RESEARCH ARTICLE SUMMARY

IMAGING TECHNIQUES

Cortical column and whole-brain imaging with molecular contrast and nanoscale resolution

Ruixuan Gao*, Shoh M. Asano*, Srigokul Upadhyayula*, Igor Pisarev, Daniel E. Milkie, Tsung-Li Liu, Ved Singh, Austin Graves, Grace H. Huynh, Yongxin Zhao, John Bogovic, Jennifer Colonell, Carolyn M. Ott, Christopher Zugates, Susan Tappan, Alfredo Rodriguez, Kishore R. Mosaliganti, Shu-Hsien Sheu, H. Amalia Pasolli, Song Pang, C. Shan Xu, Sean G. Megason, Harald Hess, Jennifer Lippincott-Schwartz, Adam Hantman, Gerald M. Rubin, Tom Kirchhausen, Stephan Saalfeld, Yoshinori Aso, Edward S. Boyden†, Eric Betzig†

INTRODUCTION: Neural circuits across the brain are composed of structures spanning seven orders of magnitude in size that are assembled from thousands of distinct protein types. Electron microscopy has imaged densely labeled brain tissue at nanometer-level resolution over near-millimeter-level dimensions but lacks the contrast to distinguish specific proteins and the speed to readily image multiple specimens. Conversely, confocal fluorescence microscopy offers molecular contrast but has insufficient resolution for dense neural tracing or the precise localization of specific molecular players within submicrometer-sized structures. Last, superresolution fluorescence microscopy bleaches fluorophores too quickly for large-volume imaging and also lacks the speed for effective brain-wide or cortex-wide imaging of multiple specimens.

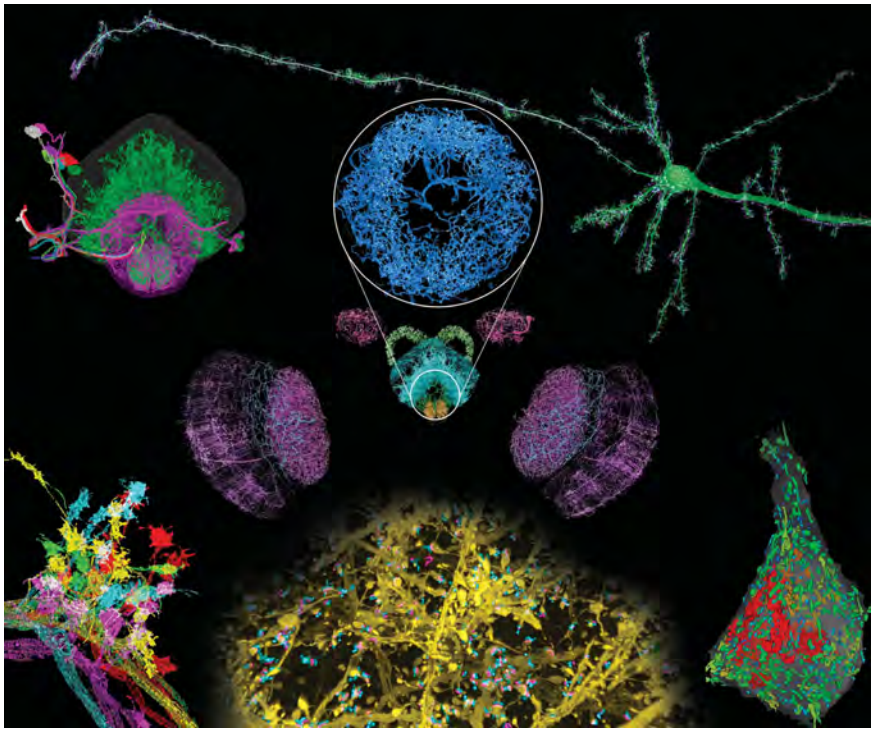

Nanoscale brain-wide optical imaging. ExLLSM images neural structures with molecular contrast over millimeter-scale volumes, including (clockwise from top right) mouse pyramidal neurons and their processes; organelle morphologies in somata; dendritic spines and synaptic proteins across the cortex; stereotypy of projection neuron boutons in *Drosophila*; projection neurons traced to the central complex; and (center) dopaminergic neurons across the brain, including the ellipsoid body (circular inset).

RATIONALE: We combined two imaging technologies to address these issues. Expansion microscopy (ExM) creates an expanded, optically clear phantom of a fluorescent specimen that retains its original relative distribution of fluorescent tags. Lattice light-sheet microscopy (LLSM) then images this phantom in three dimensions with minimal photobleaching at speeds sufficient to image the entire *Drosophila* brain or across the width of the mouse cortex in ~2 to 3 days, with multiple markers at an effective resolution of ~60 by 60 by 90 nm for 4× expansion.

ON OUR WEBSITE

Read the full article at http://dx.doi.org/10.1126/science.aau8302

RESULTS: We applied expansion/LLSM (ExLLSM) to study a variety of subcellular structures in the brain. In the mouse cortex, we quantified the volume of organelles, measured morphological parameters of ~1500 dendritic spines, determined the variation of distances between pre- and postsynaptic proteins, observed large differences in postsynaptic expression at adjacent pyramidal neurons, and studied both the azimuthal asymmetry and layer-specific longitudinal variation of axonal myelination. In *Drosophila*, we traced the axonal branches of olfactory projection neurons across one hemisphere and studied the stereotypy of their boutons at the calyx and lateral horn across five animals. We also imaged all dopaminergic neurons (DANs) across the brain of another specimen, visualized DAN morphologies in all major brain regions, and traced a cluster of eight DANs to their termini to determine their respective cell types. In the same specimen, we also determined the number of presynaptic active zones (AZs) across the brain and the local density of all AZs and DAN-associated AZs in each brain region.

CONCLUSION: With its high speed, nanometric resolution, and ability to leverage genetically targeted, cell type–specific, and protein-specific fluorescence labeling, ExLLSM fills a valuable niche between the high throughput of conventional optical pipelines of neural anatomy and the ultrahigh resolution of corresponding EM pipelines. Assuming the development of fully validated, brain-wide isotropic expansion at 10× or beyond and sufficiently dense labeling, ExLLSM may enable brainwide comparisons of even densely innervated neural circuits across multiple specimens with protein-specific contrast at 25-nm resolution or better. ■

The list of author affiliations can be found in the full article online.
*These authors contributed equally to this work.
†Corresponding author. Email: esb@media.mit.edu (E.S.B.); betzige@janelia.hhmi.org (E.B.)
Cite this article as R. Gao *et al.*, *Science* **363**, eaau8302 (2019). DOI: 10.1126/science.aau8302

Downloaded from http://science.sciencemag.org/ on January 17, 2019

RESEARCH ARTICLE

IMAGING TECHNIQUES

Cortical column and whole-brain imaging with molecular contrast and nanoscale resolution

Ruixuan Gao[1,2,3]*, Shoh M. Asano[1,2]*†, Srigokul Upadhyayula[3,4,5,6]*, Igor Pisarev[3], Daniel E. Milkie[3], Tsung-Li Liu[3]‡, Ved Singh[3]§, Austin Graves[3]¶, Grace H. Huynh[1]#, Yongxin Zhao[1], John Bogovic[3], Jennifer Colonell[3], Carolyn M. Ott[3], Christopher Zugates[7], Susan Tappan[8], Alfredo Rodriguez[8], Kishore R. Mosaliganti[9], Shu-Hsien Sheu[3], H. Amalia Pasolli[3], Song Pang[3], C. Shan Xu[3], Sean G. Megason[9], Harald Hess[3], Jennifer Lippincott-Schwartz[3], Adam Hantman[3], Gerald M. Rubin[3], Tom Kirchhausen[3,4,5,6], Stephan Saalfeld[3], Yoshinori Aso[3], Edward S. Boyden[1,2,10,11,12,13]††, Eric Betzig[3,14,15,16,17,18]††**

Optical and electron microscopy have made tremendous inroads toward understanding the complexity of the brain. However, optical microscopy offers insufficient resolution to reveal subcellular details, and electron microscopy lacks the throughput and molecular contrast to visualize specific molecular constituents over millimeter-scale or larger dimensions. We combined expansion microscopy and lattice light-sheet microscopy to image the nanoscale spatial relationships between proteins across the thickness of the mouse cortex or the entire *Drosophila* brain. These included synaptic proteins at dendritic spines, myelination along axons, and presynaptic densities at dopaminergic neurons in every fly brain region. The technology should enable statistically rich, large-scale studies of neural development, sexual dimorphism, degree of stereotypy, and structural correlations to behavior or neural activity, all with molecular contrast.

The human brain is a 1.5-kg organ that, despite its small size, contains more than 80 billion neurons (*1*) that connect through approximately 7000 synapses each in a network of immense complexity. Neural structures span a size continuum greater than seven orders of magnitude in extent and are composed of more than 10,000 distinct protein types (*2*) that collectively are essential to build and maintain neural networks. Electron microscopy (EM) can image down to the level of individual ion channels and synaptic vesicles (*3*) across the ~0.03 mm^3 volume of the brain of the fruitfly *Drosophila melanogaster* (*4*, *5*). However, EM creates a grayscale image in which the segmentation of specific subcellular components or the tracing of the complete arborization of specific neurons remains challenging and in which specific proteins can rarely be unambiguously identified. Optical microscopy combined with immunofluorescence, fluorescent proteins, or fluorescence in situ hybridization (FISH) enables high-sensitivity imaging of specific protein expression patterns in brain tissue (*6*, *7*), brain-wide tracing of sparse neural subsets in flies (*8*, *9*) and mice (*10*), and in situ identification of specific cell types (*11*, *12*) but has insufficient resolution for dense neural tracing or the precise localization of specific molecular players within critical subcellular structures such as dendritic spines. Diffraction-unlimited superresolution (SR) fluorescence microscopy (*13*, *14*) combines nanoscale resolution with protein-specific contrast but bleaches fluorophores too quickly for large-volume imaging and, like EM, would require months to years to image even a single *D. melanogaster* brain (table S1).

Given the vast array of molecular species that contribute to neural communication through many mechanisms in addition to the synaptic connections determined by EM connectomics (*15*), and given that the anatomical circuits for specific tasks can vary substantially between individuals of the same species (*16*, *17*), high-resolution three-dimensional (3D) imaging with molecular specificity of many thousands of brains may be necessary to yield a comprehensive understanding of the genesis of complex behaviors in any organism. Here, we describe a combination of expansion microscopy (ExM) (*18*, *19*), lattice light-sheet microscopy (LLSM) (*20*), and terabyte-scale image processing and analysis tools (*21*) that achieves single-molecule sensitivity and ~60- by 60- by 90-nm resolution at volumetric acquisition rates ~700× and 1200× faster than existing high-speed SR (*22*) and EM (*5*) methods, respectively, at comparable or higher resolution (table S1). We demonstrate its utility through multicolor imaging of neural subsets and associated proteins across the thickness of the mouse cortex and the entirety of the *Drosophila* brain while quantifying nanoscale parameters, including dendritic spine morphology, myelination patterns, stereotypic variations in boutons of fly projection neurons, and the number of synapses in each fly brain region.

Combining expansion and lattice light-sheet microscopy (ExLLSM)

In protein-retention ExM (proExM) (*19*), fluorophore-conjugated antibodies (Abs) and/or fluorescent proteins (FPs) that mark the features of interest within a fixed tissue are chemically linked to an infused polyacrylamide/polyacrylate gel. After protease digestion of the tissue, the gel can be expanded in water isotropically, creating an enlarged phantom of the tissue that faithfully retains the tissue's original relative distribution of fluorescent tags (fig. S1 and supplementary note 1). This yields an effective resolution given by the original resolution of the imaging microscope divided by the expansion factor. Another advantage of digestion is that lipids, protein fragments, and other optically inhomogeneous organic components that are not anchored to the gel are sufficiently removed so that the expanded gel has a refractive index nearly indistinguishable from water and therefore can be imaged aberration-free to a postexpansion depth of at least 500 μm (fig. S2) by using conventional water immersion objectives. ProExM has been applied to a range of model animals, including mouse (*19*), zebrafish (*23*), and *Drosophila* (*24*–*28*). Although up to 20× expansion has been reported (*29*), at 8× expansion by using an iterated form of

[1]MIT Media Lab, Massachusetts Institute of Technology (MIT), Cambridge, MA 02139, USA. [2]McGovern Institute for Brain Research, MIT, Cambridge, MA 02139, USA. [3]Janelia Research Campus, Howard Hughes Medical Institute, Ashburn, VA 20147, USA. [4]Department of Cell Biology, Harvard Medical School, 200 Longwood Avenue, Boston, MA 02115, USA. [5]Program in Cellular and Molecular Medicine, Boston Children's Hospital, 200 Longwood Avenue, Boston, MA 02115, USA. [6]Department of Pediatrics, Harvard Medical School, 200 Longwood Avenue, Boston, MA 02115, USA. [7]arivis AG, 1875 Connecticut Avenue NW, 10th floor, Washington, DC 20009, USA. [8]MBF Bioscience, 185 Allen Brook Lane, Suite 101, Williston, VT 05495, USA. [9]Department of Systems Biology, Harvard Medical School, 200 Longwood Avenue, Boston, MA 02115, USA. [10]Department of Biological Engineering, MIT, Cambridge, MA 02139, USA. [11]MIT Center for Neurobiological Engineering, MIT, Cambridge, MA 02139, USA. [12]Department of Brain and Cognitive Sciences, MIT, Cambridge, MA 02139, USA. [13]Koch Institute, MIT, Cambridge, MA 02139, USA. [14]Department of Molecular and Cell Biology, University of California, Berkeley, CA 94720, USA. [15]Department of Physics, University of California, Berkeley, CA 94720, USA. [16]Howard Hughes Medical Institute, Berkeley, CA 94720, USA. [17]Helen Wills Neuroscience Institute, Berkeley, CA 94720, USA. [18]Molecular Biophysics and Integrated Bioimaging Division, Lawrence Berkeley National Laboratory, Berkeley, CA 94720, USA.

*These authors contributed equally to this work. †Present address: Internal Medicine Research Unit, Pfizer, Cambridge, MA 02139, USA. ‡Present address: Vertex Pharmaceuticals, 3215 Merryfield Row, San Diego, CA 92121, USA. §Present address: Intel, 2501 Northwest 229th Avenue, Hillsboro, OR 97124, USA. ¶Present address: Department of Neuroscience, Johns Hopkins University School of Medicine, Baltimore, MD 21205, USA. #Present address: Microsoft Research Lab, 14820 NE 36th Street, Redmond, WA 98052, USA. **Present address: Department of Biological Sciences, Carnegie Mellon University, Pittsburgh, PA 15143, USA.
††Corresponding author. Email: esb@media.mit.edu (E.S.B.); betzige@janelia.hhmi.org (E.B.)

Downloaded from http://science.sciencemag.org/ on January 17, 2019

the N,N-dimethylacrylamide-gel expansion protocol, we observed regions where the expansion superficially appears accurate (fig. S3A) and other regions of clear distortion, such as irregularly shaped somata and nuclei (fig. S3B). High expansion ratios also require exceptionally high fluorescence labeling densities to take advantage of the theoretically achievable resolution and take longer to image. Thus, for this work we chose to focus only on applications (table S2) enabled by 4× expansion.

Several challenges emerge when attempting to extend ExM to specimens at the millimeter scale of the fly brain or a mouse cortical column. First, even 4× expansion requires effective voxel dimensions of ~30 to 50 nm on each side to match the full resolution potential of ExM, or ~20 trillion voxels/mm^3/color. This in turn necessitates imaging at speeds on the order of 100 million voxels/s to complete the acquisition in days rather than weeks or more, as well as an image-processing and -storage pipeline that can handle such high sustained data rates. Second, photobleaching often extinguishes the fluorescence signal from deeper regions of 3D specimens before they can be imaged—a problem that becomes more severe with thicker specimens, longer imaging durations, and/or the higher illumination intensities needed for faster imaging. Last, because ExM resolution is proportional to imaging resolution, the latter should be as high as possible within these other constraints while also striving for near-isotropic resolution, so that neural tracing and quantification of nanoscale structures is not limited by the axis of poorest resolution.

To address these challenges, we turned to LLSM (*20*), which sweeps an ultrathin sheet of laser light through a specimen and collects the resulting fluorescence from above with a high numerical aperture (NA) objective to image it on a high-speed camera (supplementary note 2). Confinement and propagation of excitation light within the detection focal plane permits parallel acquisition of data at rates of 10 million to 100 million voxels/s at low intensities that minimize photobleaching within the plane and eliminates bleaching in the unilluminated regions above and below. Consequently, we could image large volumes of expanded tissue expressing yellow fluorescent protein (YFP) in a subset of mouse cortical neurons with uniform signal from top to bottom (Fig. 1A, left). By contrast, at a comparable signal in the acquired images, the out-of-focus excitation and high peak power at the multiple foci of a spinning disk confocal microscope (SDCM) photobleached the expanded tissue ~10× faster than LLSM (Fig. 1C), rendering deeper regions completely dark (Fig. 1, A and B, center), while the sparse illumination of the SDCM focal array slowed volumetric acquisition by ~7× (table S1). Another commercial alternative, Airyscan, efficiently images the fluorescence generated at the excitation focus and uses this information to extend the imaging resolution approximately 1.4× beyond the diffraction limit (*30*, *31*). However, Airyscan imaged expanded tissue ~40× slower (table S1) and with ~20× faster bleaching (Fig. 1C) than LLSM.

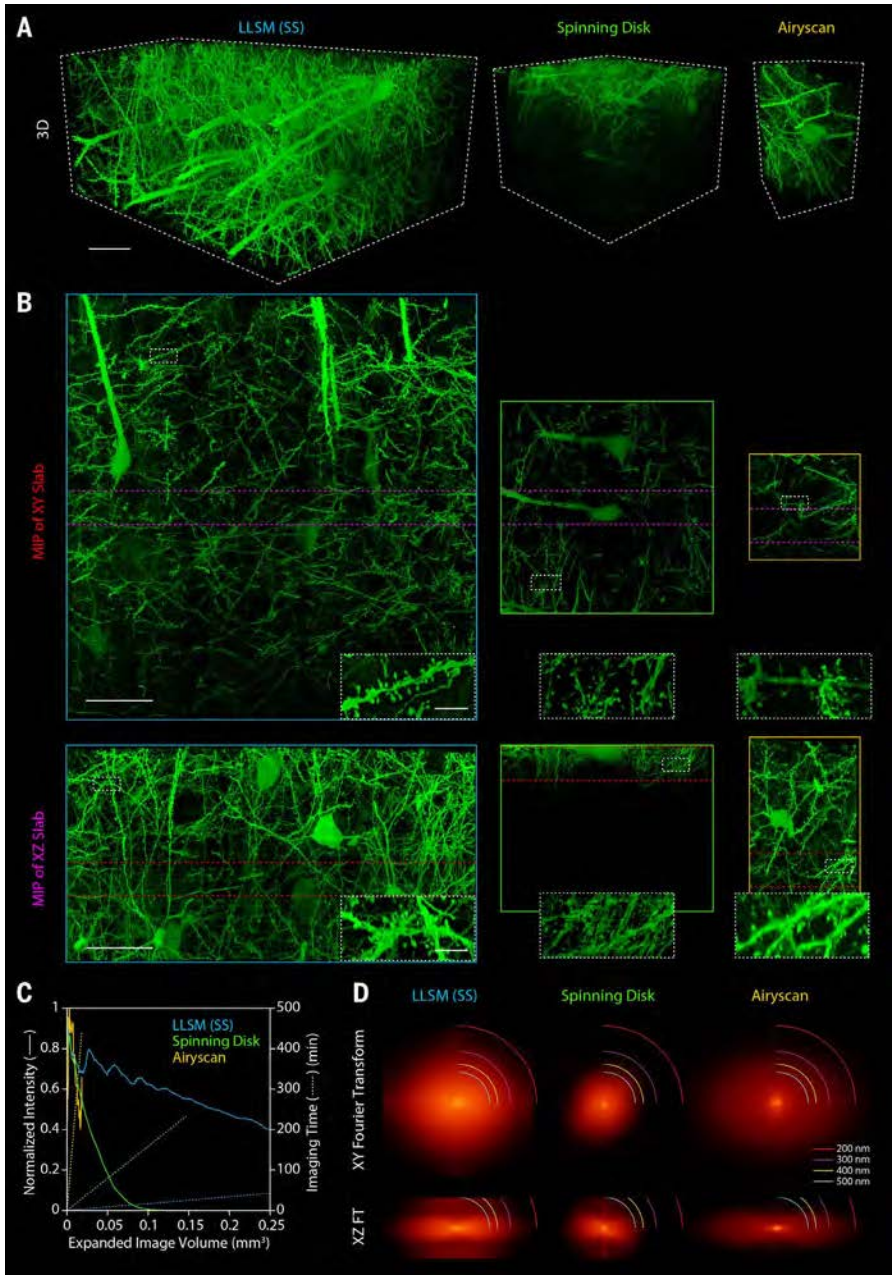

Fig. 1. Comparing modalities to image-expanded mouse brain tissue. (**A**) 3D rendered volumes at equal magnification of tissue sections from the primary somatosensory cortex of a Thy1-YFP transgenic mouse, expanded ~4× by using the protein-retention expansion microscopy (proExM) protocol and imaged by means of (left to right) LLSM in sample scan mode [LLSM (SS), blue]; spinning disk confocal microscopy (Spinning Disk, green); and Airyscan in fast mode (Airyscan, orange). Scale bars, 50 μm, here and elsewhere given in preexpanded (biological) dimensions. (**B**) (Top) *xy* and (bottom) *xz* maximum intensity projections (MIPs) of 25-μm-thick slabs cut from the image volumes in (A) at the locations denoted by the red and purple lines in the slabs perpendicular to them, respectively. (Insets) Regions in the white rectangles at higher magnification. Scale bars, 50 μm, full MIPs; 5 μm, insets. (**C**) Comparative imaging and photobleaching rates for the three modalities (table S1). (**D**) (Top) *xy* and (bottom) *xz* spatial frequency content in the same three image volumes as measured from mitochondria-targeted antibody puncta, with different resolution bands as shown (fig. S4).

LLSM can operate in two modes: objective scan (fig. S4), in which the sample is stationary while the light-sheet and detection objective move in discrete steps across the image volume, and sample scan (Fig. 1), in which the sample is swept continuously through the light sheet. Sample scan is faster (tables S1) but yields slightly lower *yz* resolution (fig. S4) than that of

Downloaded from http://science.sciencemag.org/ on January 17, 2019

objective scan because information in the sample scanning direction is slightly blurred by simultaneous image acquisition and sample movement. Of the methods above, Airyscan should in principle achieve the highest lateral (*xy*) resolution, followed by SDCM (owing to pinhole filtering), and last, the two modes of LLSM. In practice, however, dendritic spines and axons appeared more clearly and faithfully resolved in lateral views with LLSM than with SDCM or even Airyscan (Fig. 1B, top row), a conclusion corroborated by its higher lateral spatial frequency content (Fig. 1D and fig. S4A, top rows) as measured from mitochondria-targeted Ab puncta. Likewise, the thinness of the lattice light sheet contributes to the axial (*z*) resolution of LLSM (Fig. 1D and fig. S4A, bottom rows) and therefore yielded *xz* views of spines and axons only slightly poorer than in the lateral plane and substantially sharper than those obtained with SDCM or Airyscan (Fig. 1B, bottom row).

One additional challenge in millimeter-scale ExLLSM involves the processing of multiterabyte data sets. In LLSM, the lateral extent of the light sheet (table S2) is far smaller than an expanded fly brain or cortical column, so the final image volumes had to be computationally stitched together from as many as 25,000 (table S2) tiled subvolumes per color. However, because of systematic sample stage errors and slight swelling or shrinking of expanded samples over many hours, many tiles did not perfectly overlap with their neighbors on all six sides. To address this, we developed an Apache Spark–based high-performance computing pipeline (supplementary note 3 and figs. S5 to S7) that first performed a flat-field correction for each tile to account for intensity variations across the light sheet and then stitched the intensity-corrected tiles together by using an automated and iteratively refined prediction model of tile coordinates. In a separate track, each intensity-corrected tile was deconvolved by using a measured point spread function (PSF) so that when the final set of coordinates for all tiles was available, the deconvolved image volume of the entire specimen could be assembled and visualized (supplementary note 4 and 5) with minimal stitching artifacts.

Quantification of subcellular structures in mouse cortical neurons

The protein-specific fluorescence contrast of ExLLSM enabled rapid, computationally efficient, and purely automated segmentation and nanoscale quantification of subcellular neural structures over large volumes. For example, dense cytosolic expression of YFP under the *thy1* promotor in mouse pyramidal neurons revealed sharply delineated voids (Movie 1) representing subcellular compartments (Fig. 2A) of various shapes and sizes whose volumes we could quantify accurately (Fig. 2B and supplementary note 4d). Simultaneous immunofluorescence labeling against Tom20 and LAMP1, although comparatively sparse (movie S1), was sufficient to identify the subset of these that represented mitochondria or lysosomes (Fig. 2C)—in the latter case, the specific subset with LAMP1 that likely represented multivesicular bodies or autolysosomes (supplementary note 6a) (*32*). As expected, we found that mitochondria were generally both longer and larger in volume than lysosomes (Fig. 2D and table S3). Mitochondria ranged in length from 0.2 to 8.0 μm, which is consistent with EM measurements in the cortex (*33*) or other regions (*34*) of the mouse brain, whereas the subset of LAMP1 compartments ranged from 0.1 to ~1.0 μm, which is also consistent with EM (*35*).

Given this agreement—and the important roles mitochondria play in dendrite development, synapse formation, calcium regulation, and neurodegenerative disease (*34*, *36*, *37*)—we extended our analysis across ~100 by 150 by 150 μm of the mouse somatosensory cortex. We classified length, aspect ratio, and volume (Fig. 2E and fig. S8) of 2893 mitochondria and 222 lysosomes across the somata and initial portions (78 μm mean length) of the apical dendrite of five-layer V pyramidal neurons, as well as the initial portions (95 μm mean length) of three descending axon segments. As noted previously in the hippocampus (*36*), we found that long and high-aspect-ratio mitochondria were far more prevalent in apical dendrites than in axons, with mitochondria longer than 3 μm comprising 6.5% all dendritic mitochondria (~12 per 100 μm of dendrite length) versus 0.7% of all axonal ones. These differences may represent the difficulty in assembling and maintaining large organelles within the narrow confines of the axon, or they may reflect functional differences in the regulation of calcium in axons versus dendrites.

We next turned our attention to the myelination of axons, which is essential for the rapid (*38*, *39*) and energy-efficient (*40*) propagation of action potentials (APs) and which, when disrupted, can lead to neurodegenerative diseases such as multiple sclerosis (*41*). The propagation velocity is affected by the g-ratio, the diameter of the axon normalized to the diameter of its surrounding myelin sheath (*42*). Most EM measurements of the g-ratio come from 2D images of single sections cut transversely to axonal tracts (*43*–*45*) and therefore lack information on how the g-ratio might vary along the length of a given axon. To address this, we used ExLLSM to image a 320- by 280- by 60-μm volume in the primary somatosensory cortex of a Thy1-YFP transgenic mouse immunostained against myelin basic protein (MBP) (Fig. 2F and Movie 2). At every longitudinal position z along a given myelinated axon, we measured the local g-ratio at every azimuthal position θ by dividing the radius $\rho_{axon}(\theta, z)$ of the axon along the radial vector from the axon center by the radius $\rho_{myelin}(\theta, z)$ of the outer edge of the myelin sheath along the same vector (Fig. 2G, fig. S9, and supplementary note 4e). Across one 56-μm-long segment, the mean g-ratio of 0.57 calculated from mean axon and sheath diameters of 0.52 and 0.90 μm, respectively, fell at the lower end of a distribution previously reported in the central nervous system yet was consistent with a theoretical estimate of 0.60 for the ratio that optimizes propagation velocity (*42*). However, these values do not reflect the substantial variability we observed, with the outer axon–to–outer myelin distance ranging from 0.12 to 0.35 μm (fig. S10) and the local g-ratio ranging from ~0.4 to 0.8 (Fig. 2H and Movie 2). Furthermore, the axon and the sheath were rarely concentric (Fig. 2G), leading to rapid longitudinal changes in capacitance and impedance that may

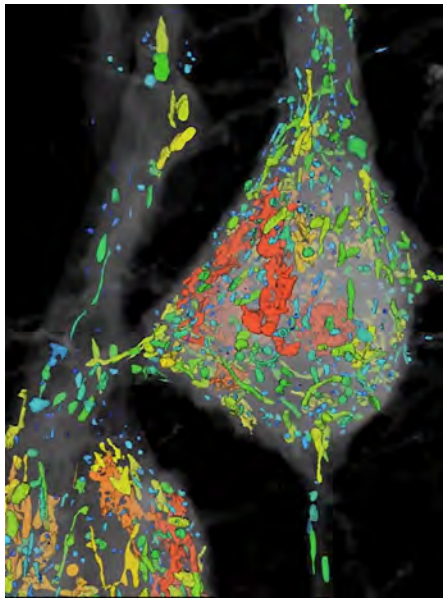

Movie 1. Organelle analysis of layer V pyramidal neurons in the mouse somatosensory cortex. Segmentation of cytosolic voids in Thy1-YFP–expressing neurons, quantification of their volumes, and immunostaining-based classification of those voids that represent mitochondria or multivesicular bodies or autolysosomes (Fig. 2, A to E; fig. S8; and movie S1).

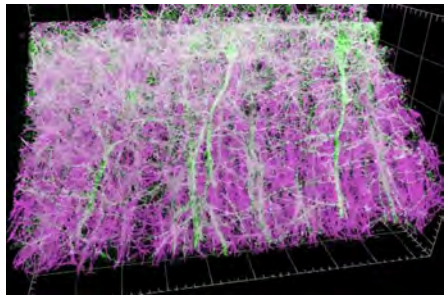

Movie 2. Axon myelination and local g-ratio of layer V pyramidal neurons of the mouse primary somatosensory cortex. Thy1-YFP–expressing neurons and immunostained myelin sheaths across 320 by 280 by 60 μm, with quantification of the local g-ratio on the surface of a specific myelin sheath (Fig. 2, F and G, and figs. S9 and S10).

Downloaded from http://science.sciencemag.org/ on January 17, 2019

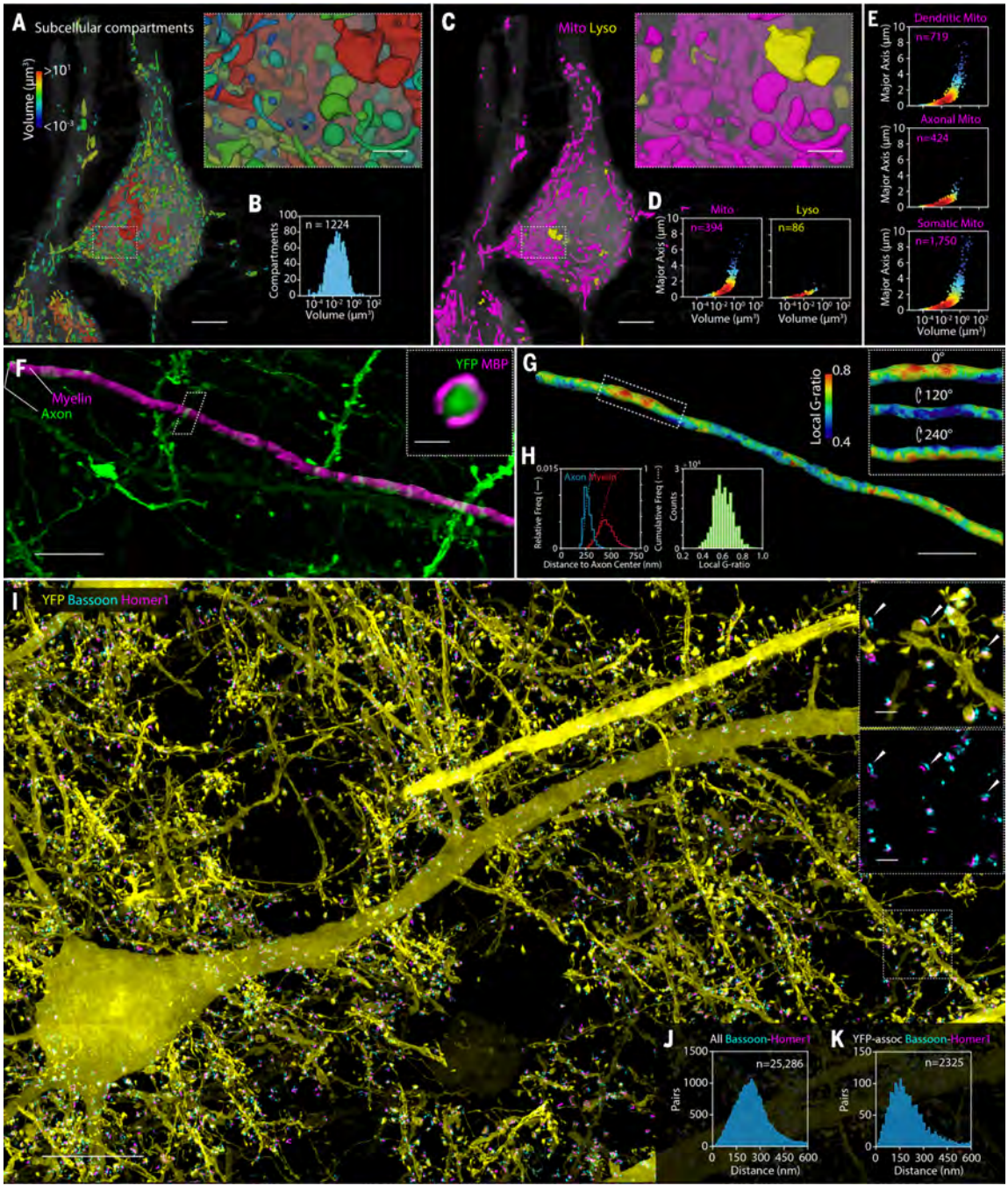

Fig. 2. Nanoscale, protein-specific 3D imaging of subcellular neural structures. (**A**) Segmented compartments void of cytosolic YFP (gray), color-coded by volume, in portions of the somata and apical dendrites of two layer V pyramidal neurons from the somatosensory cortex of a Thy1-YFP mouse (Movie 1). Scale bars, 5 μm and (inset) 1 μm. (**B**) Distribution of the compartment volumes. (**C**) Same region as (A), with voids identified with immunostaining (movie S1) as either mitochondria (magenta) or multivesicular bodies or autolysosomes (yellow). (**D**) Scatter plots of the major axis (long axis) length versus volume for the two organelle types. Point colors in (D) and (E) indicate relative data point density (blue, low; red, high). (**E**) Similar scatter plots for mitochondria only, separated by cellular region (fig. S8). (**F**) Axon of a layer V pyramidal neuron and its surrounding myelin sheath, from the primary somatosensory cortex of another Thy1-YFP mouse, immunostained against myelin (Movie 2). (Inset) A cross-sectional view through the white parallelogram. Scale bars, 5 μm and (inset) 500 nm. (**G**) Same region as (F), with the myelin sheath color coded according to the local g-ratio (fig. S10). (Inset) Azimuthal variation in g-ratio in the region within the rectangle. Scale bar, 5 μm. (**H**) (Left) Distribution of axon radius and myelin outer radius and (right) distribution of g-ratio at all points on the axon in (G). (**I**) *xy* MIP of a 9.3-μm-thick slab within a 75- by 100- by 125-μm volume from the primary somatosensory cortex of a Thy1-YFP mouse, immunostained against synaptic proteins Bassoon and Homer1 (Movie 3 and fig. S10). Only YFP-associated Bassoon/Homer1 pairs are shown for clarity. (Insets) (Top) magnified *xy* MIP of a 2.2-μm-thick slab from boxed region at right. (Bottom) All Bassoon/Homer1 pairs in the same region. Three pairs are indicated with arrows. Scale bars, 10 μm and (insets) 1 μm. (**J**) Distribution of distances between paired Bassoon and Homer1 centroids across the entire volume. (**K**) Distribution when restricted to only those pairs associated with YFP-expressing neurons.

Downloaded from http://science.sciencemag.org/ on January 17, 2019

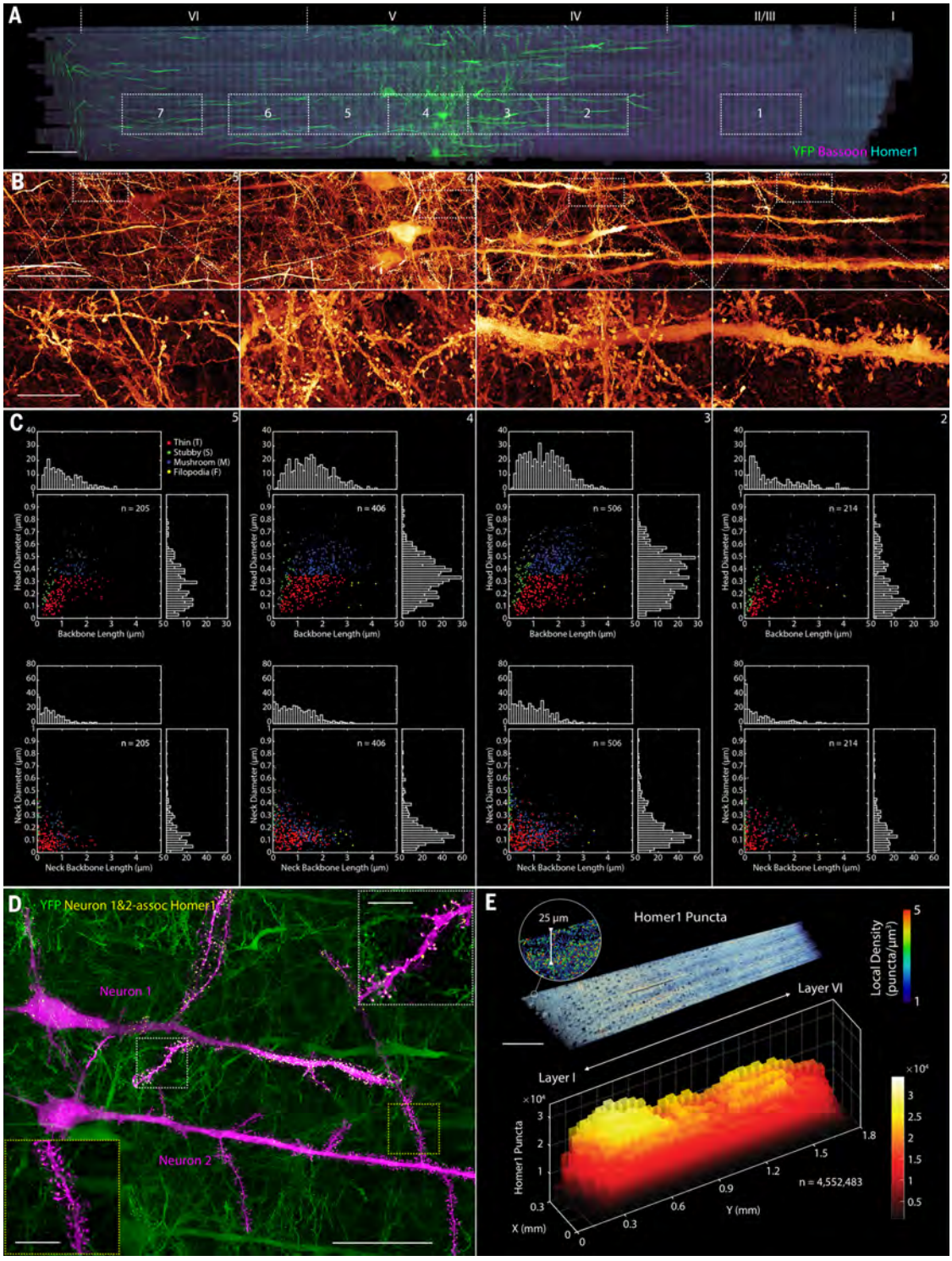

Fig. 3. Characterizing dendritic spine morphologies and postsynaptic Homer1 across the mouse primary somatosensory cortex. (**A**) Coronal MIP of a 1900- by 280- by 70-µm tissue section spanning the pia to the white matter of the primary somatosensory cortex of a Thy1-YFP mouse (Movie 4), additionally immunostained against Bassoon and Homer1. Boxes denote seven regions for quantitative morphological analysis of dendritic spines. Scale bar, 100 µm. (**B**) (Top) Magnified MIPs of YFP-expressing neurons in four of the regions from (A), with (bottom) further magnified subregions showing differing spine morphologies. Scale bars, (top) 50 µm and (bottom) 10 µm. (**C**) Scatter plots and histograms indicating relationships between (top) spine backbone length and head diameter and (bottom) spine neck length and neck diameter in the four regions from (B) (figs. S13 to S15 and movie S2). (**D**) Two adjacent layer V pyramidal neurons selected within the volume (magenta), one exhibiting strong Homer 1 expression (neuron 1) and the other exhibiting weak expression (neuron 2). (Insets) Homer1 localization or lack thereof at apical dendritic spines (fig. S17). Scale bars, 50 µm and (insets) 10 µm. (**E**) (Top) MIP of the local density of Homer1 puncta across a ~25-µm-thick coronal slab, and (bottom) the cumulative number of puncta in 50- by 50- by 25-µm subvolumes across the cortex.

Downloaded from http://science.sciencemag.org/ on January 17, 2019

influence the speed and efficiency of signal propagation. We subsequently confirmed these observations with EM (fig. S11 and supplementary note 2h).

ExLLSM is also well suited to study the nanoscale organization of synaptic proteins over large tissue volumes. Imaging a 75- by 100- by 125-μm tissue section cut from layer IV/V of the primary somatosensory cortex of a transgenic Thy1-YFP mouse, we identified 25,286 synapses that have closely juxtaposed concentrations of immunolabeled pre- and postsynaptic proteins Bassoon and Homer1 (fig. S12A), 2325 of which had Homer1 localized at YFP-labeled dendritic spines (Fig. 2I and Movie 3). These tended to form nested caps, with major axis lengths of 856 ± 181 nm and 531 ± 97 nm for Bassoon and Homer1, respectively [median ± median absolute deviation (MAD)] (fig. S12, B and C). The Homer1 distribution was consistent with SR measurements in dissociated hippocampal neurons (DHN) (*46*), but our Bassoon values were slightly larger. The centroid-to-centroid distance we measured between Bassoon/Homer1 pairs was 243 ± 69 nm for all pairs within the volume (Fig. 2J) and 185 ± 70 nm for those associated with YFP-filled spines (Fig. 2K). The difference between these values suggests that mature glutamatergic synapses of layer V pyramidal neurons, which are the ones expressing YFP, are narrower than other types across the primary somatosensory cortex. The difference between these values and previous SR measurements of 150 ± 20 nm in the ventral orbital cortex (n = 252 Bassoon/Homer1 pairs) (*47*), 165 ± 9 nm in DHN (n = 43 pairs) (*46*), and 179 ± 42 nm in the middle of the primary somatosensory cortex (n = 159 pairs) (*29*) may reflect natural variations in different brain regions (*29*) or a systematic bias in these earlier studies arising by measuring the distance between 1D Gaussian fits to the Bassoon/Homer1 distributions in a manually selected slice through the heart of each synapse, versus our approach of calculating the distance between the 3D centroids calculated across the complete distributions.

Somatosensory cortex–spanning measurement of dendritic spines and excitatory synapses

The combination of fast imaging (table S1) and targeted sparse labeling enables ExLLSM-based quantification of nanoscale neural structures to be extended to millimeter-scale dimensions over multiterabyte data sets. This yields statistically large sample populations that can reveal subtle changes in the distributions of specific morphological parameters across different regions of the brain.

One such application involves the morphology of dendritic spines in different layers of the mouse cerebral cortex. A spine is a small (~0.01 to 1.0 μm^3) membranous protrusion from a neuronal dendrite that receives synaptic input from the closely juxtaposed axon of another neuron. Spine morphology has been extensively studied with a variety of imaging methods (*48*), in part because it is related to synaptic strength (*49*), whose time- and activity-dependent change (plasticity) (*50*) is implicated in learning and memory consolidation (*51*). However, although optical methods such as Golgi impregnations (*52*), array tomography (*6*), and confocal (*53*) and two-photon microscopy (*54*, *55*) can image the complete arborization of neurons spanning the cortex, they lack the 3D nanometric resolution needed to measure the detailed morphology of spines. Conversely, EM (*56*, *57*) and SR fluorescence microscopy (*58*, *59*) have the requisite resolution but not the speed to scale readily to cortical dimensions. ExLLSM, however, has both.

To demonstrate this, we imaged a 1900- by 280- by 70-μm tissue slice spanning the pia to the white matter in the primary somatosensory cortex of a transgenic Thy1-YFP mouse expressing cytosolic fluorescence within a sparse subset of layer V pyramidal neurons. The slice was additionally immunostained against Bassoon and Homer1 (Fig. 3A and Movie 4). In each of seven different regions across the cortex (Fig. 3B and fig. S13A), we selected four 27- by 27- by 14-μm subvolumes and used a modified commercial analysis pipeline (supplementary note 4f) (*60*) to segment (fig. S14 and movie S2) and measure spine ultrastructure. Across the ~1500 spines so measured, the range of spine head diameters, neck diameters, overall backbone lengths (spine root to tip), and neck backbone lengths (Fig. 3C and figs. S13B and S15) were consistent with those seen in an EM study of layer II/III pyramidal neurons in the mouse visual cortex (*56*). Furthermore, the absence of spines in the initial segment of the distal apical dendrite, and prevalence of much larger spines on smaller dendritic branches than on the remainder of the distal apical dendrite (Fig. 3D), were in line with an EM study of pyramidal neurons in the primary somatosensory cortex of the cat (*61*). Mean spine head diameter and mean neck backbone length each approximately doubled from layer II/III (position 1) to the regions of layers IV and V (positions 3 and 4) nearest the somata before falling again in layer VI (positions 6 and 7) to levels similar to layer II/III (table S4). This is consistent with a longitudinal in vivo study of spine morphology that found that spines closer to the soma, including those on proximal apical dendrites, were more mature and formed stronger synaptic connections than those on basal dendrites or the distal apical dendrite (*62*). We also found that head diameter and backbone length or neck backbone length were correlated across all layers of the cortex (Fig. 3C, top row; figs. S13B, top row, and S15; and table S4), but neck diameter and neck backbone length were not correlated across all regions (Fig. 3C, bottom row; fig. S13B, bottom row; and table S4).

Colabeling with Homer1-specific antibodies allowed us also to map excitatory synapses and their density (Fig. 3E) across the primary somatosensory cortex. In particular, when 4.5 million Homer1 puncta were binned in 50- by 50- by 25-μm subvolumes to average across local fluctuations, their density was revealed to be ~1.5 to 2.0× greater in layers II/III and V (~40 to 50 puncta/μm^3) than in adjacent layers I, IV, and VI. Similar dual maxima in synaptic density are seen in sparsely sampled EM images of the rat somatosensory (*63*) and mouse barrel cortex (*64*), although in different cortical layers (rat, II and IV; mouse, I and IV) than seen in this work.

Focusing on the subset of Homer1 puncta colocalized with YFP-expressing dendritic spines, we found that thin spines were approximately twice as likely to coexpress Homer1 as spines classified as stubby, mushroom, or filopodial (fig. S16). As a synaptic scaffold protein, Homer1 plays an important role in the recruitment and cross-linking of other proteins that lead to the maturation and enlargement of spines (*65*–*67*), so Homer1's relative abundance at thin spines may presage their transformation to more mature forms. Surprisingly, we also observed dramatic variations in the expression of Homer1 within neighboring layer V pyramidal neurons: Homer1 was present at nearly all spines and throughout the cytosol of one neuron (Fig. 3D, neuron 1), whereas a parallel neuron ~57 μm away of similar morphology exhibited very little Homer1,

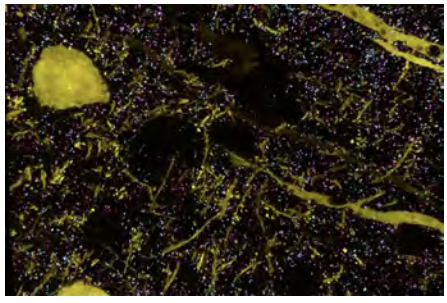

Movie 3. Synaptic proteins and their associations to neuronal processes in layers IV and V of the mouse primary somatosensory cortex. Thy1-YFP–expressing neurons and immunostained pre- and postsynaptic proteins Bassoon and Homer1 across 75 by 100 by 125 μm, sequentially showing all Bassoon and Homer1 puncta, and only YFP-associated Bassoon and Homer1 pairs (Fig. 2, I to K, and fig. S12).

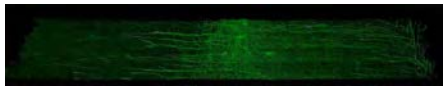

Movie 4. Relationship of postsynaptic Homer1 to neuronal processes across the mouse primary somatosensory cortex. Thy1-YFP–expressing neurons and immunostained postsynaptic protein Homer1 across 1900 by 280 by 70 μm in the primary somatosensory cortex, with specific focus on two adjacent layer V pyramidal neurons that exhibit substantially different patterns of Homer1 expression (Fig. 3, figs. S13 to S17, and movie S2).

Downloaded from http://science.sciencemag.org/ on January 17, 2019

even at its dendritic spines (Fig. 3D, neuron 2). This difference did not result from differential labeling efficiency because the density of Homer1 puncta in the immediate surrounds of each neuron was similar (fig. S17). Instead, because Homer1 levels are known to change rapidly under different neuronal states [for example, asleep versus awake (*68*)], it may reflect the different excitatory states of these two neurons at the time the animal was sacrificed.

Visual cortex–spanning neuronal tracing and myelination patterns

Although the radial anisotropy of axonal myelination (Fig. 2E) can affect the speed and efficiency of AP propagation, so too can its

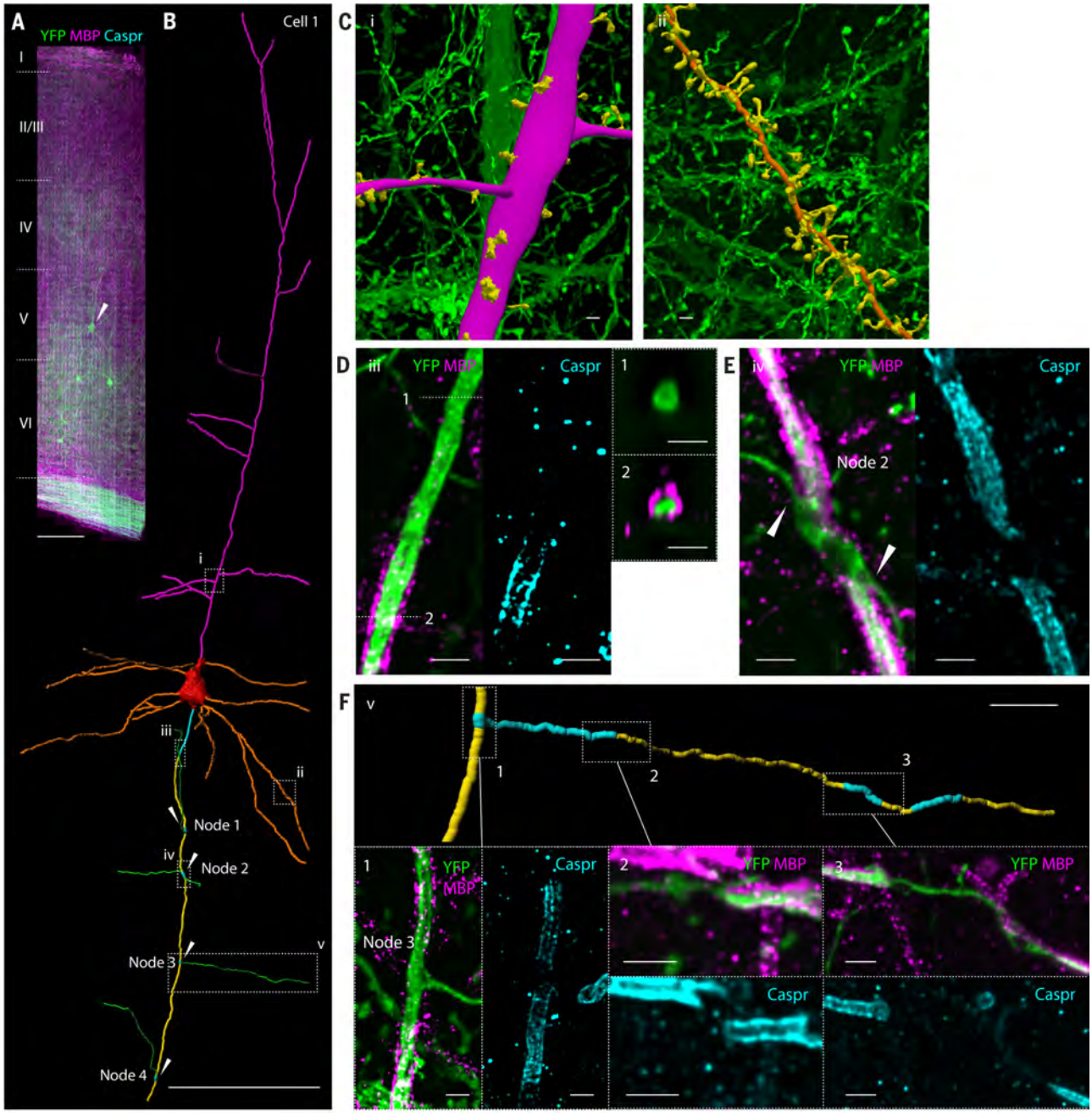

Fig. 4. Neural tracing and longitudinal myelination analysis across the mouse primary visual cortex. (**A**) Coronal MIP of a 25-μm-thick slab within a 1100- by 280- by 83-μm tissue section spanning the pia to the white matter of the primary visual cortex of a Thy1-YFP mouse (Movie 5), additionally immunostained against MBP and Caspr to highlight myelin sheaths and nodes of Ranvier, respectively. Scale bar, 100 μm. (**B**) Traced arborization (Movie 6) of a specific layer V pyramidal neuron denoted by the arrowhead in (A), showing the soma (red), apical (magenta), and basal (orange) dendrites; myelinated (yellow) and unmyelinated (cyan) axon segments; and collateral axon branches (green). Arrows indicate nodes of Ranvier. Scale bar, 100 μm. (**C**) Magnified segmented views of (left) the distal apical dendrite and two of its branches and (right) a basal dendrite and its spines, from boxed regions i and ii in (B), respectively. Scale bars, 1 μm. (**D**) MIP view of boxed region iii in (B), showing (left) the distal end of the PMAS; (middle) Caspr at the start of myelination; and (right) cross-sectional views of the axon (1) before and (2) after the start of myelination. Scale bars, 1 μm. (**E**) MIP view of boxed region iv in (B), showing (left) break in myelination and two branching collateral axons at a node of Ranvier and (right) Caspr highlighting the two ends of the node. Scale bars, 1 μm. (**F**) (Top) Segmented view of a collateral axon with myelinated and unmyelinated sections from boxed region v in (B). (Bottom) Three MIP views of breaks in myelination with flanking Caspr. Scale bars, (top) 10 μm; (bottom) 1 μm.

Downloaded from http://science.sciencemag.org/ on January 17, 2019

longitudinal variation. The repeated gaps in myelination at the nodes of Ranvier house ion channels that are essential to regenerate the AP during saltatory conduction (*69*), the hallmark of high-speed signal propagation in vertebrates. Recently, however, high-throughput EM imaging and axonal tracing at 30 by 30 by 240 nm/voxel (*70*) has revealed additional gaps in the axonal myelination of layer II/III neurons in the mouse primary visual cortex much larger (for example, 55 μm) than either the ~2 μm typical of the nodes of Ranvier or the shorter and rarer gaps observed in layers III to VI of the primary somatosensory cortex.

To determine whether these differences are more reflective of the layer of origination of the axon or the functional role of the cortical region studied (the somatosensory versus the visual cortex), we imaged at 27 by 27 by 50 nm/voxel a ~280- by 1100- by 83-μm tissue section from the primary visual cortex extending from the pia to the white matter of a Thy1-YFP mouse. The tissue was additionally immunostained against MBP and contactin-associated protein (Caspr) (*71*) to visualize myelin sheaths and their terminations, respectively (Fig. 4A and Movie 5). Although the dense global staining of EM makes long-range 3D tracing of small neurites challenging, expression of YFP in a sparse subset of layer V and layer VI pyramidal neurons (*72*) enabled rapid semiautomatic tracing (supplementary note 4h) of axons, their myelination, and the entire arborization of selected neurons across the tissue section (Fig. 4B and Movie 6). This included the distal apical dendrite and its branches (Fig. 4C, i), basal dendrites and their spines (Fig. 4C, ii), the premyelin axonal segment (PMAS) (Fig. 4D), the nodes of Ranvier (Fig. 4E), and collateral branches of the main axon originating at the nodes (Fig. 4F). All these features matched the known morphologies of layer V pyramidal neurons (*73*) and were recapitulated in a second neuron traced throughout the volume (Fig. 5A and Movie 6).

Given this assurance, we traced the axons and their longitudinal myelination patterns for 10 neurons in layer V and 11 more in layer VI (Fig. 5B). Within the imaged volume, all of the layer V axons in the primary visual cortex exhibited continuous myelination beyond the end of the PMAS, except for the expected small gaps at the nodes of Ranvier. This is consistent with the myelination pattern seen previously for layer III to VI axons in the primary somatosensory cortex (*70*). The range of PMAS lengths we measured for these neurons (28 to 41 μm, mean = 34.9 ± 1.1 μm) was also consistent with the range found in layers V and VI of the primary somatosensory cortex (25 to 40 μm, mean = 33.7 ± 2.4 μm). The internodal spacing of the

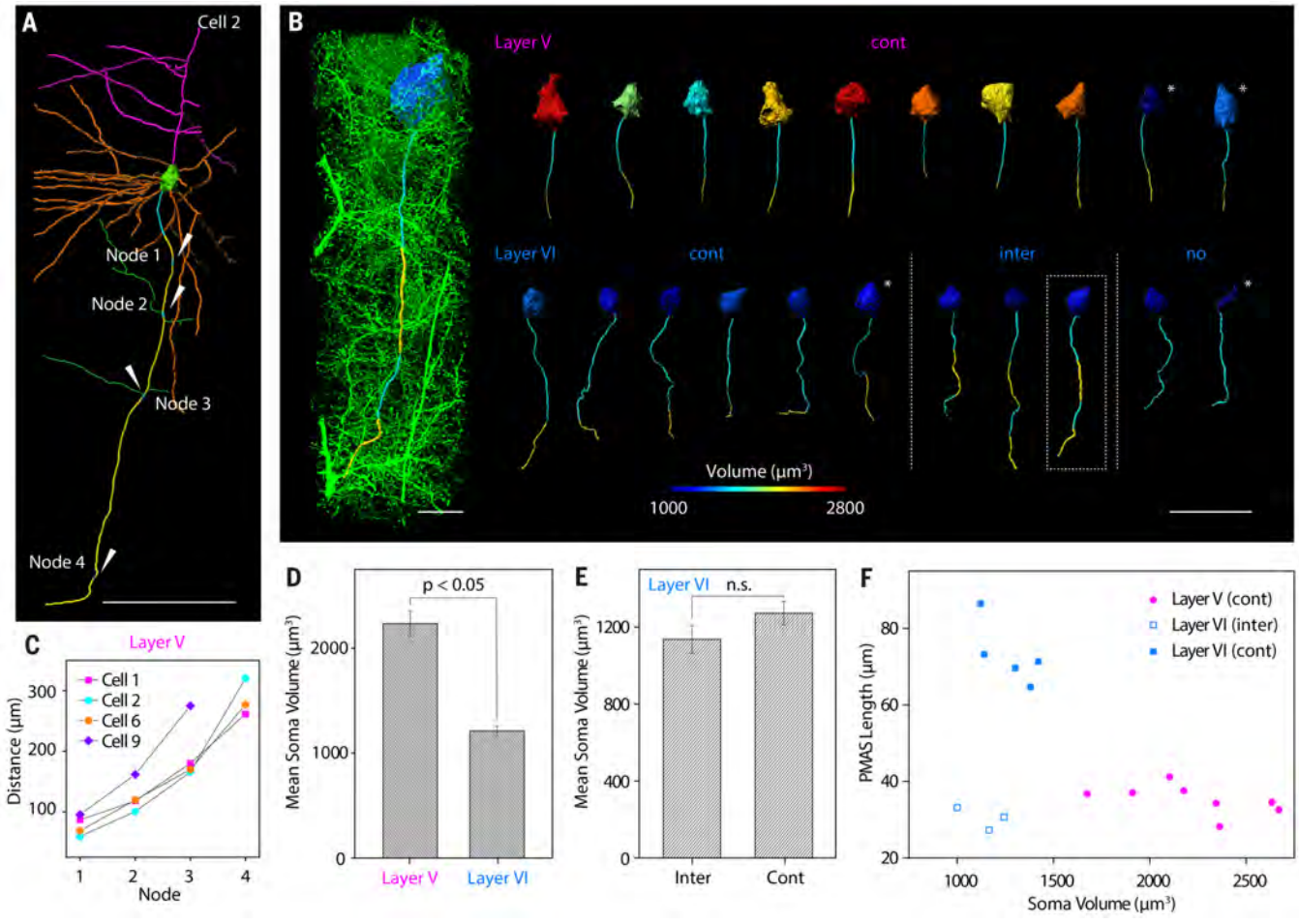

Fig. 5. Longitudinal myelination profiles of layer V and VI pyramidal neurons in the mouse primary visual cortex. (**A**) Traced arborization of a second layer V pyramidal neuron within the volume in Fig. 4A. Scale bar, 100 μm. (**B**) (Left) Segmented soma and axon of a pyramidal neuron shown in the context of its surroundings in layer VI. (Right) Segmented somata (color coded by volume) and axons, showing myelinated (yellow) and unmyelinated (cyan) segments, for 10 pyramidal neurons from layer V (top row) and 11 more from layer VI (bottom row). Boxed neuron is shown at left. Scale bars, (left) 10 μm and (right) 50 μm. (**C**) Node spacing for four layer V neurons from (B) (fig. S18). (**D**) Volumes of eight layer V and nine layer VI somata fully within the image volume [no asterisks in (B)] (mean ± SEM). (**E**) Volumes of the three somata with intermittently myelinated axons and five somata with continuously myelinated axons in layer VI (mean ± SEM). The *P* values are calculated from a permutation test for medians. n.s., not significant. (**F**) Scatter plot of soma volume versus PMAS length for the neurons in (B) (fig. S19).

Downloaded from http://science.sciencemag.org/ on January 17, 2019

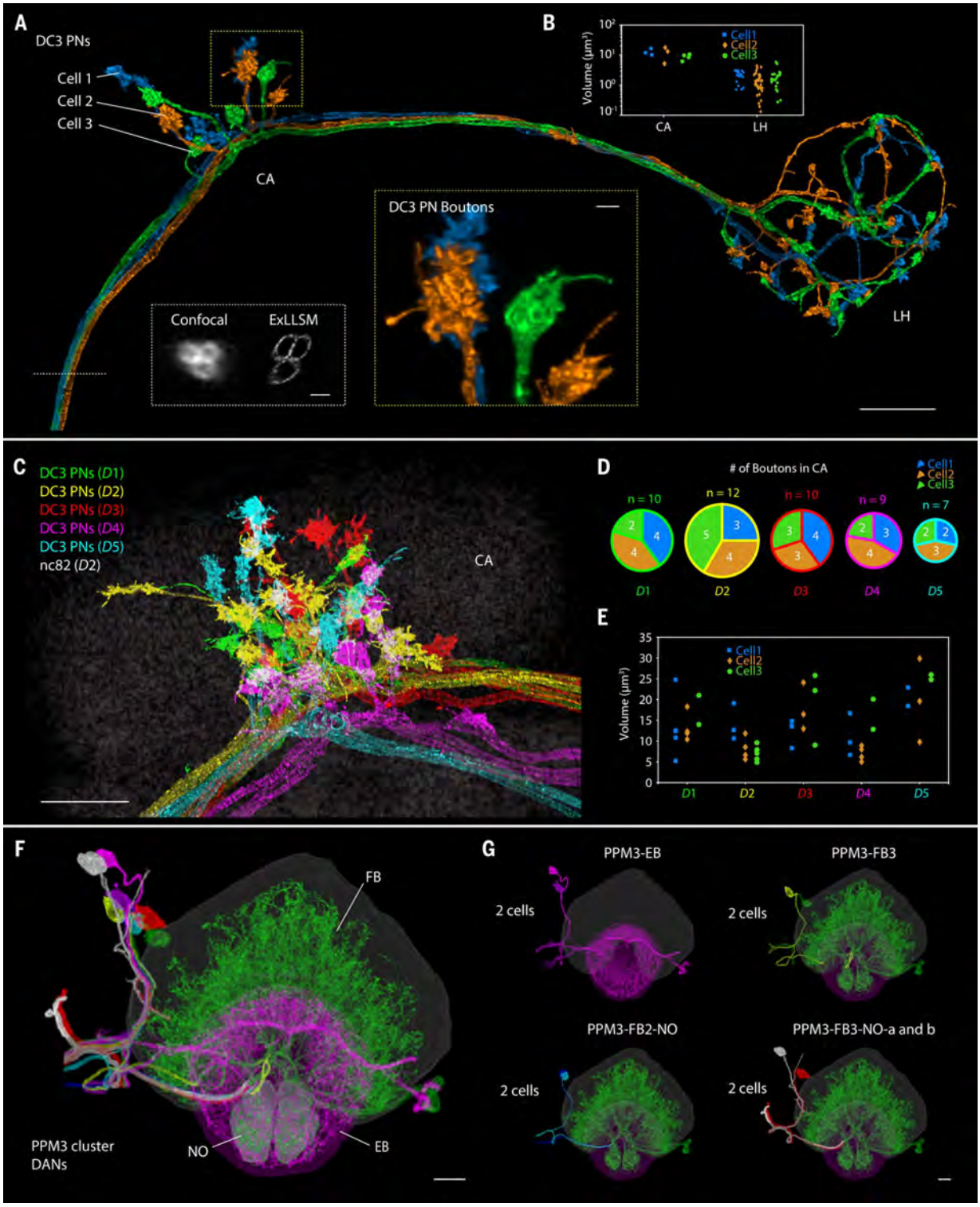

Fig. 6. Long-range tracing and stereotypy of neuron bundles in *Drosophila*. (**A**) MIP view of DC3 olfactory projection neurons (PNs) projecting from the antenna lobe of an adult *Drosophila* brain and partially traced here (Movie 7) to the calyx (CA) and lateral horn (LH). Scale bar, 10 μm. (Inset) (White box) Comparison of cross-sectional views of the axon bundle by means of (left) confocal microscopy and (right) ExLLSM. Scale bar, 1 μm. (Inset) (Yellow box) A magnified view of DC3 PN boutons in CA. Scale bar, 1 μm. (**B**) Volume of each individual DC3 PN bouton in CA and LH. (**C**) Overlaid MIP view of DC3 PNs from five adult *Drosophila* brains (D1 to D5) near CA. Scale bar, 10 μm. (**D**) Number of DC3 PN boutons in CA for D1 to D5 shown in (C). (**E**) Volume of DC3 PN boutons in CA for D1 to D5 shown in (C). (**F**) MIP view of individually traced PPM3 DANs in the right hemisphere of an adult *Drosophila* brain (Movie 8), innervating the fan-shaped body (FB) (green), ellipsoid body (EB) (magenta), and noduli (NO) (green). The fine neurites arborizing FB, EB, and NO are from both hemispheres of the brain. Scale bar, 10 μm. (**G**) MIP view of the identified cell types of PPM3 DANs (fig. S20). Scale bar, 10 μm.

Downloaded from http://science.sciencemag.org/ on January 17, 2019

four layer V neurons that could be traced to the white matter increased with increasing distance from the soma (Fig. 5C and fig. S18). By contrast, in layer VI only six axons were continuously myelinated, whereas two were completely unmyelinated, and three exhibited intermittent myelination with long unmyelinated segments more reminiscent of the layer II and III axons in the primary somatosensory cortex than the layer VI axons there (*70*). Thus, myelination patterns of axons in the primary visual cortex and the primary somatosensory cortex can differ, even for neurons in the same cortical layer.

Although the volumes of the somata and the diameters of the PMAS in layer V of the primary visual cortex were twice as large as those in layer VI (Fig. 5D and fig. S19, respectively), there was not a strong relationship between soma volume and myelination pattern (for example, intermittent or continuous) within layer VI (Fig. 5E). However, the PMAS lengths of the six continuously myelinated and the three intermittently myelinated axons in layer VI of the primary visual cortex split into distinct populations (Fig. 5F), with the intermittent ones of mean length (30.3 ± 1.7 μm) similar to the axons of layer V, and the continuous ones more than twice as long (70.6 ± 3.6 μm). Thus, continuously myelinated axons in different layers of the primary visual cortex need not have similar PMAS lengths. Given that the distal end of the PMAS is the site of AP initiation (*74*), perhaps PMAS length might be one mechanism by which neurons control the AP to account for differences in myelination or overall axon length in different layers and cortical regions.

Long-range tracing of clustered neurons in *Drosophila* and their stereotypy

Although millimeter-scale tissue sections present no problem for LLSM, the entire mouse brain is far too large, given the short working distances of commercially available high-resolution objectives. The brain of the fruitfly *D. melanogaster*, on the other hand, fits comfortably within the microscope, even in its 4× expanded form. Furthermore, a vast array of genetic tools have been developed for *Drosophila*, such as split-GAL4 drivers and MultiColor FlipOut (MCFO) (*17*), which enable precise labeling of user-selected subsets of its ~100,000 neurons, such as the dorsal paired medial (DPM) neurons that innervate the mushroom bodies (MBs) (movie S3). Fluorescence imaging of thousands of such subsets across thousands of transgenic flies and collation of the results then yields brain-wide 3D reconstructions of complete neural networks at single-cell resolution (*8*, *9*). However, to trace fine neuronal processes and identify synaptic connections, nanoscale resolution is needed. For all these reasons, the *Drosophila* brain is well matched to the capabilities of ExLLSM.

We thus chose to start with a relatively simple case: three olfactory projection neurons (PNs) originating at the DC3 glomerulus of the antennal lobes that feed most prominent sensory inputs to the calyx (CA) of the MB and lateral horn (LH) (*75*, *76*). Imaging a ~250- by 175- by 125-μm volume, we were able to trace the axonal branches of all three DC3 PNs across one hemisphere (Fig. 6A and Movie 7), although tracing of fine dendritic processes was still difficult at 4× expansion. We were also able to precisely assign boutons to each cell within the CA (cell 1, 3 boutons; cell 2, 3 boutons; cell 3, 4 boutons) and the LH (cell 1, 19 boutons; cell 2, 32 boutons; cell 3, 23 boutons) and determine the shapes and sizes of the boutons in these regions (Fig. 6B).

The neuronal circuits of the olfactory pathways to the MB have been extensively described by using light microscopy and have been reconstructed completely in the L1 instar larva and partially in the adult brain by using EM (*5*, *77*). However, the variation among individual animals has not been well studied at the level of detailed subcellular circuitry. The speed of ExLLSM now makes this possible. We studied the stereotypy of DC3 PNs by comparing their morphologies in the CA across five different animals (Fig. 6C). As expected, we consistently observed the restriction of boutons to the ends of the neurites in CA. However, we found that both the number and size of boutons differed among the three cells from the same hemisphere as well as between animals. For example, the total number of boutons in CA varied from 7 to 12, and none of the bouton assignments to each cell was the same among all five brains studied (Fig. 6D). The bouton size also showed substantial variability among the brains (Fig. 6E). These variations might arise from the distinct developmental histories of the individual animals. It is not yet clear whether they also indicate differences in synaptic strength and connection with Kenyon cells or how they might affect processing of olfactory information for associative learning in the MB. ExLLSM will enable such questions to be answered, thanks to its high throughput and its precise descriptions of neuronal morphology.

Given our success with this relatively simple example, we next applied ExLLSM to a much more challenging sample by imaging a ~340- by 660- by 90-μm volume covering nearly the entire brain of a TH-GAL4 transgenic *Drosophila* specimen. The sample was immunostained in one color against the membranes of all dopaminergic neurons (DANs) and in a second color with nc82 antibodies against Bruchpilot (Brp), a major structural and functional component of presynaptic active zones (AZs) (*78*, *79*). Among the ~110 DANs within the image volume, we focused our efforts on tracing the protocerebral posterior medial 3 (PPM3) cluster of DANs that project to the central complex, a key brain region essential for navigation, visual memory, sleep, and aggression (*80*–*82*). With manual annotation, we identified and traced all eight

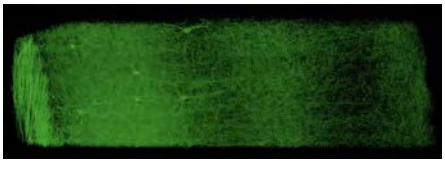

Movie 5. Neuronal processes and myelination patterns across the mouse primary visual cortex. Thy1-YFP–expressing neurons across 1100 by 280 by 83 μm, immunostained against myelin and Caspr, a marker of the nodes of Ranvier, with specific emphasis on the neuronal processes and longitudinal myelination profile of a selected layer V pyramidal neuron (Figs. 4 and 5 and figs. S18 and S19).

Movie 6. Segmentation of pyramidal neurons in layer V of the mouse primary visual cortex. Segmentation of two neurons, with specific emphasis on their branches and axonal myelination patterns (Fig. 4 and 5 and figs. S18 and S19).

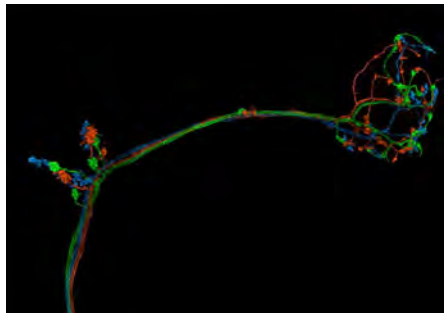

Movie 7. Tracing of DC3 olfactory projection neurons (PNs) in an adult *Drosophila* brain. Volumetric view of three individually traced neurons projecting from the antenna lobe in a bundle, with magnified views of their boutons at the calyx and lateral horn (Fig. 6, A to E).

Downloaded from http://science.sciencemag.org/ on January 17, 2019

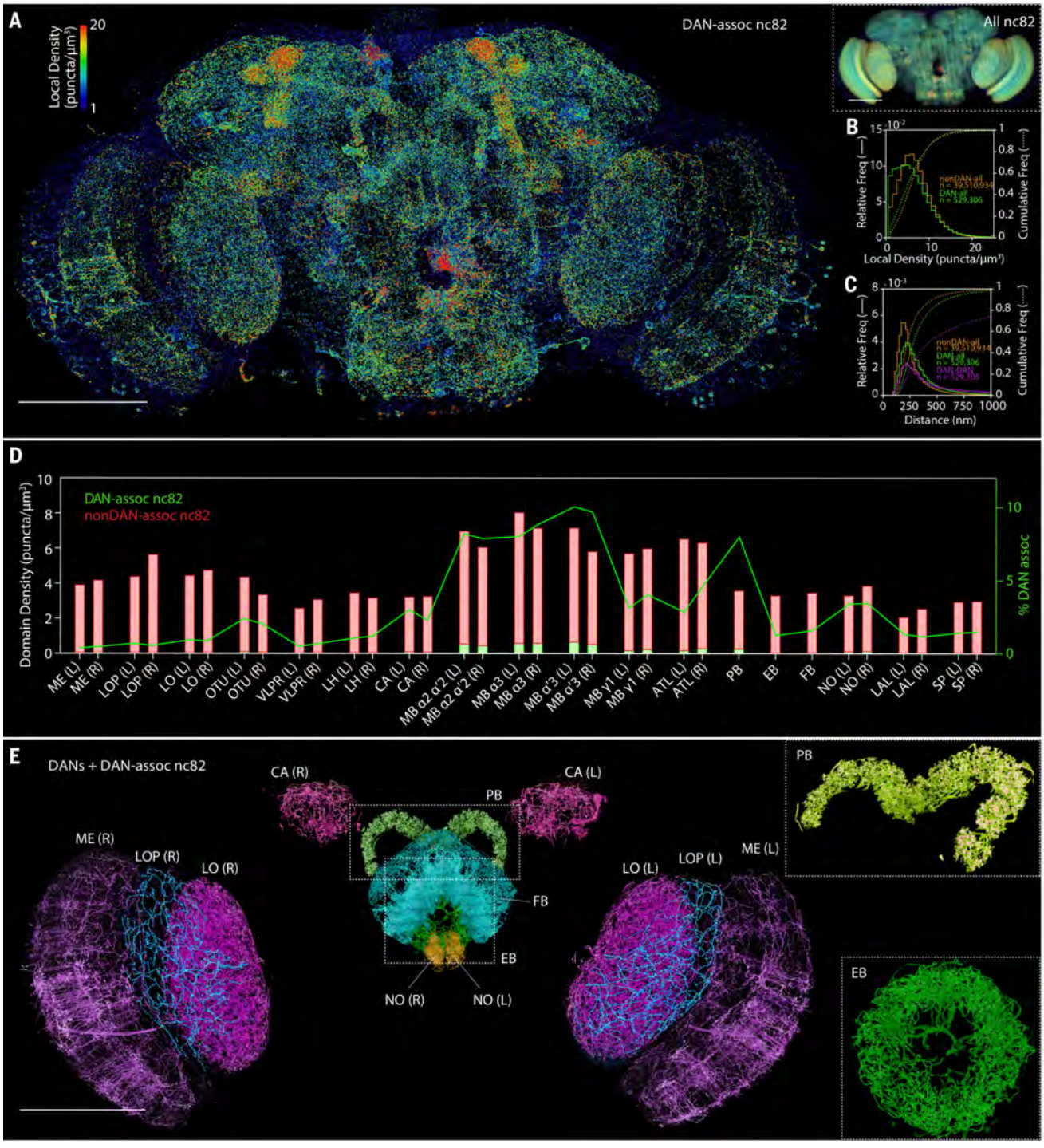

Fig. 7. Whole-brain analysis of presynaptic sites and DANs in *Drosophila*. (**A**) MIP view of the subset of nc82 puncta marking presynaptic sites that are associated with DANs (DAN-assoc nc82), color coded by the local puncta density, in an adult *Drosophila* brain (Movie 9). Scale bar, 100 µm. (Inset) (Right) MIP view of all nc82 puncta, using identical color coding of local density. Scale bar, 100 µm. (**B**) Distribution of local densities of (green) DAN-associated nc82 puncta and (orange) nonDAN-associated nc82 puncta in (A) (fig. S28). (**C**) Distribution of distances from DAN-associated nc82 puncta (green) and nonDAN-associated nc82 puncta (orange) to the nearest nc82 punctum of any kind, and nearest-neighbor distances from one DAN-associated nc82 to another (magenta) (fig. S29). (**D**) Volumetric density of DAN-associated nc82 puncta (green bars) and nonDAN-associated nc82 puncta (red bars), and the percentage of nc82 puncta that are DAN-associated (green curve), within each of the 33 brain regions of the adult *Drosophila* brain (fig. S30). (**E**) MIP view of DANs and DAN-associated nc82 puncta, color coded by 13 representative brain region (Movie 10). Scale bar, 100 µm. (Insets) Magnified views of the (top, angled view) PB and (bottom) EB. Brain regions are ME, medulla; LOP, lobula plate; LO, lobula; OTU, optical tubercle; VLPR, ventrolateral protocerebrum; LH, lateral horn; CA, calyx; MB, mushroom body; ATL, antler; PB, protocerebral bridge; EB, ellipsoid body; FB, fan-shaped body; NO, noduli; LAL, lateral accessory lobe; and SP, superior protocerebrum. "L" and "R" indicate the left and right hemispheres of the brain, respectively.

Downloaded from http://science.sciencemag.org/ on January 17, 2019

individual cells within the cluster (Fig. 6F, figs. S20 and S21, Movie 8, table S5, and movie S4). Although tracing of fine processes inside the central complex was difficult, we were able to trace the main axonal branches and precisely determine the number of cell types and the number of cells belonging to each cell type. Within the PPM3 cluster, we found that two cells (PPM3-EB) mainly projected to the ellipsoid body (EB) (*82*); two cells (PPM3-FB3) projected to layer 3 of the fan-shaped body (FB); two cells (PPM3-FB2-NO) projected to layer 2 of the FB and noduli (NO); and two cells, which could be further categorized into two cell types (PPM3-FB3-NO-a and PPM3-FB3-NO-b), projected to layer 3 of the FB and NO (Fig. 6G, figs. S20 and S21, table S5, and supplementary note 6f). Using stochastic labeling of individual neurons and split-GAL4 intersection, we were able to identify and confirm the individual cell types we assigned (figs. S20 and S21, table S5, and supplementary note 6f).

Whole-brain analysis of presynaptic sites and DANs

We next turned our attention to the nc82 channel of this specimen because recent EM measurements of the nearest-neighbor distances between synapses in the α lobe of the MB (fig. S22) (*83*) suggest that quantitative counting of synapses across the *Drosophila* brain should be possible with ExLLSM at 4× expansion. However, to have confidence in the results, we needed to show that nc82 puncta larger than 100 nm represented true AZs and not nonfunctional Brp monomers or nonspecific background. To do so, we imaged two additional nc82-stained brains: one coimmunostained against V5-tagged Brp and the other coimmunostained against the AZ protein Syd1 (supplementary note 6c) (*84*, *85*). In both cases, the distribution of distances from each nc82 punctum to its nearest costained neighbor was consistent with their mutual incorporation in a single AZ (fig. S23). In addition, we imaged another brain sample of the output neuron from the α1 compartment of the MB (MBON-α1) to validate the specificity of nc82 antibody. We measured a 70-fold–higher surface density of nc82 puncta at the axons and boutons of MBON-α1 than at its dendrites (fig. S24 and supplementary note 6d), which is consistent with the near-absence of dendritic presynaptic densities observed for the same neuron with EM (*83*). Furthermore, we counted ~44,000 nc82 puncta in the α3 compartment (fig. S25), compared with ~34,000 presynaptic densities in the EM study (fig. S22 and supplementary note 6e). The distribution of distances between the presynaptic densities was also similar in the two cases (figs. S22B and S25B).

To see whether these differences were within typical specimen variability, we imaged three additional wild-type females and counted between ~34,000 and ~49,000 n82 puncta in the α3 compartments of four MBs (fig. S26). Conversely, for the two animals in which we studied both α3 compartments (the original TH-GAL4 specimen and the wild type), the number of nc82 puncta in the left and right compartments were within ~10% of one another. This suggests that the variability we observed between animals, including the EM result, is indeed natural and not due to errors from our counting methodology.

Given confidence from these results, we then extended our analysis across nearly the entire brain (the medial lobes of the MB were not imaged because TH-GAL4 does not express in the DANs in that region). In total, we counted ~40 million nc82 puncta, ~530,000 of them localized at DANs (Fig. 7A and Movie 9), and calculated the brain-wide distribution of puncta density (Fig. 7B) and nearest-neighbor distances between any puncta or only DAN-associated ones (Fig. 7C).

We observed substantial differences when we further subdivided our analysis into 33 major brain regions (fig. S28 to S30 and table S6). The volume density of all puncta, for example, varied from ~2 to 3 per cubic micrometer in the lateral accessory lobe (LAL) and superior protocerebrum (SP) to ~6 to 8 in the compartments of the MB (Fig. 7D), perhaps reflecting the distinct computational needs of different brain regions. The high density in the MB, for example, is likely beneficial for increasing capacity and sensory specificity of memory in associative learning.

When focusing on only those nc82 puncta associated with DANs, we found additional differences. For example, the distance between non-DAN nc82 puncta and DAN-associated nc82 puncta differed substantially between brain regions (fig. S29), indicating that the proportion of synapses that can be modulated by dopamine may differ between brain regions. We also found that the percentage of puncta associated with DANs was approximately 10-fold higher in the MB than in the optic lobes (Fig. 7D), which is consistent with dopamine-dependent heterosynaptic plasticity being the basis of associative learning in the MB (*83*, *86*, *87*). On the other hand, the FB and the EB, which are known for visual and place memory formation (*88*), exhibited surprisingly low DAN association, whereas the protocerebral bridge (PB) and the antler (ATL), which are not particularly known for heterosynaptic plasticity, showed high DAN association second only to the MB. Despite these differences, the variation in surface density of nc82 puncta on DANs in different brain regions was considerably less pronounced (fig. S30B) because the percentage volume occupied by DAN in each domain (fig. S30D) followed similar trends to the percentage of DAN-associated puncta (Fig. 7D). This could also be seen directly in volume renderings of the DANs and DAN-associated puncta in each brain region (Fig. 7E and Movie 10), although local intradomain variations in the spatial distribution of nc82 were also seen.

Discussion

Thanks to its combination of high imaging speed, low photobleaching rate, and 3D nanoscale resolution, ExLLSM extends, by at least 1000-fold in volume, the ability of SR fluorescence microscopy to generate detailed images of subcellular ultrastructure. This fills a valuable niche between the high throughput of conventional optical pipelines of neural anatomy

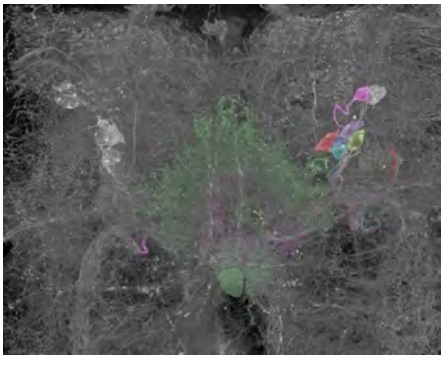

Movie 8. Tracing and classification of PPM3 dopaminergic neurons (DANs) in an adult *Drosophila* brain. Section of brain near the central complex with eight neurons from the protocerebral posterior medial 3 (PPM3) cluster in the right hemisphere (colored) shown in relation to surrounding DANs (white), and tracing of the individual neurons to their paired innervations in different regions of the central complex (Fig. 6, F and G, and figs. S20 and S21).

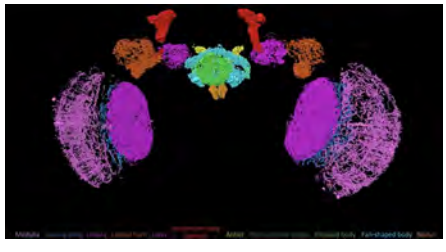

Movie 9. Local density map of DAN-associated presynaptic sites across an adult *Drosophila* brain. Color-coded brain regions and 3D color-coded map of the local density of DAN-associated nc82 puncta in each domain (Fig. 7, A to D, and figs. S28 to S30).

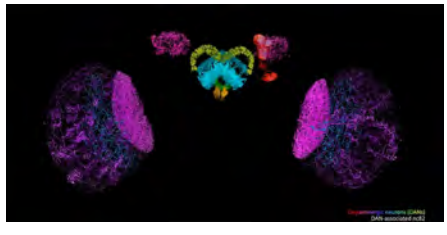

Movie 10. DANs and DAN-associated presynaptic sites in different brain regions of an adult *Drosophila* brain. Volume rendered DANs, DAN-associated nc82 puncta, and all nc82 puncta across the entire brain, color coded by brain region, followed by magnified 3D and orthoslice views of DANs and DAN-associated nc82 in each of nine different domains (Fig. 7E).

Downloaded from http://science.sciencemag.org/ on January 17, 2019

(8, 9) and the ultrahigh resolution of corresponding EM pipelines (5, 70, 83). With genetically targeted cell type–specific labeling (17, 89–91) and protein-specific immunostaining, ExLLSM enables sparse neural subsets and dense synaptic connections to be recorded, visualized, and quantified at ~60- by 60- by 90-nm resolution with ~100 person-hours of effort over cortex-spanning volumes in the mouse or brain-wide volumes in *Drosophila*. This compares with 5 weeks to image and ~16,000 person-hours to trace all neurons and count all synapses in a volume only 1/80th of a fly brain encompassing the α lobe of the MB in a recent EM study at 8-nm isotropic resolution (83). The fluorescence contrast of ExLLSM also raises the possibility of correlating (92) fluorescence-based genetic indicators of neural activity (93, 94) with neural ultrastructure over much larger volumes and without the labeling compromises common to correlative EM/fluorescence studies (95).

Although we have focused on the mouse cortex and the *Drosophila* brain in this work, we have also applied ExLLSM to image the mossy fiber innervation of granule cells in glomeruli in the cerebellum of the mouse (fig. S31 and movie S5) as well as a complete human kidney glomerulus section (fig. S32). However, the application of ExM to any biological system must be examined on a case-by-case basis through careful controls and comparisons with known aspects (such as with EM) of the specific ultrastructural elements under investigation. In particular, extrapolating the faithful nanoscale expansion of delicate membranous structures and vesicles in a specimen from images of more robust components such as cytoskeletal elements, clathrin-coated pits, or nuclear histones (18, 29, 96, 97) should be avoided. Elastic inhomogeneity of the specimen after digestion, such as from collagen-rich connective tissue or adhesion to a rigid substrate, can also interfere with expansion, although newer protocols with more aggressive digestion may help (98). In this regard, brain tissue may represent a best case for ExM studies, owing to its comparatively homogenous mechanical properties and ready digestion. It should always be remembered that any image of a once-living specimen is an imperfect representation of that specimen, and the more steps that intrude in the process from one to the other the more imperfect it becomes. Overexpression, chemical fixation, permeabilization, and immunostaining already introduce numerous structural artifacts (99–101) in all forms of high-resolution fluorescence microscopy, including ExM, but ExM also requires additional steps of polymer infusion, gelation, label attachment, digestion, expansion, and handling that can perturb ultrastructure even more. Careful controls are essential.

At 4× expansion, the resolution of ExLLSM is close, but not quite sufficient, to trace fine, highly innervated neuronal processes—such as the PPM3 cluster, which terminates in the central complex—and would therefore benefit from higher expansion ratios. However, even if specimen-wide isotropic expansion can be validated at higher ratios with newer protocols of iterated expansion (29), ExM is still heir to the problems that bedevil other forms of high-resolution fluorescence microscopy. Chief among these is that because of the stochastic nature of labeling, the mean separation between fluorophores must be ~5× to 10× smaller than the desired resolution in each dimension in order to distinguish with high confidence two or more structures for which no a priori knowledge exists (102). We met this requirement at the level of ~60- by 60- by 90-nm resolution in most cases owing to the dense expression of cytosolic label in Thy1-YFP transgenic mice and DAN membrane label in a TH-GAL4 transgenic fly, as well as the exceptional specificity of Abs targeting MBP and nc82. Other Abs in our study did not meet this standard but were sufficient to identify organelles responsible for voids of cytosolic label, mark Homer1 at synapses and Caspr at nodes of Ranvier, and measure statistical distributions of synapse breadth and pre- and post-synaptic separation. However, immunostaining in any form is probably not dense enough to achieve true 3D resolution much beyond that already obtainable at 4× expansion, and the long distance between epitope and fluorophore, particularly with secondary Abs, further limits resolution. Likewise, loss of FP fluorescence upon linking and digestion, as well as the slow continued loss of fluorescence, which we alleviated here with a highly basic imaging buffer (supplementary note 2, c and d), probably preclude study at high resolution of many FP-linked proteins at the endogenous levels produced through genome editing. Indeed, even at 4× expansion, we rarely found sufficient residual fluorescence to image targets labeled with red FPs of the *Anthozoa* family, despite reports to the contrary (19).

Despite these challenges and limitations, the high speed and nanometric 3D resolution of ExLLSM make it an attractive tool for comparative anatomical studies, particularly in the *Drosophila* brain. For example, although we imaged the entire TH-GAL4/nc82 brain in 62.5 hours (3.2×10^5 μm^3/hour), with subsequent improvements in scanning geometry and field of view (FOV) we imaged mouse brain tissue in two colors at 4.0×10^6 μm^3/hour. If transferrable to the fly, this would allow whole-brain imaging in ~5.0 hours. This limit is not fundamental; with simultaneous multicolor imaging and multiple cameras to cover even broader FOVs, rates up to ~10^8 μm^3/hour may be achievable, or ~12 min/fly brain at 4× expansion. Assuming the future development of (i) robust, isotropic expansion at 10× or greater; (ii) longer working distance high NA water immersion objectives or lossless sectioning (103) of expanded samples; and (iii) a ubiquitous, dense, and cell-permeable fluorescent membrane stain analogous to heavy-metal stains in EM, even densely innervated circuits might be traced, particularly when imaged in conjunction with cell type–specific or stochastically expressed multicolor labels for error checking (104). With such a pipeline in place, 10 or more specimens might be imaged in a single day at 4× to 10× expansion, enabling statistically rich, brain-wide studies with protein-specific contrast and nanoscale resolution of neural development, sexual dimorphism, degree of stereotypy, and structure/function or structure/behavior correlations, particularly under genetic or pharmacological perturbation.

Materials and methods

Preparation of ExM samples

Mouse, *D. melanogaster*, and human samples were dissected, fixed, and immunostained following the protocols in supplementary note 1. Sample genotypes and antibodies are summarized in table S2. Unless otherwise noted, all samples were processed by using a protein-retention ExM (proExM) protocol with minor modifications (19, 105) or an expansion pathology (ExPath) protocol (98). Prepared ExM samples were stored in 1× phosphate-buffered saline at 4°C and expanded in doubly deionized water immediately before imaging with LLSM.

Lattice light-sheet imaging

With the exception of Fig. 1, all ExM samples were imaged in objective scan mode (20) by using a LLSM described previously (106), except with adaptive optics capability disabled. The ExM sample in the left column of Fig. 1 was imaged by using a LLSM optimized for ExM, featuring a broader 160-μm FOV, a 1.5-mm scan range, and software optimized for rapid sample scan acquisition (supplementary note 2a). All expanded samples were large compared with the LLS FOV and were therefore imaged in a series of overlapping 3D tiles that covered the desired sample volume (supplementary note 2b). For imaging sessions of several hours or more, focus was maintained through the periodic imaging of reference beads (supplementary note 2c). Raw data from each tile were deskewed (for sample scan mode), flat-fielded, deconvolved, and stored for subsequent processing.

Computing pipeline for flat-field correction, stitching, and export of 3D image tiles

Because automatic tools for 3D stitching (107–111) do not scale to datasets with thousands of 3D image tiles, we developed a scalable high-performance computing (HPC) pipeline to robustly flat-field correct, deconvolve, and assemble 3D image tiles into the final volume (supplementary note 3). First, we extended and parallelized CIDRE (107) for 3D volumes to calculate 3D flat fields (figs. S5 and S6). We then corrected the raw image tiles using these flat-fields and deconvolved each. Next, we parallelized the globally optimizing 3D stitching method (108) to automatically stitch the thousands of raw image tiles, without manual intervention, in an iteratively refined prediction model that corrects for systematic stage coordinate errors (fig. S7). Last, we exported the stitched datasets using the flat-field–corrected and deconvolved image tiles as multiresolution hierarchies

Downloaded from http://science.sciencemag.org/ on January 17, 2019

into a custom file format (N5) (*21*) that enabled parallel blockwise export and compression on a HPC cluster. Bindings for N5 format for the ImgLib2 library (*112*) are provided for the ImageJ distribution Fiji (*113*). For interactive visualization, we developed a BigDataViewer-based viewer plugin (*114*) including a crop and export tool to make arbitrary subvolumes available in legacy formats such as TIFF image series.

REFERENCES AND NOTES

1. S. Herculano-Houzel, The human brain in numbers: A linearly scaled-up primate brain. *Front. Hum. Neurosci.* **3**, 31 (2009). doi: 10.3389/neuro.09.031.2009; pmid: 19915731
2. K. Sharma *et al.*, Cell type- and brain region-resolved mouse brain proteome. *Nat. Neurosci.* **18**, 1819–1831 (2015). doi: 10.1038/nn.4160; pmid: 26523646
3. J. E. Heuser, T. S. Reese, Evidence for recycling of synaptic vesicle membrane during transmitter release at the frog neuromuscular junction. *J. Cell Biol.* **57**, 315–344 (1973). doi: 10.1083/jcb.57.2.315; pmid: 4348786
4. C. S. Xu *et al.*, Enhanced FIB-SEM systems for large-volume 3D imaging. *eLife* **6**, e25916 (2017). doi: 10.7554/eLife.25916; pmid: 28500755
5. Z. Zheng *et al.*, A complete electron microscopy volume of the brain of adult *Drosophila melanogaster*. *Cell* **174**, 730–743.e22 (2018). doi: 10.1016/j.cell.2018.06.019; pmid: 30033368
6. K. D. Micheva, S. J. Smith, Array tomography: A new tool for imaging the molecular architecture and ultrastructure of neural circuits. *Neuron* **55**, 25–36 (2007). doi: 10.1016/j.neuron.2007.06.014; pmid: 17610815
7. J.-C. Rah *et al.*, Thalamocortical input onto layer 5 pyramidal neurons measured using quantitative large-scale array tomography. *Front. Neural Circuits* **7**, 177 (2013). doi: 10.3389/fncir.2013.00177; pmid: 24273494
8. A. S. Chiang *et al.*, Three-dimensional reconstruction of brain-wide wiring networks in *Drosophila* at single-cell resolution. *Curr. Biol.* **21**, 1–11 (2011). doi: 10.1016/j.cub.2010.11.056; pmid: 21129968
9. A. Jenett *et al.*, A GAL4-driver line resource for *Drosophila* neurobiology. *Cell Reports* **2**, 991–1001 (2012). doi: 10.1016/j.celrep.2012.09.011; pmid: 23063364
10. M. N. Economo *et al.*, A platform for brain-wide imaging and reconstruction of individual neurons. *eLife* **5**, e10566 (2016). doi: 10.7554/eLife.10566; pmid: 26796534
11. S. Shah, E. Lubeck, W. Zhou, L. Cai, In situ transcription profiling of single cells reveals spatial organization of cells in the mouse hippocampus. *Neuron* **92**, 342–357 (2016). doi: 10.1016/j.neuron.2016.10.001; pmid: 27764670
12. J. R. Moffitt *et al.*, High-throughput single-cell gene-expression profiling with multiplexed error-robust fluorescence in situ hybridization. *Proc. Natl. Acad. Sci. U.S.A.* **113**, 11046–11051 (2016). doi: 10.1073/pnas.1612826113; pmid: 27625426
13. J. Tønnesen, U. V. Nägerl, Superresolution imaging for neuroscience. *Exp. Neurol.* **242**, 33–40 (2013). doi: 10.1016/j.expneurol.2012.10.004; pmid: 23063602
14. H. Zhong, Applying superresolution localization-based microscopy to neurons. *Synapse* **69**, 283–294 (2015). doi: 10.1002/syn.21806; pmid: 25648102
15. C. I. Bargmann, Beyond the connectome: How neuromodulators shape neural circuits. *BioEssays* **34**, 458–465 (2012). doi: 10.1002/bies.201100185; pmid: 22396302
16. J. Lu, J. C. Tapia, O. L. White, J. W. Lichtman, The interscutularis muscle connectome. *PLOS Biol.* **7**, e32 (2009). pmid: 19209956
17. A. Nern, B. D. Pfeiffer, G. M. Rubin, Optimized tools for multicolor stochastic labeling reveal diverse stereotyped cell arrangements in the fly visual system. *Proc. Natl. Acad. Sci. U.S.A.* **112**, E2967–E2976 (2015). doi: 10.1073/pnas.1506763112; pmid: 25964354
18. F. Chen, P. W. Tillberg, E. S. Boyden, Expansion microscopy. *Science* **347**, 543–548 (2015). doi: 10.1126/science.1260088; pmid: 25592419
19. P. W. Tillberg *et al.*, Protein-retention expansion microscopy of cells and tissues labeled using standard fluorescent proteins and antibodies. *Nat. Biotechnol.* **34**, 987–992 (2016). doi: 10.1038/nbt.3625; pmid: 27376584
20. B. C. Chen *et al.*, Lattice light-sheet microscopy: Imaging molecules to embryos at high spatiotemporal resolution. *Science* **346**, 1257998 (2014). doi: 10.1126/science.1257998; pmid: 25342811
21. I. Pisarev, S. Saalfeld, Stitcher and N5 viewer; https://github.com/saalfeldlab/stitching-spark, https://github.com/saalfeldlab/n5-viewer.
22. J. Tønnesen, V. V. G. K. Inavalli, U. V. Nägerl, Super-resolution imaging of the extracellular space in living brain tissue. *Cell* **172**, 1108–1121.e15 (2018). doi: 10.1016/j.cell.2018.02.007; pmid: 29474910
23. L. Freifeld *et al.*, Expansion microscopy of zebrafish for neuroscience and developmental biology studies. *Proc. Natl. Acad. Sci. U.S.A.* **114**, E10799–E10808 (2017). doi: 10.1073/pnas.1706281114; pmid: 29162696
24. T. J. Mosca, D. J. Luginbuhl, I. E. Wang, L. Luo, Presynaptic LRP4 promotes synapse number and function of excitatory CNS neurons. *eLife* **6**, e27347 (2017). doi: 10.7554/eLife.27347; pmid: 28606304
25. C. K. Cahoon *et al.*, Superresolution expansion microscopy reveals the three-dimensional organization of the *Drosophila* synaptonemal complex. *Proc. Natl. Acad. Sci. U.S.A.* **114**, E6857–E6866 (2017). doi: 10.1073/pnas.1705623114; pmid: 28760978
26. A. Tsai *et al.*, Nuclear microenvironments modulate transcription from low-affinity enhancers. *eLife* **6**, e28975 (2017). doi: 10.7554/eLife.28975; pmid: 29095143
27. N. Jiang *et al.*, Superresolution imaging of *Drosophila* tissues using expansion microscopy. *Mol. Biol. Cell* **29**, 1413–1421 (2018). doi: 10.1091/mbc.E17-10-0583; pmid: 29688792
28. F. Guo, M. Holla, M. M. Diaz, M. Rosbash, A circadian output circuit controls sleep-wake arousal threshold in *Drosophila*. *bioRxiv* (2018). doi: 10.1101/298067
29. J. B. Chang *et al.*, Iterative expansion microscopy. *Nat. Methods* **14**, 593–599 (2017). doi: 10.1038/nmeth.4261; pmid: 28417997
30. C. J. L. Sheppard, Super resolution in confocal imaging. *Optik (Stuttg.)* **80**, 53–54 (1988).
31. C. B. Müller, J. Enderlein, Image scanning microscopy. *Phys. Rev. Lett.* **104**, 198101 (2010). doi: 10.1103/PhysRevLett.104.198101; pmid: 20867000
32. X.-T. Cheng *et al.*, Characterization of LAMP1-labeled nondegradative lysosomal and endocytic compartments in neurons. *J. Cell Biol.* **217**, 3127–3139 (2018). doi: 10.1083/jcb.201711083; pmid: 29695488
33. N. Kasthuri *et al.*, Saturated reconstruction of a volume of neocortex. *Cell* **162**, 648–661 (2015). doi: 10.1016/j.cell.2015.06.054; pmid: 26232230
34. Q. A. Liu, H. Shio, Mitochondrial morphogenesis, dendrite development, and synapse formation in cerebellum require both Bcl-w and the glutamate receptor δ2. *PLOS Genet.* **4**, e1000097 (2008). doi: 10.1371/journal.pgen.1000097; pmid: 18551174
35. W. Kuehnel, *Color Atlas of Cytology, Histology, and Microscopic Anatomy* (Thieme Flexibook, ed. 4, 2003).
36. V. Popov, N. I. Medvedev, H. A. Davies, M. G. Stewart, Mitochondria form a filamentous reticular network in hippocampal dendrites but are present as discrete bodies in axons: A three-dimensional ultrastructural study. *J. Comp. Neurol.* **492**, 50–65 (2005). doi: 10.1002/cne.20682; pmid: 16175555
37. M. R. Duchen, Mitochondria in health and disease: Perspectives on a new mitochondrial biology. *Mol. Aspects Med.* **25**, 365–451 (2004). doi: 10.1016/j.mam.2004.03.001; pmid: 15302203
38. S. G. Waxman, M. V. I. Bennett, Relative conduction velocities of small myelinated and non-myelinated fibres in the central nervous system. *Nat. New Biol.* **238**, 217–219 (1972). doi: 10.1038/newbio238217a0; pmid: 4506206
39. K. A. Nave, Myelination and support of axonal integrity by glia. *Nature* **468**, 244–252 (2010). doi: 10.1038/nature09614; pmid: 21068833
40. J. J. Harris, D. Attwell, The energetics of CNS white matter. *J. Neurosci.* **32**, 356–371 (2012). doi: 10.1523/JNEUROSCI.3430-11.2012; pmid: 22219296
41. A. Compston, A. Coles, Multiple sclerosis. *Lancet* **372**, 1502–1517 (2008). doi: 10.1016/S0140-6736(08)61620-7; pmid: 18970977
42. W. A. H. Rushton, A theory of the effects of fibre size in medullated nerve. *J. Physiol.* **115**, 101–122 (1951). doi: 10.1113/jphysiol.1951.sp004655; pmid: 14889433
43. R. La Marca *et al.*, TACE (ADAM17) inhibits Schwann cell myelination. *Nat. Neurosci.* **14**, 857–865 (2011). doi: 10.1038/nn.2849; pmid: 21666671
44. L.-J. Oluich *et al.*, Targeted ablation of oligodendrocytes induces axonal pathology independent of overt demyelination. *J. Neurosci.* **32**, 8317–8330 (2012). doi: 10.1523/JNEUROSCI.1053-12.2012; pmid: 22699912
45. M. Zonouzi *et al.*, GABAergic regulation of cerebellar NG2 cell development is altered in perinatal white matter injury. *Nat. Neurosci.* **18**, 674–682 (2015). doi: 10.1038/nn.3990; pmid: 25821912
46. O. O. Glebov, S. Cox, L. Humphreys, J. Burrone, Neuronal activity controls transsynaptic geometry. *Sci. Rep.* **6**, 22703 (2016). doi: 10.1038/srep22703; pmid: 26951792
47. A. Dani, B. Huang, J. Bergan, C. Dulac, X. Zhuang, Superresolution imaging of chemical synapses in the brain. *Neuron* **68**, 843–856 (2010). doi: 10.1016/j.neuron.2010.11.021; pmid: 21144999
48. N. L. Rochefort, A. Konnerth, Dendritic spines: From structure to in vivo function. *EMBO Rep.* **13**, 699–708 (2012). doi: 10.1038/embor.2012.102; pmid: 22791026
49. H. Hering, M. Sheng, Dendritic spines: Structure, dynamics and regulation. *Nat. Rev. Neurosci.* **2**, 880–888 (2001). doi: 10.1038/35104061; pmid: 11733795
50. E. A. Nimchinsky, B. L. Sabatini, K. Svoboda, Structure and function of dendritic spines. *Annu. Rev. Physiol.* **64**, 313–353 (2002). doi: 10.1146/annurev.physiol.64.081501.160008; pmid: 11826272
51. M. Segal, Dendritic spines and long-term plasticity. *Nat. Rev. Neurosci.* **6**, 277–284 (2005). doi: 10.1038/nrn1649; pmid: 15803159
52. S. Konur, D. Rabinowitz, V. L. Fenstermaker, R. Yuste, Systematic regulation of spine sizes and densities in pyramidal neurons. *J. Neurobiol.* **56**, 95–112 (2003). doi: 10.1002/neu.10229; pmid: 12838576
53. D. Dumitriu, A. Rodriguez, J. H. Morrison, High-throughput, detailed, cell-specific neuroanatomy of dendritic spines using microinjection and confocal microscopy. *Nat. Protoc.* **6**, 1391–1411 (2011). doi: 10.1038/nprot.2011.389; pmid: 21886104
54. M. Jiang *et al.*, Dendritic arborization and spine dynamics are abnormal in the mouse model of MECP2 duplication syndrome. *J. Neurosci.* **33**, 19518–19533 (2013). doi: 10.1523/JNEUROSCI.1745-13.2013; pmid: 24336718
55. X. Yu, Y. Zuo, Two-photon in vivo imaging of dendritic spines in the mouse cortex using a thinned-skull preparation. *J. Vis. Exp.* **87**, e51520 (2014). pmid: 24894563
56. J. I. Arellano, R. Benavides-Piccione, J. Defelipe, R. Yuste, Ultrastructure of dendritic spines: Correlation between synaptic and spine morphologies. *Front. Neurosci.* **1**, 131–143 (2007). doi: 10.3389/neuro.01.1.1.010.2007; pmid: 18982124
57. C. Bosch *et al.*, FIB/SEM technology and high-throughput 3D reconstruction of dendritic spines and synapses in GFP-labeled adult-generated neurons. *Front. Neuroanat.* **9**, 60 (2015). doi: 10.3389/fnana.2015.00060; pmid: 26052271
58. K. Takasaki, B. L. Sabatini, Super-resolution 2-photon microscopy reveals that the morphology of each dendritic spine correlates with diffusive but not synaptic properties. *Front. Neuroanat.* **8**, 29 (2014). doi: 10.3389/fnana.2014.00029; pmid: 24847215
59. J. Tønnesen, G. Katona, B. Rózsa, U. V. Nägerl, Spine neck plasticity regulates compartmentalization of synapses. *Nat. Neurosci.* **17**, 678–685 (2014). doi: 10.1038/nn.3682; pmid: 24657968
60. D. L. Dickstein *et al.*, Automatic dendritic spine quantification from confocal data with neurolucida 360. *Curr. Protoc. Neurosci.* **77**, 1, 21 (2016). doi: 10.1002/cpns.16; pmid: 27696360
61. E. G. Jones, T. P. S. Powell, Morphological variations in the dendritic spines of the neocortex. *J. Cell Sci.* **5**, 509–529 (1969). pmid: 5362339
62. J. Grutzendler, N. Kasthuri, W. B. Gan, Long-term dendritic spine stability in the adult cortex. *Nature* **420**, 812–816 (2002). doi: 10.1038/nature01276; pmid: 12490949
63. L. Anton-Sanchez *et al.*, Three-dimensional distribution of cortical synapses: A replicated point pattern-based analysis. *Front. Neuroanat.* **8**, 85 (2014). doi: 10.3389/fnana.2014.00085; pmid: 25206325
64. J. DeFelipe, L. Alonso-Nanclares, J. I. Arellano, Microstructure of the neocortex: Comparative aspects. *J. Neurocytol.* **31**, 299–316 (2002). doi: 10.1023/A:1024130211265; pmid: 12815249
65. C. Sala *et al.*, Regulation of dendritic spine morphology and synaptic function by Shank and Homer. *Neuron* **31**, 115–130 (2001). doi: 10.1016/S0896-6273(01)00339-7; pmid: 11498055

Downloaded from http://science.sciencemag.org/ on January 17, 2019

66. U. Thomas, Modulation of synaptic signalling complexes by Homer proteins. *J. Neurochem.* **81**, 407–413 (2002). doi: 10.1046/j.1471-4159.2002.00869.x; pmid: 12065649
67. A. Dosemeci, R. J. Weinberg, T. S. Reese, J.-H. Tao-Cheng, The postsynaptic density: There is more than meets the eye. *Front. Synaptic Neurosci.* **8**, 23 (2016). doi: 10.3389/fnsyn.2016.00023; pmid: 27594834
68. G. H. Diering *et al*., Homer1a drives homeostatic scaling-down of excitatory synapses during sleep. *Science* **355**, 511–515 (2017). doi: 10.1126/science.aai8355; pmid: 28154077
69. D. Debanne, E. Campanac, A. Bialowas, E. Carlier, G. Alcaraz, Axon physiology. *Physiol. Rev.* **91**, 555–602 (2011). doi: 10.1152/physrev.00048.2009; pmid: 21527732
70. G. S. Tomassy *et al*., Distinct profiles of myelin distribution along single axons of pyramidal neurons in the neocortex. *Science* **344**, 319–324 (2014). doi: 10.1126/science.1249766; pmid: 24744380
71. S. Einheber *et al*., The axonal membrane protein Caspr, a homologue of neurexin IV, is a component of the septate-like paranodal junctions that assemble during myelination. *J. Cell Biol.* **139**, 1495–1506 (1997). doi: 10.1083/jcb.139.6.1495; pmid: 9396755
72. C. Porrero, P. Rubio-Garrido, C. Avendaño, F. Clascá, Mapping of fluorescent protein-expressing neurons and axon pathways in adult and developing Thy1-eYFP-H transgenic mice. *Brain Res.* **1345**, 59–72 (2010). doi: 10.1016/j.brainres.2010.05.061; pmid: 20510892
73. S. Ramaswamy, H. Markram, Anatomy and physiology of the thick-tufted layer 5 pyramidal neuron. *Front. Cell. Neurosci.* **9**, 233 (2015). doi: 10.3389/fncel.2015.00233; pmid: 26167146
74. L. M. Palmer, G. J. Stuart, Site of action potential initiation in layer 5 pyramidal neurons. *J. Neurosci.* **26**, 1854–1863 (2006). doi: 10.1523/JNEUROSCI.4812-05.2006; pmid: 16467534
75. S. J. C. Caron, V. Ruta, L. F. Abbott, R. Axel, Random convergence of olfactory inputs in the Drosophila mushroom body. *Nature* **497**, 113–117 (2013). doi: 10.1038/nature12063; pmid: 23615618
76. N. J. Butcher, A. B. Friedrich, Z. Lu, H. Tanimoto, I. A. Meinertzhagen, Different classes of input and output neurons reveal new features in microglomeruli of the adult Drosophila mushroom body calyx. *J. Comp. Neurol.* **520**, 2185–2201 (2012). doi: 10.1002/cne.23037; pmid: 22237598
77. K. Eichler *et al*., The complete connectome of a learning and memory centre in an insect brain. *Nature* **548**, 175–182 (2017). doi: 10.1038/nature23455; pmid: 28796202
78. W. Fouquet *et al*., Maturation of active zone assembly by *Drosophila* Bruchpilot. *J. Cell Biol.* **186**, 129–145 (2009). doi: 10.1083/jcb.200812150; pmid: 19596851
79. N. Ehmann *et al*., Quantitative super-resolution imaging of Bruchpilot distinguishes active zone states. *Nat. Commun.* **5**, 4650 (2014). doi: 10.1038/ncomms5650; pmid: 25130366
80. Z. Mao, R. L. Davis, Eight different types of dopaminergic neurons innervate the *Drosophila* mushroom body neuropil: Anatomical and physiological heterogeneity. *Front. Neural Circuits* **3**, 5 (2009). doi: 10.3389/neuro.04.005.2009; pmid: 19597562
81. E. C. Kong *et al*., A pair of dopamine neurons target the D1-like dopamine receptor DopR in the central complex to promote ethanol-stimulated locomotion in *Drosophila*. *PLOS ONE* **5**, e9954 (2010). doi: 10.1371/journal.pone.0009954; pmid: 20376353
82. O. V. Alekseyenko *et al*., Single serotonergic neurons that modulate aggression in *Drosophila*. *Curr. Biol.* **24**, 2700–2707 (2014). doi: 10.1016/j.cub.2014.09.051; pmid: 25447998
83. S. Y. Takemura *et al*., A connectome of a learning and memory center in the adult *Drosophila* brain. *eLife* **6**, e26975 (2017). doi: 10.7554/eLife.26975; pmid: 28718765
84. D. Owald *et al*., A Syd-1 homologue regulates pre- and postsynaptic maturation in *Drosophila*. *J. Cell Biol.* **188**, 565–579 (2010). doi: 10.1083/jcb.200908055; pmid: 20176924
85. S. Holbrook, J. K. Finley, E. L. Lyons, T. G. Herman, Loss of syd-1 from R7 neurons disrupts two distinct phases of presynaptic development. *J. Neurosci.* **32**, 18101–18111 (2012). doi: 10.1523/JNEUROSCI.1350-12.2012; pmid: 23238725
86. Y. Aso *et al*., The neuronal architecture of the mushroom body provides a logic for associative learning. *eLife* **3**, e04577 (2014). doi: 10.7554/eLife.04577; pmid: 25535793
87. Y. Aso, G. M. Rubin, Dopaminergic neurons write and update memories with cell-type-specific rules. *eLife* **5**, e16135 (2016). doi: 10.7554/eLife.16135; pmid: 27441388
88. L. Kahsai, T. Zars, Learning and memory in *Drosophila*: Behavior, genetics, and neural systems. *Int. Rev. Neurobiol.* **99**, 139–167 (2011). doi: 10.1016/B978-0-12-387003-2.00006-9; pmid: 21906539
89. H. Luan, N. C. Peabody, C. R. Vinson, B. H. White, Refined spatial manipulation of neuronal function by combinatorial restriction of transgene expression. *Neuron* **52**, 425–436 (2006). doi: 10.1016/j.neuron.2006.08.028; pmid: 17088209
90. B. D. Pfeiffer *et al*., Refinement of tools for targeted gene expression in *Drosophila*. *Genetics* **186**, 735–755 (2010). doi: 10.1534/genetics.110.119917; pmid: 20697123
91. M. J. Dolan *et al*., Facilitating neuron-specific genetic manipulations in *Drosophila melanogaster* using a split GAL4 repressor. *Genetics* **206**, 775–784 (2017). doi: 10.1534/genetics.116.199687; pmid: 28363977
92. D. D. Bock *et al*., Network anatomy and in vivo physiology of visual cortical neurons. *Nature* **471**, 177–182 (2011). doi: 10.1038/nature09802; pmid: 21390124
93. T.-W. Chen *et al*., Ultrasensitive fluorescent proteins for imaging neuronal activity. *Nature* **499**, 295–300 (2013). doi: 10.1038/nature12354; pmid: 23868258
94. B. F. Fosque *et al*., Neural circuits. Labeling of active neural circuits in vivo with designed calcium integrators. *Science* **347**, 755–760 (2015). doi: 10.1126/science.1260922; pmid: 25678659
95. P. de Boer, J. P. Hoogenboom, B. N. G. Giepmans, Correlated light and electron microscopy: Ultrastructure lights up! *Nat. Methods* **12**, 503–513 (2015). doi: 10.1038/nmeth.3400; pmid: 26020503
96. T. J. Chozinski *et al*., Expansion microscopy with conventional antibodies and fluorescent proteins. *Nat. Methods* **13**, 485–488 (2016). doi: 10.1038/nmeth.3833; pmid: 27064647
97. T. Ku *et al*., Multiplexed and scalable super-resolution imaging of three-dimensional protein localization in size-adjustable tissues. *Nat. Biotechnol.* **34**, 973–981 (2016). doi: 10.1038/nbt.3641; pmid: 27454740
98. Y. Zhao *et al*., Nanoscale imaging of clinical specimens using pathology-optimized expansion microscopy. *Nat. Biotechnol.* **35**, 757–764 (2017). doi: 10.1038/nbt.3892; pmid: 28714966
99. U. Schnell, F. Dijk, K. A. Sjollema, B. N. G. Giepmans, Immunolabeling artifacts and the need for live-cell imaging. *Nat. Methods* **9**, 152–158 (2012). doi: 10.1038/nmeth.1855; pmid: 22290187
100. D. R. Whelan, T. D. M. Bell, Image artifacts in single molecule localization microscopy: Why optimization of sample preparation protocols matters. *Sci. Rep.* **5**, 7924 (2015). doi: 10.1038/srep07924; pmid: 25603780
101. D. Li *et al*., ADVANCED IMAGING. Extended-resolution structured illumination imaging of endocytic and cytoskeletal dynamics. *Science* **349**, aab3500 (2015). doi: 10.1126/science.aab3500; pmid: 26315442
102. W. R. Legant *et al*., High-density three-dimensional localization microscopy across large volumes. *Nat. Methods* **13**, 359–365 (2016). doi: 10.1038/nmeth.3797; pmid: 26950745
103. K. J. Hayworth *et al*., Ultrastructurally smooth thick partitioning and volume stitching for large-scale connectomics. *Nat. Methods* **12**, 319–322 (2015). doi: 10.1038/nmeth.3292; pmid: 25686390
104. Y.-G. Yoon *et al*., Feasibility of 3D reconstruction of neural morphology using expansion microscopy and barcode-guided agglomeration. *Front. Comput. Neurosci.* **11**, 97 (2017). doi: 10.3389/fncom.2017.00097; pmid: 29114215
105. S. M. Asano *et al*., Expansion microscopy: Protocols for imaging proteins and RNA in cells and tissues. *Curr. Protoc. Cell Biol.* **80**, e56 (2018). doi: 10.1002/cpcb.56; pmid: 30070431
106. T. L. Liu *et al*., Observing the cell in its native state: Imaging subcellular dynamics in multicellular organisms. *Science* **360**, eaaq1392 (2018). doi: 10.1126/science.aaq1392; pmid: 29674564
107. K. Smith *et al*., CIDRE: An illumination-correction method for optical microscopy. *Nat. Methods* **12**, 404–406 (2015). doi: 10.1038/nmeth.3323; pmid: 25775044
108. S. Preibisch, S. Saalfeld, P. Tomancak, Globally optimal stitching of tiled 3D microscopic image acquisitions. *Bioinformatics* **25**, 1463–1465 (2009). doi: 10.1093/bioinformatics/btp184; pmid: 19346324
109. D. Hörl *et al*., BigStitcher: Reconstructing high-resolution image datasets of cleared and expanded samples. *bioRxiv* (2018). doi: 10.1101/343954
110. M. Emmenlauer *et al*., XuvTools: Free, fast and reliable stitching of large 3D datasets. *J. Microsc.* **233**, 42–60 (2009). doi: 10.1111/j.1365-2818.2008.03094.x; pmid: 19196411
111. A. Bria, G. Iannello, TeraStitcher—A tool for fast automatic 3D-stitching of teravoxel-sized microscopy images. *BMC Bioinformatics* **13**, 316 (2012). doi: 10.1186/1471-2105-13-316; pmid: 23181553
112. T. Pietzsch, S. Preibisch, P. Tomancák, S. Saalfeld, ImgLib2—Generic image processing in Java. *Bioinformatics* **28**, 3009–3011 (2012). doi: 10.1093/bioinformatics/bts543; pmid: 22962343
113. J. Schindelin *et al*., Fiji: An open-source platform for biological-image analysis. *Nat. Methods* **9**, 676–682 (2012). doi: 10.1038/nmeth.2019; pmid: 22743772
114. T. Pietzsch, S. Saalfeld, S. Preibisch, P. Tomancak, BigDataViewer: Visualization and processing for large image data sets. *Nat. Methods* **12**, 481–483 (2015). doi: 10.1038/nmeth.3392; pmid: 26020499

ACKNOWLEDGMENTS

We thank D. Bock, K. Svoboda, N. Ji, N. Spruston, L. Scheffer, E. Snapp, P. Tillberg, L. Lavis, E. Bloss, W. Legant, D. Hoffman, and K. Hayworth at Howard Hughes Medical Institute (HHMI) Janelia Research Campus (JRC) and B. Sabatini and D. Van Vactor at Harvard Medical School (HMS) for invaluable discussions and comments. We also thank K. Schaefer, T. Wolff, C.-L. Chang, and H. Choi at JRC for help with sample preparation and imaging. We gratefully acknowledge the shared resources and project teams at JRC, including D. Alcor, J. Heddleston, and A. Taylor of the Advanced Imaging Center and Light Microscopy Facility for help with imaging; I. Negrashov and jET for manufacturing expertise; and O. Malkesman, K. Salvesen, C. Christoforou, G. Meissner, and the FlyLight project team for sample handling and preparation. Last, we are grateful to C. Pama and R. Karadottir at the University of Cambridge; J. Melander and H. Zhong at OHSU; T. Herman at the University of Oregon; and E. Karagiannis, J.-S. Kang, and F. Chen at MIT for help with sample preparation and H. Otsuna, T. Kawase, and E. Bas at JRC; C. Wietholt at FEI Amira; M. Gastinger at Bitplane; and J. McMullen and T. Tetreault at MBF Bioscience for data analysis and visualization. **Funding**: I.P., D.E.M., T.-L.L., V.S., A.G., J.B., J.C., C.M.O., J.L.-S., A.H., G.M.R., S.S., Y.A., and E.B. are funded by HHMI. E.S.B. acknowledges, for funding, John Doerr, the Open Philanthropy Project, NIH 1R01NS087950, NIH 1RM1HG008525, NIH 1R01DA045549, NIH 2R01DA029639, NIH 1R01NS102727, NIH 1R41MH112318, NIH 1R01EB024261, NIH 1R01MH110932, the HHMI–Simons Faculty Scholars Program, IARPA D16PC00008, U.S. Army Research Laboratory and the U. S. Army Research Office under contract/grant W911NF1510548, U.S.–Israel Binational Science Foundation Grant 2014509, and NIH Director's Pioneer Award 1DP1NS087724. S.U. and T.K. are funded by grants from Biogen, Ionis Pharmaceuticals, and NIH grant R01GM075252 (to T.K.). S.U. gratefully acknowledges the Fellows program of the Image and Data Analysis Core at Harvard Medical School and the MATLAB code repository received from the Computational Image Analysis Workshop, supported by NIH grant GM103792. K.R.M. and S.G.M. are funded by NIH grant R01DC015478. S.T. and A.R. are funded by NIH grant R44MH093011. **Author contributions:** E.B., E.S.B., and R.G. supervised the project and wrote the manuscript with input from all coauthors. T.-L.L. and J.C. built the microscopes with input from E.B., D.E.M., and jET (JRC) and performed all microscope characterization experiments. D.E.M. created the instrument control software. R.G., S.M.A., T.-L.L., V.S., J.C., and C.M.O. acquired all biological data with coauthors. G.H.H. provided the Thy1-YFP mice, and R.G. and S.M.A. prepared the ExM samples. A.G. and A.H. provided the Slc17a7-cre X TCGO mice and prepared the ExM samples. Y.Z. provided the human kidney sections and prepared the ExPath samples. Y.A. and G.M.R. created the split-GAL4 fly strains, Y.A. optimized the IHC conditions, and R.G. and S.M.A prepared the ExM samples. K.R.M., S.G.M., S.M.A., and T.-L.L. provided the initial stitching software packages. I.P. and S.S. created the automated flat-field, stitching, and N5 visualization pipeline, and I.P., R.G., J.B., and S.S. deconvolved, flat-fielded, and stitched all image data. Y.A. performed segmentation and tracing and supervised analyses of all fly image data. C.Z., S.T., and A.R. provided customized commercial software packages and helped with segmentation, tracing and reconstruction of neurites and dendritic spines using these packages. S.-H.S. and H.A.P. designed experimental protocols and performed sample preparation for FIB-SEM. S.P., C.S.X., and H.H. performed FIB-SEM sample preparation, image acquisition, and data processing. J.L.-S. and T.K. provided essential discussion on the subcellular ultrastructure analysis and access to instrumentation and computational resources. S.U. and R.G. processed and performed quantitative analysis of all image data. S.U., R.G., E.B., and Y.A. produced all figures and

Downloaded from http://science.sciencemag.org/ on January 17, 2019

movies. **Competing interests:** Portions of the technology described here are covered by U.S. patent 7,894,136 issued to E.B., assigned to Lattice Light of Ashburn, VA, and licensed to Carl Zeiss Microscopy; U.S. patents 8,711,211 and 9,477,074 issued to E.B., assigned to HHMI, and licensed to Carl Zeiss Microscopy; U.S. patent application 13/844,405 filed by E.B. and assigned to HHMI; and U.S. patent 9,500,846 issued to E.B. and assigned to HHMI. E.S.B. is a co-inventor on multiple patents related to ExM and is also a cofounder of a company that aims to provide kits and services relating to ExM to the public. R.G. is a co-inventor on multiple patents related to ExM. Y.Z. is a co-inventor on multiple patents related to ExM. **Data and materials availability:** All data needed to evaluate the conclusions in the paper are present in the paper or the supplementary materials. The compressed size of the datasets used in generating the figures and movies exceeds 100 terabytes, and it is therefore not practical to upload to a public data repository. All data used in this paper will be made freely available to those who request and provide a mechanism for feasible data transfers (such as physical hard disk drives or cloud storage). Documentation for construction of a LLSM can be obtained by execution of a research license agreement with HHMI.

SUPPLEMENTARY MATERIALS

www.sciencemag.org/content/363/6424/eaau8302/suppl/DC1
Supplementary Text
Figs. S1 to S33
Table S1 to S6
References (*115*–*133*)
Movies S1 to S7

19 July 2018; accepted 30 November 2018
10.1126/science.aau8302

Downloaded from http://science.sciencemag.org/ on January 17, 2019

Science

Cortical column and whole-brain imaging with molecular contrast and nanoscale resolution

Ruixuan Gao, Shoh M. Asano, Srigokul Upadhyayula, Igor Pisarev, Daniel E. Milkie, Tsung-Li Liu, Ved Singh, Austin Graves, Grace H. Huynh, Yongxin Zhao, John Bogovic, Jennifer Colonell, Carolyn M. Ott, Christopher Zugates, Susan Tappan, Alfredo Rodriguez, Kishore R. Mosaliganti, Shu-Hsien Sheu, H. Amalia Pasolli, Song Pang, C. Shan Xu, Sean G. Megason, Harald Hess, Jennifer Lippincott-Schwartz, Adam Hantman, Gerald M. Rubin, Tom Kirchhausen, Stephan Saalfeld, Yoshinori Aso, Edward S. Boyden and Eric Betzig

Science **363** (6424), eaau8302.
DOI: 10.1126/science.aau8302

Combining expansion and the lattice light sheet

Optical and electron microscopy have made tremendous inroads into understanding the complexity of the brain. Gao *et al.* introduce an approach for high-resolution tracing of neurons, their subassemblies, and their molecular constituents over large volumes. They applied their method, which combines expansion microscopy and lattice light-sheet microscopy, to the mouse cortical column and the entire *Drosophila* brain. The approach can be performed at speeds that should enable high-throughput comparative studies of neural development, circuit stereotypy, and structural correlations to neural activity or behavior.

Science, this issue p. eaau8302

ARTICLE TOOLS http://science.sciencemag.org/content/363/6424/eaau8302

SUPPLEMENTARY MATERIALS http://science.sciencemag.org/content/suppl/2019/01/16/363.6424.eaau8302.DC1

REFERENCES This article cites 129 articles, 33 of which you can access for free
http://science.sciencemag.org/content/363/6424/eaau8302#BIBL

PERMISSIONS http://www.sciencemag.org/help/reprints-and-permissions

Use of this article is subject to the Terms of Service

Science (print ISSN 0036-8075; online ISSN 1095-9203) is published by the American Association for the Advancement of Science, 1200 New York Avenue NW, Washington, DC 20005. 2017 © The Authors, some rights reserved; exclusive licensee American Association for the Advancement of Science. No claim to original U.S. Government Works. The title *Science* is a registered trademark of AAAS.

Downloaded from http://science.sciencemag.org/ on January 17, 2019

www.sciencemag.org/content/363/6424/eaau8302/suppl/DC1

Supplementary Material for

Cortical column and whole-brain imaging with molecular contrast and nanoscale resolution

Ruixuan Gao, Shoh M. Asano, Srigokul Upadhyayula, Igor Pisarev, Daniel E. Milkie, Tsung-Li Liu, Ved Singh, Austin Graves, Grace H. Huynh, Yongxin Zhao, John Bogovic, Jennifer Colonell, Carolyn M. Ott, Christopher Zugates, Susan Tappan, Alfredo Rodriguez, Kishore R. Mosaliganti, Shu-Hsien Sheu, H. Amalia Pasolli, Song Pang, C. Shan Xu, Sean G. Megason, Harald Hess, Jennifer Lippincott-Schwartz, Adam Hantman, Gerald M. Rubin, Tom Kirchhausen, Stephan Saalfeld, Yoshinori Aso, Edward S. Boyden*, Eric Betzig*

*Corresponding author. Email: esb@media.mit.edu (E.S.B.); betzige@janelia.hhmi.org (E.B.)

Published 18 January 2019, *Science* **363**, eaau8302 (2017)
DOI: 10.1126/science.aau8302

This PDF file includes:

Supplementary Text
Figs. S1 to S33
Table S1 to S6
References

Other Supplementary Material for this manuscript includes the following:
(available at www.sciencemag.org/content/363/6424/eaau8302/suppl/DC1)

Movies S1 to S7

Table of Contents

Supplementary Notes 5

1. Sample Preparation 5

   a. Ethics statements 5

   b. Mouse 5

   c. Drosophila melanogaster 7

   d. Human 7

   e. Expansion microscopy (ExM) protocols 8

2. Instrumentation for Imaging 10

   a. Lattice light-sheet microscope (LLSM): hardware 10

   b. LLSM: software control 10

   c. LLSM: ExM sample mounting 12

   d. LLSM: perfusion 13

   e. Spinning-disk confocal microscope 13

   f. Airyscan 13

   g. Laser-scanning confocal microscope 13

   h. Focused ion beam milling scanning electron microscopy 14

3. Image Preprocessing 14

   a. Flat-field correction 14

   b. Deconvolution 15

c. Stitching 15

d. Export and interactive visualization 16

e. Default parameters for flat-field correction, stitching, and export 16

f. 3D volume deskew and rotation 17

g. Filtering non-specific antibody signals 17

h. Chromatic and alignment offset correction 18

4. Image Analysis 18

a. Bleaching analysis 18

b. FFT of diffraction-limited fluorescence puncta 19

c. Linear unmixing 19

d. Cellular and subcellular organelles segmentation 19

e. G-Ratio calculation 20

f. Dendritic spine reconstruction 21

g. Dendritic spine - Homer1 puncta association 22

h. Tracing of neurites 23

i. Local maxima detection 23

j. Surface area and volume calculations 24

5. Visualization 24

6. Additional Notes for ExLLSM Datasets 25

a. Segmentation and reconstruction of organelles (Fig. 2, A to E, and fig. S8) 25

b. Podocyte morphology of renal glomerulus (fig. S32) 25

c. Nc82 puncta as the presynaptic site label (fig. S23) 26

d. Association of nc82 puncta to neurons (figs. S24, S25, and S27) 26

e. Nc82 puncta statistics in MB α3 using ExLLSM and FIB-SEM (figs. S22, S25, and S26) 27

f. Cell type classification of the eight PPM3 cluster neurons in the adult Drosophila brain and comparison with individual labeled neurons using multicolor flip-out (MCFO) and split-GAL4 strains (figs. S20 and S21) 27

Supplementary Figures 29

Supplementary Table 62

Captions for Supplementary Movies 75

References and Notes: 82

Supplementary Notes

1. Sample Preparation

a. Ethics statements

All procedures involving Thy1-YFP mice were in accordance with the US National Institutes of Health Guide for the Care and Use of Laboratory Animals and approved by the Massachusetts Institute of Technology Committee on Animal Care.

All animal surgeries and procedures involving Slc17a7-cre X TCGO and C57BL/6 mice were performed humanely, in accordance with protocols (#13-99 and #16-142) approved by the Institutional Animal Care and Use Committee of the Janelia Research Campus, HHMI.

The human kidney specimens (US BioMAX, HuFTS301) were commercially available and unidentified archival specimens that did not require informed consent from the subjects.

b. Mouse

b.1 Thy1-YFP mouse

Transgenic mice expressing cytosolic YFP under the Thy1 promoter (Thy1-YFP-H strain on C57BL/6), 2-4 months old, both male and female, were used. The mice were anesthetized with ketamine/xylazine and perfused transcardially with 25 mL ice cold 4% paraformaldehyde (PFA) in 1x PBS, followed by 25 mL of 1x PBS. Brains were dissected out and soaked for 24 hours in 4% PFA at 4°C. 50-250 μm coronal slices were prepared on a vibratome (Leica VT1000S) and stored in 1x PBS at 4°C.

Unless otherwise noted, immunohistochemistry of Thy1-YFP mouse brain slices was carried out following standard protocols as described previously (*19*, *105*). The antibodies used in this study are listed in table S2. Briefly, the fixed brain slices were permeabilized by 0.1% Triton X-100 in 1x PBS at room temperature for 15 minutes and blocked by a blocking buffer containing 5% normal donkey serum in 1x PBS with 0.1% Triton X-100 at room temperature overnight. The brain slices were incubated with primary antibodies at a dilution of 1:100 -1:200 in the blocking buffer on a shaker at room temperature for 24 hours before the antibody solution was washed out 4 x 30 minutes with fresh blocking buffer. The brain slices were then incubated with secondary

antibodies at a dilution of 1:100 - 1:200 in the blocking buffer on a shaker at room temperature for 24 hours before the antibody solution was washed out 4 x 30 minutes with fresh 1x PBS for the subsequent expansion microscopy (ExM) protocols. For the sequential Tom20 and LAMP1 staining, Thy1-YFP brain slices were first permeabilized, blocked, and incubated in the primary antibody against Tom20 and the secondary antibody as described. The brain slices were subsequently blocked in a blocking buffer of 5% normal goat serum in 1x PBS with 0.1% Triton X-100 at room temperature overnight and incubated in the primary antibody against LAMP1 and the secondary antibody.

b.2 Slc17a7-cre X TCGO mouse

Cre-dependent adeno-associated viruses (AAV) for rabies glycoprotein G (G) and avian tumor virus receptor A (TVA) were stereotactically injected into basal pontine nucleus (BPN) of Slc17a7-cre X TCGO mice at 3.9 mm posterior to bregma, 0.5 mm lateral of midline, at depths of 5.9, 5.7, and 5.5 mm below dura (100 nL/depth). Selective, retrograde labeling of BPN mossy fiber projections to the paramedian lobule of cerebellum was achieved by injecting a pseudotyped G-deleted rabies virus (SAD mCherry EnvA) whose tropism is restricted to TVA (*115*) to the paramedian lobule 7.25 mm posterior to bregma, 2.25 mm lateral of midline, at depths of 1.9, 1.7, and 1.5 mm below dura (70 nL/depth). G and TVA AAV injection preceded rabies injection by 2-3 weeks. With this approach, only G/TVA-coexpressing terminals originating from BPN could also retrogradely express pseudotyped mCherry rabies. A sparse subset of cerebellar Granule cells and Golgi cells that received inputs from BPN mossy fibers were anterogradely infected with mCherry rabies.

After 2-3 weeks of AAV expression and an additional 10 days of rabies expression, animals were anesthetized, transcardially perfused with 4% PFA in 1x PBS. The brains were dissected and post-fixed in PFA for 2 hours. 100 µm coronal slices of the entire brain were made using a vibratome (Leica VT1200S) and tissues from the cerebellum were prepared for the subsequent ExM protocols.

b.3 C57BL/6 mouse

A 2-month old male C57BL/6 mouse was deeply anesthetized and transcardially perfused with 30 ml of 3% PFA (60 mM NaCl, 130 mM glycerol, 10 mM sodium phosphate buffer). The brain was carefully dissected out from the skull and post-fixed with 50 ml of 3% PFA (30 mM of NaCl, 70 mM glycerol, 30 mM PIPES buffer, 10 mM betaine, 2 mM $CaCl_2$, 2 mM $MgSO_4$) for 2 hours

at room temperature. The brain sample was then rinsed in a 400 mOsM buffer (65 mM NaCl, 100 mM glycerol, 30 mM PIPES buffer, 10 mM betaine, 2 mM $CaCl_2$, and 2 mM $MgSO_4$) for half an hour, followed by vibratome sectioning (coronal sections, 100 μm thickness) using a Leica VT1000S vibratome in the same buffer. 100 μm sections were then fixed in 1% PFA, 2% glutaraldehyde solution (30 mM NaCl, 70 mM glycerol, 30 mM PIPES buffer, 10 mM betaine, 2 mM $CaCl_2$, 2 mM $MgSO_4$, 75 mM sucrose) overnight at 4°C. Sections were then washed using the 400 mOsM rinsing buffer (see above). Round samples of the hippocampus were created from the 100 μm coronal sections using a 2 mm biopsy punch (Miltex, Inc). The 2 mm samples were dipped in hexadecene, placed in a 100 μm aluminum carrier, covered with a flat carrier and high-pressure frozen using a Wohlwend compact 01 High pressure freezer. Samples were then freeze-substituted in 0.5% osmium tetroxide, 20 mM 3-Amino-1,2,4-triazole, 0.1% uranyl acetate, 4% water in acetone, using a Leica AFS2 system. Specimens were further dehydrated in 100% acetone and embedded in Durcupan resin.

c. Drosophila melanogaster

The fly strains and antibodies used in this study are listed in table S2. Briefly, split-GAL4 drivers were designed and made based on confocal image database (*9*, *86*, *90*, *116*, *117*). Crosses were kept on standard cornmeal food at 21°C at 60% relative humidity. Dissection and immunohistochemistry of fly brains were done as previously described with minor modifications (*9*, *17*). Brains of 3-10 days old adult female flies were dissected in Schneider's Insect medium and fixed in 4% PFA in Schneider's medium for 55 min at room temperature. After washing in PBT (0.5% Triton X-100 in 1x PBS) for 3 x 10 min, the tissues were blocked in 5% normal goat serum (or normal donkey serum, depending on the secondary antibody) for 90 min. Subsequently, the tissues were incubated in primary antibodies diluted in 5% serum in PBT for 2-4 days on a nutating shaker at 4°C, washed in PBT for 3 x 30 min or longer, then incubated in secondary antibodies diluted in 5% serum in PBT for 2-4 days on a nutating shaker at 4°C. The tissues were washed thoroughly in PBT 4 x 30 min or longer before starting the ExM protocols. For the samples with V5 labeling, tissues were post-fixed with 4% PFA for 2 hours at room temperature after secondary antibodies, washed three times in PBT, blocked with 5% normal mouse serum in PBT for 1.5 hours and then incubated in V5 antibody directly conjugated with dye overnight.

d. Human

Acetone-fixed frost kidney specimens (US BioMAX, HuFTS301) were immunostained using the expansion pathology (ExPath) protocol as described previously (*98*). Briefly, the kidney

specimen was placed in 20 mM sodium citrate solution (pH 8) at ~100°C in a heat-resistant container, and the container was immediately transferred to a 60°C incubator for 30 min. Then the specimen was immunostained with primary antibodies in MAXbind™ Staining Medium (Active Motif) at a concentration of 10 µg/mL at room temperature for 3 hours, followed by staining with secondary antibodies (table S2). Finally, the specimens were washed 2-3 times with MAXwash™ Washing Medium before the expansion part of the ExPath protocol.

e. Expansion microscopy (ExM) protocols

e.1 Basic protocol

Unless otherwise noted, all samples were prepared using the protein-retention ExM (proExM) protocol with minor modifications (*19*, *105*). Briefly, acryloyl-X, SE (6-((acryloyl)amino)hexanoic acid, succinimidyl ester or AcX, Thermo-Fisher) stock solution was mixed at a concentration of 10 mg/mL in anhydrous DMSO and stored at -20°C in a desiccated environment. Fixed and immunostained samples were incubated in diluted AcX solution (0.1 mg/mL in 1x PBS) at room temperature overnight. Monomer solution (1x PBS, 2 M NaCl, 8.625% (w/v) sodium acrylate, 2.5% (w/v) acrylamide, 0.15% (w/v) N,N′-methylenebisacrylamide) was mixed and cooled to 4°C before use. Concentrated stocks of ammonium persulfate (APS) (10% w/v), tetramethylethylenediamine (TEMED) (10% w/v), and 4-hydroxy-2,2,6,6-tetramethylpiperidin-1-oxyl (4HT) (0.5% w/v) were added to the monomer solution to a final concentration of 0.2% (w/v), 0.2% (w/v), and 0.01% (w/v), respectively, to yield the gelling solution. The samples in AcX solution were washed 2 x 15 min with 1x PBS and immediately incubated in the mixed gelling solution at 4°C for 30 min, transferred to a gelation chamber, and gelled in a humidified 37°C incubator for 2 hours. The gelled samples were trimmed and immersed in digestion buffer (50 mM Tris (pH 8), 1 mM EDTA, 0.5% Triton X-100, 1 M NaCl, 8 units/mL Proteinase K (New England Biolabs)) at room temperature overnight. The digested samples were expanded in doubly deionized water or 1 mM NaOH aqueous solution for 3 x 20 min immediately before the sample mounting and imaging.

High expansion samples (expansion factor: ~7x) were prepared using an iterative expansion of N,N-dimethylacetoacetamide (DMAA) gel, and then the polyacrylamide/sodium polyacrylate gel as described (*29*, *118*). Briefly, fixed and immunostained samples were incubated in diluted AcX solution (0.1 mg/mL in 1x PBS) at room temperature overnight. Monomer solution (1x PBS, 20% (w/v) DMAA, 0.01% (w/v) N,N′-methylenebisacrylamide) was mixed and cooled to 4°C before use. Concentrated stocks of potassium persulfate (KPS) (4.2% w/v), TEMED (10% w/v), and 4HT

(0.5% w/v) were added to the monomer solution to a final concentration of 0.168 % (w/v), 0.2% (w/v), and 0.01% (w/v), respectively, to yield the gelling solution. The samples in AcX solution were washed 2 x 5 min with 1x PBS and immediately incubated in the mixed gelling solution at 4°C for 2 hours in a gelation chamber, and gelled in a humidified 37°C incubator for 2 hours. During the gelation process, small air bubbles trapped in the gelation chamber were removed to prevent residual oxygen. The gelled samples were trimmed, immersed in the digestion buffer at room temperature overnight as described, and washed 3 x 20 min with 1x PBS. The samples were subsequently reembedded in polyacrylamide/sodium polyacrylate gel following the proExM protocol as described, and expanded in doubly deionized water for 3 x 20 min immediately before the sample mounting and imaging.

Unless otherwise noted, overview fluorescence images of all samples were captured with a wide-field or spinning-disk confocal microscope at pre-gelation and post-expansion states. Distinctive landmarks in pre-gelation and post-expansion images were used to calculate the expansion factors.

e.2 Thick mouse brain slices (>100 μm)

Thick mouse brain slice (100 - 250 μm) ExM samples were prepared using a modified proExM protocol as described previously (*19*, *105*). Briefly, fixed and immunostained brain slices were incubated in diluted AcX solution (0.1 mg/mL) in MES buffered saline (100 mM MES + 150 mM NaCl, pH ~6) at room temperature for 24 hours. The gelling solution was prepared with 1.5 times more 4HT (0.015% w/v) and the samples were incubated in the gelling solution at 4°C for 45-60 min before gelation. Digestion of the samples was carried out in the digestion buffer at room temperature for 24 hours and then in fresh digestion buffer for another 24 hours.

e.3 Drosophila melanogaster

Fly brain ExM samples were prepared using a modified proExM protocol as described previously (*19*, *105*). Fixed and immunostained fly brains were incubated in diluted AcX solution (0.1 mg/mL in 1x PBS) at room temperature for 24 hours. The gelling solution was prepared with 1.5 times more 4HT (0.015% w/v) and the samples were incubated in the gelling solution at 4°C for 1 hour before gelation. Digestion of the samples was carried out in the digestion buffer at room temperature for 24 hours and then in fresh digestion buffer for another 24 hours.

e.4 Human

Human kidney sample was prepared and expanded using the ExPath protocol as described previously (*98*).

2. Instrumentation for Imaging

a. Lattice light-sheet microscope (LLSM): hardware

Imaging of all expanded ExM samples except that in the left column of Fig. 1 was carried out in objective scan mode (*20*) (where the detection objective and the light-sheet moved together in discrete steps) using a LLSM described previously (*106*), except with its adaptive optics capabilities disabled. The ExM sample at the left in Fig. 1 was imaged using an LLSM optimized for expanded samples in order to increase the field of view and allow for long-range fast scanning in the sample scan mode (where the sample was translated continuously in the plane of the coverslip). It used two pairs of cylindrical lenses to illuminate a thin stripe on a spatial light modulator (Forth Dimension QXGA with 2048 by 1536 pixels) in order to generate a lattice light-sheet ~160 μm wide along the *y*-axis. The sample was scanned in the *x*-direction (sample scan mode) using a piezo inertia stage (PI Q522.130) that allows scanning of 1.5 mm. The width and depth of the sample bath was increased to facilitate for the tiling of samples over a larger range (up to ± 6 mm). A two camera solution was implemented along with dichroics and emission filters (Semrock Di03-R561-t1-25x36; emission filter on the camera 1 is a Semrock FF01-530/43-25; emission filter on the camera 2 was a Semrock LP02-568RU-25), which, in the fast multicolor acquisition mode, allowed readout of one camera during exposure of the other.

b. LLSM: software control

For samples with rectangular imaging volumes, we typically specified a rectangular parallelepiped as hard limits for the tiled volume. The microscope software covered the volume with a 3D matrix of rectangular tiles with the desired tile overlap. For smaller data sets, the tile overlap was set at 4 μm in *x/y* and 8 μm in *z*. For larger data sets more affected by sample shrinkage over time or position errors near the limits of stage travel, the overlap was increased to, for example, 6 μm in *x/y* and 12 μm in *z*.

For large samples with non-rectangular extents, we chose to implement a strategy to avoid imaging tiles that had no signals. Termed “intelligent tiling”, the software automatically determined tiles that had signals, and then progressively imaged the neighboring tiles, stopping when there were no signals. We found it was most efficient to image a volume by minimizing the

stage motion, especially the *z* stage motion. Therefore, all of the tiles at a single *z* stage position (i.e. the tiles in the same *z* slab) were imaged following a serpentine pattern before moving to the next *z* slab.

In detail, we first specified a rectangular parallelepiped as hard limits for the tiled volume and the microscope software covered the volume with a 3D matrix of rectangular tiles with the desired tile overlap as described. These tiles became the "candidate tile" list. Next, we found a tile of interest and set it as the "seed" tile where the software would begin imaging at. The seed tile initialized the "working on" queue. The microscope then began imaging tiles from the "working on" queue. If an imaged tile had signals, then its bordering six tiles were removed from the "candidate tile" list and placed in a "next batch" list. Whenever the "working on" queue was empty or the *z* position was about to switch, all the tiles in the "next batch" list and "working on" queue were combined and then sorted according to serpentine paths within each *z* slab and added to the "working on" queue. The *z* slabs were sorted from their distance to the seed point.

A tile was determined to have signals based on the set thresholds. Briefly, we set the "pixel intensity threshold" and the "count threshold", as well as which emission channel to be used for the signal checking. During imaging of a tile, the number of pixels above the "pixel intensity threshold" were counted for every camera image with the specified emission channel. If the count was ever greater than the "count threshold", the tile was considered to have signals.

This "intelligent tiling" implementation was typically robust enough to automatically capture the signal of interest and follow the specimen contour. We could also view the data as it was acquiring and direct the imaging along a particular direction by circling areas in a reviewer tool to add tiles (or prevent tiles from being imaged) if needed.

Autofocus was performed on a 200 nm diameter fluorescent bead located on the sample surface every 10-30 minutes for selected samples that required long-term imaging (~days). During each autofocus measurement, the bead was precisely located using a normal imaging volume sweep. The light sheet was statically held at the bead, while the objective piezo was swept. The fluorescence intensity as function of a piezo position was fitted with a Gaussian curve and the peak center gave the correct piezo offset to use.

c. LLSM: ExM sample mounting

Expanded ExM samples were mounted on the LLSM sample holder using the following protocols to ensure mechanical stability during the imaging. Unless otherwise noted, all expanded ExM samples were trimmed and mounted on a cleaned 12 mm coverslip using the "superglue method" or the "poly-L-lysine method" as described previously (*105*). The 12 mm coverslips were cleaned by soaking in 1M KOH in water for 30 minutes, rinsed with double-distilled water three times, stored in 30% (v/v) ethanol in water, and air-dried before the sample mounting.

For the "superglue method", a thin layer of superglue was applied to a small area of the cleaned 12 mm coverslip. Excessive liquid around the expanded ExM sample was wicked away before the sample was placed on the applied superglue. After curing the superglue for 20-30 s, a few droplets of double-distilled water were added to keep the sample hydrated and to wash away uncured superglue. After the curing, an opaque interface was formed between the gel and the superglue. For the "poly-L-lysine method", a few droplets of 0.1% (w/v) poly-L-lysine aqueous solution were applied to the top surface of the cleaned 12 mm coverslip for 20 min. The poly-L-lysine modified surface was rinsed with double-distilled water three times and air-dried for 1 hour in a clean environment. Excessive liquid around the expanded ExM sample was wicked away before the sample was placed on the poly-L-lysine modified surface of the 12 mm coverslip. After 20-30 s, a few droplets of double-distilled water were added to keep the sample hydrated.

After mounting the sample to the 12 mm coverslip, the coverslip was attached to the LLSM sample holder with superglue or metal clips. The sample holder was then transferred to the sample chamber filled with double-distilled water or 1 mM NaOH aqueous solution.

Fluorescent beads were attached to the sample surface for autofocusing for selected samples that required long-term imaging (~days). After sample mounting as described, the sample was soaked in diluted fluorescent bead solution (amine-terminated FluoSpheres, 0.2 μm, red fluorescent (580/605), ThermoFisher) for 5 min, and rinsed with fresh double-distilled water twice before transferring to the sample chamber. The bead solution was diluted in double-distilled water by a factor of ~10^5-10^6 and ultrasonicated for 10 min before use.

Selected Thy1-YFP mouse brain slice samples were expanded and mounted in 1 mM NaOH aqueous solution to prevent the slow denaturing of YFP in water (table S2).

d. LLSM: perfusion

Selected samples that required long-term imaging (~days) were perfused with fresh double distilled water or 1 mM NaOH aqueous solution to maintain a stable pH in the sample chamber.

e. Spinning-disk confocal microscope

An Andor spinning-disk (CSU-W1 Yokogawa) confocal system on a Nikon Eclipse Ti-E microscope body was used to acquire tiled *z* stacks of expanded Thy-1 YFP mouse sample in Fig. 1A. 2 by 2 tiled images with 15 % overlap were collected using a Nikon CFI Apo LambdaS LWD 40x (1.15 NA) water-immersion objective. The sample was imaged using 488 nm and 561 nm solid state laser lines and Andor Zyla 4.2 PLUS sCMOS camera. The 3D image tiles were deconvolved using experimentally measured PSFs for each color channel for 15 iterations (*20*).

f. Airyscan

A Zeiss LSM 880 laser-scanning confocal microscope with the Airyscan module was used in Fast mode to acquire tiled *z* stacks of expanded Thy-1 YFP mouse sample in Fig. 1. In this mode, an elliptical laser beam entered the objective, and a column of 4 pixels (in the *y*-direction) were acquired simultaneously. 3 by 3 tiled images with 10% overlap were collected using a Zeiss C-Apochromat 40x (1.1 NA) water immersion objective with a 2x zoom. The samples were imaged using 488 nm and 561 nm laser lines with a pixel dwell time of 0.54 µs. The 3D image tiles were Airyscan-processed using ZEN (Zeiss).

A Zeiss LSM 880 laser-scanning confocal microscope with the Airyscan module was used in standard mode to acquire a tiled *z* stack of the non-expanded PPM3 dopaminergic neurons (DANs) in movie S4. The fly brain was cleared and mounted in DPX after immunostaining. A 1 by 1 tiled image was collected using a Zeiss (Plan-Apochromat 63x, 1.4 NA Oil DIC M27) oil immersion objective with a 2.5x zoom, 1268- by 1268-pixel (0.04- by 0.04-µm) field of view, and 190 nm z-step. The samples were imaged using the 488 nm laser line with a pixel dwell time of 1.09 µs. The 3D image tile was Airyscan-processed using ZEN (Zeiss).

g. Laser-scanning confocal microscope

A Zeiss LSM 800 laser-scanning confocal microscope was used to acquire *z* stacks of pre-expansion and post-expansion fly brains in fig. S1. The image stacks were collected using a Zeiss Plan-Apochromat 20x (0.8 NA) air objective.

h. Focused ion beam milling scanning electron microscopy

A Durcupan embedded mouse hippocampus CA1 sample (fig. S11) was first mounted on a Cu stud, then imaged by a customized Zeiss NVision40 FIB-SEM system previously described (*4*). The sample was biased at 400 V to improve image contrast by filtering out secondary electrons. The block face was imaged by a 1 nA electron beam with 1.5 keV landing energy at 1.25 MHz. The *xy* pixel resolution was set at 8 nm. A subsequently applied focused Ga+ beam of 27 nA at 30 keV strafed across the top surface and ablated away 2 nm of the surface. The newly exposed surface was then imaged again. The ablation–imaging cycle continued about once every minute for one week. The sequence of acquired images formed a raw imaged volume, followed by post processing of image registration and alignment using a Scale Invariant Feature Transform (SIFT) based algorithm. The aligned stack was binned by a factor of 4 along z to form a final isotropic volume of 40 by 40 by 40 μm with 8- by 8- by 8-nm voxels, which can be viewed in arbitrary orientations.

3. Image Preprocessing

Existing stitching and flat-field correction tools do not scale to datasets with thousands of 3D image tiles and lack automatic tools for error detection (*107–111*). Hence, we developed an image preprocessing pipeline that utilizes Apache Spark 2 based high performance computing (HPC) environments to enable rapid flat-field correction, deconvolution, and stitching of datasets with thousands of 3D image tiles (manuscript in preparation). All developed software packages are available as open-source projects on GitHub (flat-field correction, stitching, and export: https://github.com/saalfeldlab/stitching-spark, visualization tools: https://github.com/saalfeldlab/n5-viewer). All the ExLLSM datasets were preprocessed with the flat-field correction, deconvolution and stitching pipeline, which was executed on HHMI Janelia's computing cluster. In addition, selected ExLLSM datasets were further preprocessed with deskewing/rotation, noise removal, or chromatic offset correction.

a. Flat-field correction

First, we developed a flat-field correction pipeline for large sets of 2D or 3D images based on the state-of-the-art flat-field correction method CIDRE (*107*). The original implementation supports 2D image sets of limited size, requires that all input data (all images) be loaded into main memory at once, and implements an optimization objective that does not enable parallelization.

Our improved solution supports 2D and 3D images at full resolution, has constant memory requirements, and relaxes the optimization objective in a way that enables parallel solution (figs. S5 and S6). For the datasets in table S2, flat-fields were calculated for each dataset and channel independently using HHMI Janelia's computing cluster. Flat-fields were applied to all 3D image tiles prior to deconvolution and stitching.

b. Deconvolution

Unless otherwise noted, all the datasets acquired were deconvolved after flat-field correction on tile-by-tile basis with the Richardson-Lucy algorithm adapted to run on MATLAB, using experimentally measured PSFs for each color channel for 15 iterations (*20*) (fig. S6). The MATLAB code was executed on the HHMI Janelia's computing cluster.

c. Stitching

All datasets were stitched with our HPC stitching pipeline of rigid transformation based on image tile cross-correlations, which incorporated an iteratively refined prediction model for systematic stage coordinate errors (fig. S7). The fully-automated prediction model enabled us to stitch all datasets without manual intervention. Briefly, recorded stage coordinates were rotated into sample space and converted into a JSON format. From these coordinates, overlapping tile pairs were identified. Only tile pairs that overlapped by more than 50% in n-1 dimensions in n-dimensional space (e.g., 2 out of 3) were used as we found this to be more robust than including "diagonal" pairs with small overlap volumes. The overlap volume was padded by a user defined tolerance space (table S2). All channels of each raw tile were flat-field corrected, and channels were averaged into a single gray scale channel to maximize the amount of signal relevant for stitching. Gaussian smoothing was applied to suppress the effect of high frequency noise. Pairwise translation vectors were estimated using the phase correlation method (*108*). All vectors for which the intensity variance in both image tiles and the normalized cross-correlation (NCC) were below a given threshold were not used for global optimization. Thresholds were found by exhaustive iterative grid search over both parameters until the maximum residual of the optimized solution fell below a user defined threshold (e.g., 10 pixels, *c.f.*, table S2). This "trusted" but "small" solution was then used to predict pairwise translation vectors for tile pairs that were previously rejected. For these tile pairs, pairwise translation vectors were estimated using the phase correlation method (*108*), seeded at the predicted translation vector instead of that indicated from imported stage coordinates. The new set of pairwise shift vectors was again filtered, optimized, and used to generate an improved prediction model. This was repeated until no more tiles were

added to the solution. For Sample 12 (table S2), local deformation that occurred over the course of imaging prevented effective stitching except for subsets of tiles acquired close in time. Therefore, we independently stitched sets of tiles with a shared *z*-coordinate to form "slabs," then manually aligned these slabs using BigWarp (*119*, *120*) to account for the deformation.

d. Export and interactive visualization

The stitched volume was exported to a custom file format (N5) that enabled parallel block-wise export and compression as a multichannel multiscale pyramid using a parallel HPC exporter. We provided bindings for this file format for the ImgLib2 library (*112*) that we made available for the ImageJ distribution Fiji (*113*). Instead of linear blending (*108*), regions where multiple tiles overlap were typically rendered with *max-border-distance* fusion, in which the pixel of the tile with the largest distance to the tile border is used. With flat-field corrected tiles, we found this fusion mode visually more appealing than smooth blending. We attributed this to the fact the expanded samples experience minor non-rigid deformations that are not captured by our purely translation based stitching. These deformations lead to reduced sharpness in the overlap region when multiple overlapping tiles are smoothly blended.

Selected volumes of the datasets were subsequently exported into TIFF series and HDF5 for visualization and analysis.

Finally, we developed a Fiji plugin “N5 Viewer” based on BigDataViewer (*114*) for interactive browsing of multichannel multiscale N5 datasets. The plugin automatically saves user adjusted viewer properties such as color scheme, contrast, grouping, and bookmarks to simplify working with datasets and sharing them with colleagues. Arbitrary subvolumes can be extracted and exported for processing in Fiji or other legacy image processing software.

e. Default parameters for flat-field correction, stitching, and export

The default parameters used for flat-field correction, stitching, and export are listed below. Unless otherwise noted, all the ExLLSM datasets were processed using the default parameters. Detailed stitching conditions and results are listed in table S2.

Flat-field correction

- Minimum histogram value: 80
- Maximum histogram value: 500
- Histogram size: 256

- Background value (pivot point): 101
- Regularization towards pivot point: 0.5
- Hierarchical regularization towards correction fields at lower resolution: 0.5

Stitching
- Considering only adjacent pairs with more than 50% overlap in two dimensions
- No padding for the overlapping region (use stage coordinates with ~11% overlap)
- Gaussian blur sigma: 2.0
- Search window for extracting local statistics for excluded tiles: 3x tile size
- Minimum number of points within the search window for considering a tile: 5
- Radius of the confidence ellipse: 3x standard deviation
- Maximum allowed transfer error: 20 pixels

Export
- Output block size: 128 pixels in *x/y*, adjusted in *z* with respect to the pixel resolution
- Fusion mode: max-border-distance

f. 3D volume deskew and rotation

The data collected by sample scan mode were deskewed using inverse shear transform as described previously (*20*, *121*). The deskewed sample-scan data and selected objective scan datasets were corrected for *z*-anisotropy by 3D interpolation and rotated along the *y* axis and into real world coordinates. In order to decrease the overall file sizes and facilitate visualization, the rotated data was anisotropically resampled in *x* and *z* dimensions to match the original Nyquist sampling of the collected data.

g. Filtering non-specific antibody signals

The volume was first smoothed using a 3D Gaussian kernel (sigma values ranged from 0.5 to 1). Next, Otsu's method (*122*) was applied to calculate a clustering-based threshold on the smoothed volume values larger than zero and less than 99th percentile. Based on the size of the dataset larger than 100 Gigabytes, between three to ten subvolumes of 750^3 voxels representing the heterogeneity of the data were cropped from the flat-field corrected, deconvolved and stitched volumes. The average Otsu threshold value calculated from these subvolumes served as a minimum threshold for segmenting the membrane, cytosolic or punctate signals. On large data sets, Otsu's method was applied on each of the subvolumes (750^3 voxels), and the larger value between the previously calculated minimum threshold and the subvolume's Otsu value was used as the final threshold. To facilitate visualization of data comprising of membrane and cytosolic

filled signals, discrete objects with less than 1008 connected voxels (integral of a 3D Gaussian with sigma σ_{xyz} = 4, which corresponds to objects with FWHM ~ 0.9 by 0.9 by 1.7 μm post expansion) were removed. Similarly, for data containing punctate signals, discrete objects with less than 192 (σ_{xyz} = 2.3, corresponding to objects with lateral FWHM ~ 0.5 by 0.5 by 1.0 μm post expansion), 246 (σ_{xyz} = 2.5, corresponding to objects with lateral FWHM ~ 0.6 by 0.6 by 1.1 μm post expansion) and 1008 connected voxels were removed for nc82, Homer1, and Homer1 and Bassoon pairs respectively (fig. S33).

h. Chromatic and alignment offset correction

In multichannel datasets, the combined chromatic and alignment offsets were measured using PSFs generated by exciting and recording the emission of multicolor beads (200 nm TetraSpeck beads, Life technologies, catalog #T7280) on a coverslip with single or dual camera setup. The *z*-offsets were calculated by taking the difference of the 3D-fitted PSF positions (*121*) between the channels and were corrected by displacing the affected channel relative to reference by the offset values rounded to the nearest pixel.

4. Image Analysis

a. Bleaching analysis

To ensure fair comparison between different imaging methodologies, multiple blocks of expanded Thy1-YFP mouse brain sample with Tom20 antibody staining were cut from the primary somatosensory cortex of the same gelled brain slice and were imaged using spinning-disk confocal microscope, Airyscan, and LLSM as described. Each block contained multiple layer V pyramidal neuron somas and was of similar brightness. The imaged volumes in the YFP color channel were first pre-processed to remove non-specific signals as described in supplementary note 3g. Discrete objects larger than 100 μm^3 in each subvolume were excluded from bleaching analysis since they typically contained higher than average signals corresponding to neuronal cell bodies. For each imaging modality, the normalized integrated intensity was plotted for each subvolume as a function of total imaged volume. The normalized integrated intensity plot was smoothed to account for the content heterogeneity using a moving average smooth function in MATLAB with a span half the size of the number of subvolumes.

b. FFT of diffraction-limited fluorescence puncta

Representative image subvolumes of ~25 by 25 by 25 μm (post expansion size ~100 by 100 by 100 μm) in the Tom20 color channel were extracted from the above datasets using Amira (Thermo Fisher Scientific) or N5 Viewer. The subvolumes were selected from near the sample surface facing the imaging objective. The subvolumes were then individually loaded into Amira to calculate the Fourier transform (*FFT, Magnitude logarithm* function). Its maximum intensity projections into the *xy* and *xz* plane (*Image Ortho Projections* function) were subsequently loaded into MATLAB, where all the projections were normalized by the intensity and then adjusted to the same pixel size in the Fourier space.

c. Linear unmixing

Dual-channel LLSM data acquired with a single camera setup introduced signal bleed-through from a neighboring channel. Typically, a fraction of the Alexa Fluor 568 fluorophores was excited by the 488nm laser, and their emission signal contributed to the total recorded signal of YFP emission. The emission signal was unmixed to correct for signal bleed-through, where the acquired image channels were first deconvolved and background corrected. Subsequently, the relative contribution of Alexa Fluor 568 at λ_{ex} 488 nm was calculated by scaling its emission signal from λ_{ex} 560 nm based on the excitation efficiency of the Alexa Fluor 568 at λ_{ex} 488 nm. Finally, the calculated contribution of Alexa Fluor 568 was subtracted from the emission signal collected at 488nm excitation.

d. Cellular and subcellular organelles segmentation

The 3D volumes were cropped to include either neuronal somas, dendrites or axons. These cropped volumes were segmented using Otsu's method to threshold and filter discrete objects with less than 200 connected voxels. The resulting volume segmented the cells based on the cytosolic YFP filled signal. The sub-cellular membrane based organelle compartments excluded the YFP signals and thus generated a neuronal body mask-with-holes. A closed-mask was generated by filling these holes using the MATLAB function *imfill* by looping over the three dimensions separately. Subtracting the mask-with-holes from the closed-mask generated a sub-cellular organelle compartments mask. The segmented sub-cellular objects whose voxels were within 5 voxels to the lateral edge or 2 voxels to the axial edge of the volume were excluded for further analysis or visualization.

Subcellular compartments were identified either as mitochondria or lysosomes based on the antibody stained channels specific for Tom20 or LAMP1. The antibody signals typically appeared as punctate structures decorating the compartments. To assign compartments as positive or negative for either mitochondria or lysosomes, the antibody signal within each sub-cellular compartment was integrated and normalized for its volume and Otsu's method was applied on the distribution to determine a cutoff. The sub-cellular compartments with a normalized antibody signal higher than or equal to the cutoff were assigned as positive for Tom20 were scored as mitochondria first, followed by LAMP1 for lysosomes.

Surface area and volume calculations of the subcellular compartments are described in supplementary note 4j. Major and minor axis length were calculated using MATLAB *regionprops3* available from MathWorks File Exchange (https://www.mathworks.com/matlabcentral/fileexchange/47578-regionprops3) on 3D interpolated volumes to account for the *z*-anisotropy. Aspect ratio of each sub-cellular compartment was calculated by dividing the major axis by the minor axis.

e. G-Ratio calculation

Subvolumes containing myelinated axons were first cropped, then pre-processed to remove non-specific signals, and segmented. In the case of myelin segmentation, the output was a hollow tube that was subsequently filled. The segmentation outputs were curated in ITK-SNAP (*123*). The local G-Ratio and myelin thickness were calculated using the following pipeline: (1) filled axon structure was skeletonized to calculate its medial backbone, (2) *z*-anisotropy corrected distance transform mapping away from the axon's medial backbone was calculated, (3) perimeter of the filled axon and myelin volume was calculated using *bwperim* MATALB function, (4) the distance transform map values at the perimeter coordinates generated a local radius map from the axon's medial axis for both myelin and axon, (5) at every point along the myelin perimeter, the closest axon perimeter position was calculated via *K*d-tree nearest neighbor searcher using *KDTreeSearcher* and *knnsearch* MATLAB functions, (6) a local G-Ratio was calculated by dividing the local radius of the closest axon position by the local radius of myelin at every point along the perimeter of the myelin, (7) similarly, the local distance between the outer surface of the myelin sheath and the axon was calculated by subtracting the local radius of the closest axon position from the local radius of myelin at every point along the perimeter of the myelin.

f. Dendritic spine reconstruction

To fully capture the morphological details offered by the quality and resolution of our images, we used a Rayburst-algorithm-based approach for 3D reconstruction (*124*, *125*) and revised the structural metrics for the spine reconstruction and analysis to better represent the length and diameter of the spine necks.

Seven image volumes of 3000 by 6000 by 3000 voxels (pre-expansion size: ~80 by 160 by 150 µm, post-expansion size: ~290 by 580 by 540 µm) were cropped from different cortical regions of the mouse primary somatosensory cortex dataset as shown in Positions 1-7 of Fig. 3A. Using Stereo Investigator (version 2017.02.1, MBF Bioscience, Williston, VT), the cropped image volume at each position was systematically and randomly sampled to generate 4 subvolumes for dendritic spine reconstruction per position. Briefly, the cropped image volume was loaded, and the image *xy* boundaries were traced, and a grid with dimensions 200 by 140 pixels was thrown using the Fractionator probe. The randomized starting *z* position within the image volume was selected after confirming the entire volume was visible from that position. At each systematically random location, the image volume was cropped to create a subvolume of 1000 by 1000 by 278 voxels (pre-expansion size: ~27 by 27 by 14 µm, post-expansion size: ~100 by 100 by 50 µm). In total, 28 image subvolumes were reconstructed from the 7 positions.

In Neurolucida 360 (ver. 2017.01.2, MBF Bioscience, Williston, VT), the image subvolumes were pre-processed using a 2D Grayscale Morphological Closing filter which served to fill the labeled dendritic structures more uniformly for reconstruction. A structuring element radius of 10 pixels was used. All dendrites containing dendritic spines were fully reconstructed in 3D using the voxel scooping algorithm in semi-automatic mode. Further manual editing was used when necessary to refine the dendritic diameters to obtain ground truth reconstruction. Dendritic spines were modeled in Neurolucida 360 using the following parameters. Only dendritic spines entirely contained within the image subvolume were reconstructed.

Outer extent: 15 µm

- Minimum height: 0.3 µm
- Detector sensitivity range: 80-130
- Minimum count: 4
- Image noise filter and axial smear correction was enabled

All reconstructions were performed on the expanded image volumes with the voxel size of 0.097 by 0.097 by 0.18 µm. Expansion factor correction was applied post-hoc to obtain

reconstructions representing the biologically relevant pre-expansion size (expansion factor: 3.62x). Comparisons between expanded and corrected image volumes were therefore possible. Spine classification was applied to dendritic spines within the corrected data volumes, using the default classification parameters (*125*). Neurolucida 360 by default uses the spine backbone length instead of the max distance to surface used in the published algorithm. This, coupled with the increased resolution afforded by ExLLSM, results in a more accurate classification of longer spines, irrespective of their angle in relation their dendrite. Furthermore, the current classifier includes an additional parameter used to distinguish filopodia. The following parameters were used to classify the spines in our data:

- Head-to-neck ratio: 1.1
- Length-to-head ratio: 2.5
- Mushroom head size: 0.35 µm
- Filopodium length: 3.0 µm

Novel modifications to the commercial pipeline specific to ExM included (i) the application of the Grayscale Morphological Closing filter, (ii) modification of default parameterization settings to accommodate expanded tissues' isotropic expansion, (iii) as well as an implementation of a method to perform post-hoc scaling adjustment, which included a re-computation of the spine surface. Additionally, the dendritic spine model was modified at multiple stages to allow capture of metrics related to the dendritic spine neck and head boundary, the position of the head and neck centroids along the dendritic spine backbone, and attachment points along the dendrite surface. Finally, an average neck diameter computation was developed which averages the Rayburst diameter of all layers below the spine head. By convention, we considered the base of the head to be one head radius below the designated head center (*125*). Since the spine may appear detached due to imaging or image segmentation (although we know that spines are always physically attached to the dendrite), we estimated the number of layers that would occupy the gap between the visible head and the dendrite and assigned a minimum diameter to those layers in order to include them in the average. The assigned minimum diameter was equal to one half the lateral resolution of the image.

g. Dendritic spine - Homer1 puncta association

Association between dendritic spines and Homer1 puncta was determined using a *K*d-tree nearest neighbor search algorithm based on their *xyz* coordinates corrected for the *z*-anisotropy, where a *K*d-tree model of all dendritic spines was built using *KDTreeSearcher* MATLAB function.

Subsequently, all Homer1 puncta within the head radius of each spine was determined from the Euclidian distance search using *rangesearch* MATLAB function.

h. Tracing of neurites

Semi-automatic or manual tracing and reconstruction of somas and neurites were carried out using Bitplane Imaris x64 FilamentTracer and Contour Surface (ver. 9.0.0, Oxford Instruments), Arivis Vision4D (ver. 2.12.6, Arivis), or VVD Viewer (ver. 1.00, HHMI Janelia Research Campus).

i. Local maxima detection

The nc82 puncta positions were determined by detecting their local signal maxima using a 3D Laplacian-of-Gaussian filter described previously (*121*) on 3D volumes that have been pre-processed to remove non-specific signals. The detected local maxima of nc82 closer than 100nm were merged by using their mean position using *KDTreeSearcher* and *knnsearch* MATLAB functions. These nc82 puncta were determined to be dopaminergic neuronal (DAN) membrane associated if the nc82 local maxima position was colocalized with the membrane signal. The DAN membrane and nc82 were determined to be colocalized if the DAN membrane voxel value at nc82 local maxima positions was above the membrane threshold value. This threshold value was determined by taking the 99^{th} percentile of all values at the edge of the segmented membrane volume.

Since Homer1 signals did not appear as diffraction-limited objects, their 3D volumes were pre-processed to remove non-specific signals and discrete objects with less than 246 connected voxels (fig. S33). The centroid position of Homer1 signals was determined using *regionprops3* function in MATLAB.

The local density and local Euclidian distance to the closest neighbor was calculated on their *xyz* coordinates corrected for the *z*-anisotropy using *K*d-tree nearest neighbor algorithm, where either the nc82 or Homer1 positions were used to generate a model using *KDTreeSearcher* MATLAB function. Subsequently, the local density was calculated using *rangesearch* MATLAB function, where the search radius facilitated a 1 μm^3 search volume. The distance to the closest neighbor was calculated by querying the model to itself using *knnsearch* MATLAB function, where the second closest object corresponded to the closest neighbor.

j. Surface area and volume calculations

The surface area and volume of segmented objects was calculated as described previously (*106*). Briefly, all 3D volumes were interpolated to correct for the *z*-anisotropy. Volume was calculated by converting the sum of the segmented isotropic voxels into cubic microns. The surface area was calculated by converting the sum of the segmented isotropic voxel mask perimeter into squared microns.

5. Visualization

Datasets were visualized using Vision4D (Arivis), Imaris x64 8.4-9.1 (Oxford Instruments), VVD Viewer (ver. 1.00, HHMI Janelia Research Campus), or Amira 6.3-6.5 (Thermo Fisher Scientific) for volumetric rendering. Unless otherwise stated, all visualized datasets were flat-field corrected, deconvolved, stitched, gamma adjusted, and filtered to remove non-specific signals. For applicable datasets, where data from multiple channels were not spatially overlapping, the channels were merged into a single volume by rescaling each channel to fill a discrete portion of a 16-bit intensity space. Custom colormaps decoding the channels in varying intensity space were created to visualize multichannel data.

Rendering the max intensity projection with perspective-view of the multiterabyte fly brain dataset using Arivis Vision4D generated down-sampling interpolation artifacts. To overcome this limitation, we used a custom MATLAB script to generate a full resolution perspective-view MIP for each of the brain regions highlighted in Fig. 7E. The full resolution MIPs (27,964 by 15,055 pixels) of DAN membrane and nc82 channels for each region were generated independently and the final figure panel was assembled in Adobe Photoshop CS6. The brightness, contrast and gamma parameters of the neuropil layers were adjusted in Fiji. The neuropil layer ordering along with nc82 layer opacity parameters were optimized in Photoshop during final assembly to aid in the visualization of small punctate structures.

The analyzed nc82 (all or dopaminergic neuron associated, Fig. 7A and Movie 9), local G-Ratio, and axon-myelin distance were visualized by rendering color-coded spheres using the *Point Cloud View* in Amira. In the case of nc82, the spheres were color-coded for the local density of all nc82 within a 1 μm^3 volume. In the myelinated axon, the myelin surface was presented as a series of spheres color-coded for either G-Ratio or myelin thickness.

6. Additional Notes for ExLLSM Datasets

a. Segmentation and reconstruction of organelles (Fig. 2, A to E, and fig. S8)

Because the primary antibodies against Tom20 and LAMP1 were from the same animal host, we applied a sequential blocking and immunostaining strategy to reduce cross-talks between the two channels. However, there were still residual cross-talks caused by LAMP1 secondary antibody targeting the Tom20 primary antibody. Therefore, to prevent counting LAMP1 false positives, we first assigned mitochondria with the Tom20 channel and then assigned the lysosomes to the remaining subcellular compartments with the LAMP1 channel. In addition, we identified lysosomes only when the immunostained LAMP1 label was volumetrically occupying the compartment. Therefore, the identified lysosomes are likely multivesicular bodies or autolysosomes, in which the LAMP1 proteins can be found inside the vesicles.

The median length of mitochondria major axis (0.90 μm) in Fig. 2D was substantially smaller than the mean length of ~2.6 μm in cultured mouse cortical neurons (*126*), and the mean projection length of ~2.8 μm in dendrites (*127*) in previous diffraction-limited light-microscopy studies. We note this discrepancy is likely due to the increased counts of sub-diffraction mitochondria in the ExLLSM statistics.

b. Podocyte morphology of renal glomerulus (fig. S32)

We imaged an entire human kidney glomerulus cross-section with only immunostained fluorescent labels (*98*). While part of an expanded human kidney glomerulus has been imaged with a confocal microscope (*98*), we hypothesized that the voxel speed and close-to-isotropic resolution of our imaging pipeline could allow us to image the entire glomerulus cross-section with higher speed and better resolution.

Briefly, we imaged a ~220 by 220 by 22 μm volume (post-expansion size ~1.0 by 1.0 by 0.10 mm) to capture the complete cross-section of an expanded human kidney glomerulus (fig. S32). The sample was prepared following the expansion pathology (ExPath) protocol with immunostaining against Vimentin, actinin-4 and collagen IV (*98*), a protocol optimized to yield high-density and low-background staining in pathological samples. Using the actinin-4 channel, we were able to identify podocyte foot processes from a normal human kidney, similar to the ultrastructure observed in previous pathological SEM studies (*128*). We further found that the foot

processes had a ~290 nm periodicity, consistent with the values reported in the previous ExPath studies (Fig. 4c of (*98*)). Using the objective-scan mode, the whole glomerulus cross-section was imaged within 9.5 hours for 3-colors with minimal bleaching, considerably faster than EM and other light microscopy methods. By switching to the sample scan mode, a complete cross-section of the glomerulus could be imaged within 1.2 hours, suitable for high-throughput screenings of pathological samples.

c. Nc82 puncta as the presynaptic site label (fig. S23)

First, we used Brp null mutant with BAC rescue of Brp tagged with V5 epitope peptide (Brp-V5) at the N-terminal of the Brp protein to test detection efficiency of the nc82 antibody. We found that up to 62% of nc82 puncta were within 70 nm and up to 73% were within 100 nm from the closest V5 tag in CA (fig. S23). This result is consistent with the postulated distance of C- and N-terminals of Brp and implicates that it is rare that nc82 mis-detect all the Brps in a given Brp oligomer (*78*). Next, we introduced Flag-tagged Syd1 in DC3 PNs and studied its colocalization with the nc82 puncta in their boutons in CA and LH. Syd1 is a different presynaptic protein that form active zone molecular complex with Brp. We found that up to 58% of the nc82 puncta were within 150 nm and up to 80% were within 200 nm from the closest Syd1 puncta (fig. S23). This result is consistent with the postulated distance from the Brp nc82 epitope to Syd1 (*84*). Combined, these results confirm that the majority of nc82 puncta represent the location of active zone molecular complex.

d. Association of nc82 puncta to neurons (figs. S24, S25, and S27)

A recent FIB-SEM study (*83*) found virtually no presynaptic densities in the dendritic branches of MBON-α1, despite finding 35,440 presynaptic densities associated with other cell types inside α1. To validate our method of identifying the nc82 puncta associated with neurons, we imaged the entirety of MBON-α1 and checked to if we could observe a similar difference in puncta density between its dendrites and axon terminals (fig. S24). As expected, we found that the nc82 puncta surface density at MBON-α1 axons terminals (~4.16 puncta/μm^2) was about 70 time higher than that at its dendrites (~0.06 puncta/μm^2). On the other hand, we found ubiquitous nc82 puncta at the somata (fig. S27) and dendrites of other DANs including those inside the MB (fig. S25). Together, these observations serve to validate the nc82 puncta association algorithm used in this study (*77*, *83*).

e. Nc82 puncta statistics in MB α3 using ExLLSM and FIB-SEM (figs. S22, S25, and S26)

We chose the α3 compartment for benchmarking, because the spatial distributions of presynaptic densities are known from a previous FIB-SEM study (fig. S22) (*83*). We first determined the precise location of all the nc82 puncta in the MB α3, and their association to the DAN membrane signals. Using our analysis pipeline, we were then able to identify ~48,000 nc82 puncta in MB α3, ~8.5% of which were associated with DANs (fig. S25). We found that the overall distribution of inter-nc82 puncta distances were similar to that of the inter-presynaptic density distances in the FIB-SEM study. The total number of presynaptic sites and the ratio of DAN association were higher compared with the FIB-SEM results (MB α3 (FIB-SEM): ~34,000 presynaptic densities with ~4.5% of the presynaptic densities associated with two DANs (PPL1-α3-A and PPL1-α3-B) innervating the compartment) (*83*).

To address these differences, we further conducted a systematic study of MB α3 compartments of four additional brains from three females (fig. S26). For the two animals in which we studied the compartments from both hemispheres (e.g., the TH-GAL4 specimen in fig. S25 and one of the wild-type specimens in fig. S26), the number of nc82 puncta were within ~10% of one another, suggesting our method provides consistent statistics within the same animal. In addition, we found that the nc82 puncta can vary from ~34,000 to ~49,000 within the imaged specimens, suggesting that the difference observed between the ExLLSM study and the FIB-SEM study is within the natural variability between animals. Finally, even if there are systematic differences counting synapses between FIB-SEM and ExLLSM, comparison between different brain regions for a given imaging method should still be valid.

f. Cell type classification of the eight PPM3 cluster neurons in the adult Drosophila brain and comparison with individual labeled neurons using multicolor flip-out (MCFO) and split-GAL4 strains (figs. S20 and S21)

The PPM3 cluster neurons (eight per hemisphere) were classified into five morphologically distinguishable cell types in ExLLSM data. The two traced PPM3-EB neurons (A1: frontal view; A2 diagonal view) are shown in fig. S20A. The cell bodies of the PPM3 cluster neurons are located at the posterior medial surface of the brain. All 8 PPM3 neurons project their primary neurites to the anterior side of the brain through the same tract, and then axonal branch takes one of three tracts to innervate the central complex. We compared morphology of traced neurons with images of MCFO and split-GAL4 images to match cell type identity. Although position of cell bodies

varied among individuals, tracts and branching of primary neurites were stereotypical (fig. S21, B, D, F, and G), and could be used as minimal criteria for cell type identification (table S5).

A MCFO image of single PPM3-EB neuron is shown in fig. S20B. In addition to eponymous ellipsoid body, PPM3-EB neuron also bilaterally innervates noduli and bulb (aka lateral triangle) and arborize their dendrites in the ipsilateral lateral accessory lobe. Arrowheads indicate tract A to the ellipsoid body. *R14C08p65ADZp in attP40; DDC-ZpGAL4DBD in attP2* split-GAL4 driver labels two PPM3-EB neurons per hemisphere, which are shown in fig. S20C.

The two traced PPM3-FB3 neurons are shown in fig. S20D. Axonal branch of PPM3-FB3 neurons project through the hole surrounded by ellipsoid body (arrowheads; tract B) to the eponymous layer 3 of the fan-shaped body. This unique trajectory of axons distinguishes them from the PPM3-FB3-NO. PPM3-FB3 and/or PPM3-FB3-NO likely correspond to the previously described cell type of PPM3 neurons that innervate the medial fan-shaped body (PPM3-mFB) (*129*). An image of single PPM3-FB3 neuron is shown in fig. S20E. Major dendritic branches of PPM3-FB3 neurons are located in the ipsilateral superior intermediate protocerebrum and lateral accessory lobe. Split-GAL4 driver SS48802 (VT014729- p65ADZp in attP40; VT033647-ZpGAL4DBD in attP2) labels two PPM3-FB3 neurons per hemisphere, which are shown in fig. S20F.

The two traced PPM3-FB2-NO neurons are shown in fig. S20G. The axonal branch of two PPM3-FB2-NO neurons project to the layer two of the fan-shaped body (arrowheads; tract C). In fig. S20H, we did not obtain any MCFO image of single cell image of PPM3-FB2-NO in 63 brains examined. Split-GAL4 driver *SS48817* (*VT009650-p65ADZp in attP40; VT033647-ZpGAL4DBD in attP2*) labels two PPM3-FB2-NO neurons per hemisphere, which are shown in fig. S20I.

The traced PPM3-FB3-NO-a and PPM3-FB3-NO-b neurons are shown in fig. S20J. They send their axonal branch to the layer 3 of the fan-shaped body through the same tract as that of PPM3-FB2-NO neurons (arrowheads; tract C). “a” and “b” cell can be distinguished by the additional dendritic branches (arrows; branch 1 and 2).

A previous report indicated that only 6 of eight PPM3 cluster neurons in TH-GAL4 show strong immunoreactivity to anti-Tyrosine Hydroxylase (anti-TH) (*80*). On the other hand, substantial immunoreactivity to dopamine itself can be detected even in the neurons that are faintly immunoreactive to anti-TH (*130*). Therefore, whether all 8 PPM3 cluster neurons use dopamine as the main neurotransmitter needs further functional validation.

Supplementary Figures

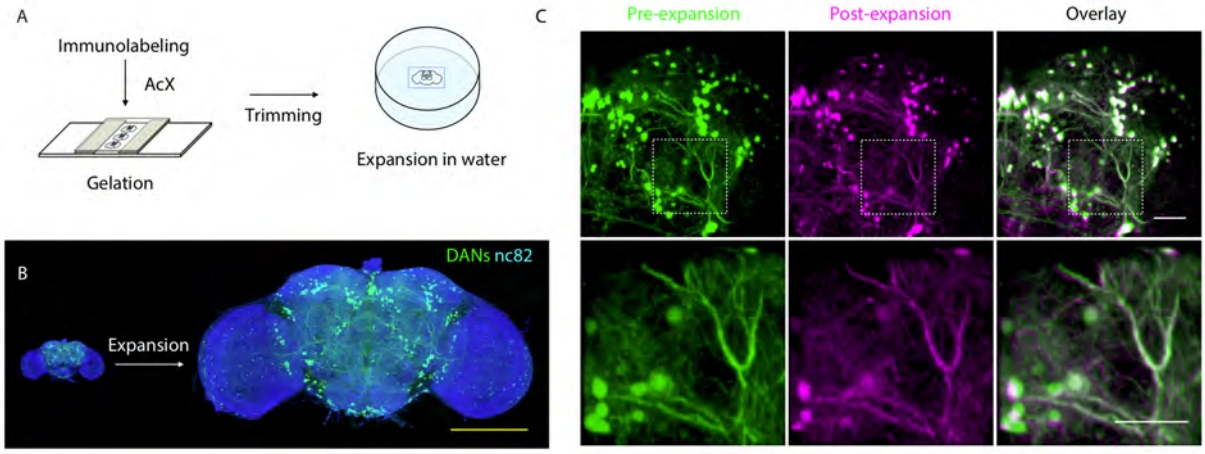

Fig. S1. Expansion of a *Drosophila* brain. (A) Schematic of steps involved in the expansion. (B) Maximum intensity projections (MIP) of an adult *Drosophila* brain with fluorescently labeled dopaminergic neurons (DANs, green) and presynaptic active zone protein Bruchpilot (nc82, cyan) in pre-expanded (left) and post-expanded (right) states. Scale bar, 500 µm, in post-expansion (as imaged) size. (C) MIPs of the DANs in the same specimen, shown pre-expanded (left, green), post-expanded (middle, magenta), and mutually overlaid. Magnified views of the boxed regions are shown below. Scale bars, 25 µm, here and elsewhere in pre-expansion (i.e., biological) size, unless otherwise noted.

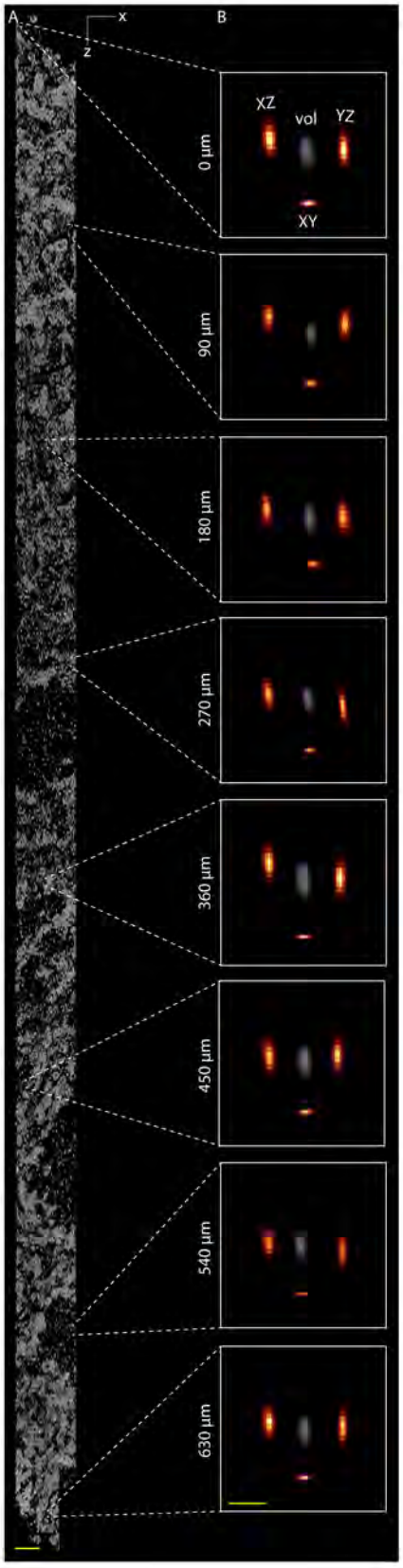

Fig. S2. Uniformity of resolution throughout expanded brain tissue. (A) Volume rendering of mitochondria-targeted Tom20 antibody puncta in a tissue section from the mouse somatosensory cortex (S1), imaged by LLSM in objective scan mode (LLSM (OS)). Scale bar, 10 µm in post-expansion (as imaged) size. (B) Volume rendered PSFs (middle in each panel) and corresponding XY (bottom in each panel), XZ (left in each panel), and YZ (right in each panel) MIPs at different imaging depths. Scale bar, 1 µm in post-expansion (as imaged) size.

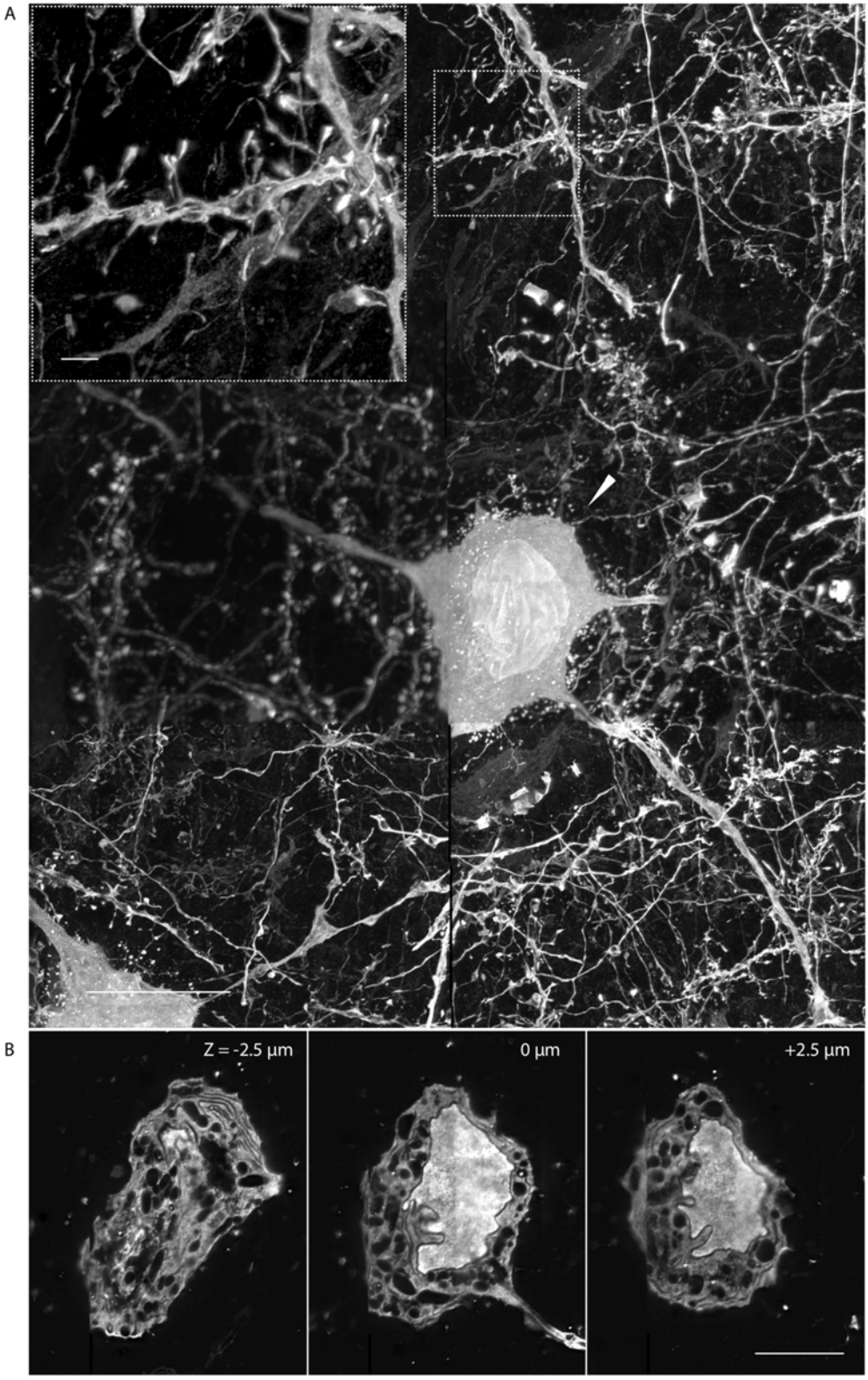

Fig. S3. ExLLSM imaging at a higher expansion ratio. (A) MIP view of a ~10 µm thick slab (post-expansion thickness ~68 µm) of Thy-1 YFP mouse cortex prepared following a high expansion protocol (expansion factor ~6.81). Scale bar, 10 µm. Inset, magnified view of the boxed region. Scale bar, 1 µm. (B) Three orthoslices through the soma indicated by the white arrow in A, taken at ~2.5 µm (pre-expansion) intervals in z, showing distortion of nucleus. Scale bar, 5 µm.

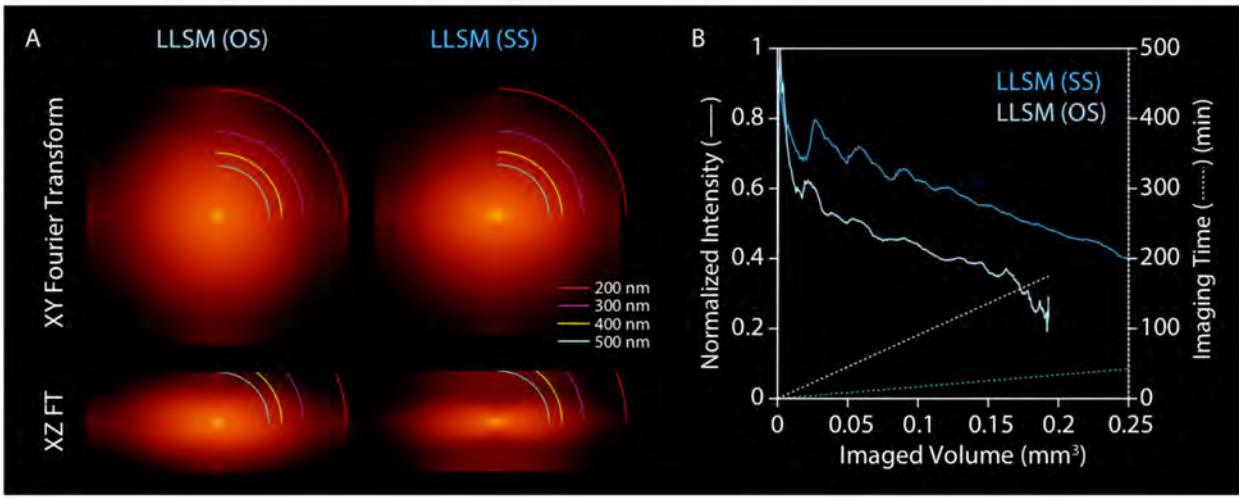

Fig. S4. ExLLSM in objective scan (OS) mode. (A) XY (top) and XZ (bottom) cross-sections of the 3D Fourier transforms of diffraction limited puncta produced by Tom20 antibodies in a ~100 μm^3 expanded cube of Thy1-YFP mouse primary somatosensory cortex tissue, imaged by LLSM in objective scan mode (LLSM (OS), light blue) and sample scan mode (LLSM (SS), blue). Both datasets were deconvolved using measured point-spread-functions (PSFs). Sample scan mode continuously sweeps the sample through the light sheet to achieve higher speed, but at the cost of a slight reduction in resolution in y and z due to the motion of the sample during the acquisition of each image. (B) Comparative bleaching rates and imaging speed in the YFP channel for LLSM (OS) and LLSM (SS). Post-expansion loss of fluorescence can contribute to bleaching even in the absence of light.

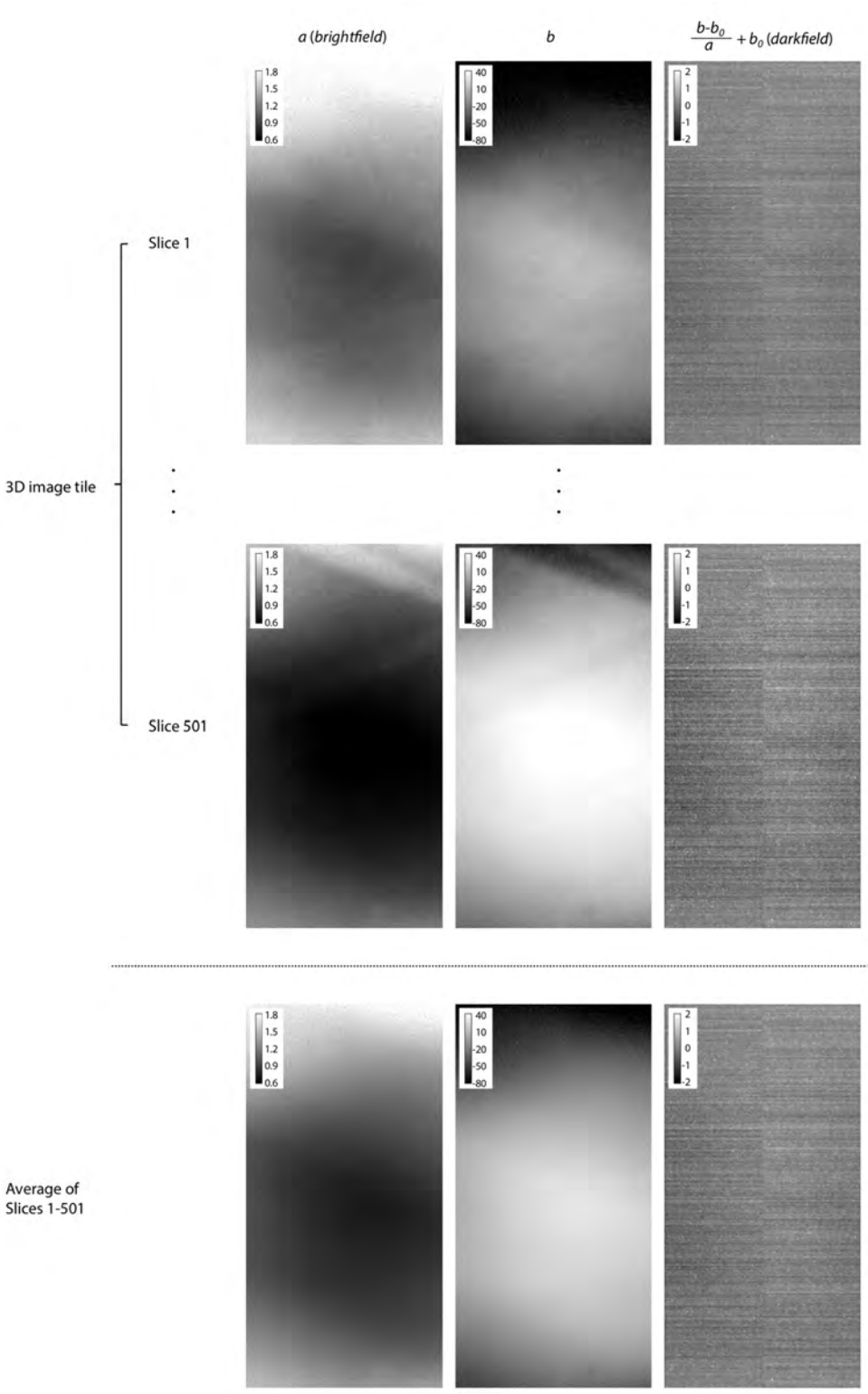

Fig. S5. Estimation of darkfield and brightfield. Brightfield (*a*, left column), offset (*b*, middle column), and darkfield ($(b-b_0)/a + b_0$, right column, calculated from the brightfield and offset) of the first image slice (slice 1, top row), the last image slice (slice 501, middle row), and average intensity projection (AIP) of all 501 image slices (slices 1-501, bottom row), estimated from 25788 3D image tiles of an ExLLSM adult *Drosophila* brain dataset (nc82 channel, Sample 12, table S2). The darkfield was extracted using a value of 101 for the background intensity (b_0). The flat-field correction was given by $y = ax + b$, where x is the observed intensity value, and y is the corrected value.

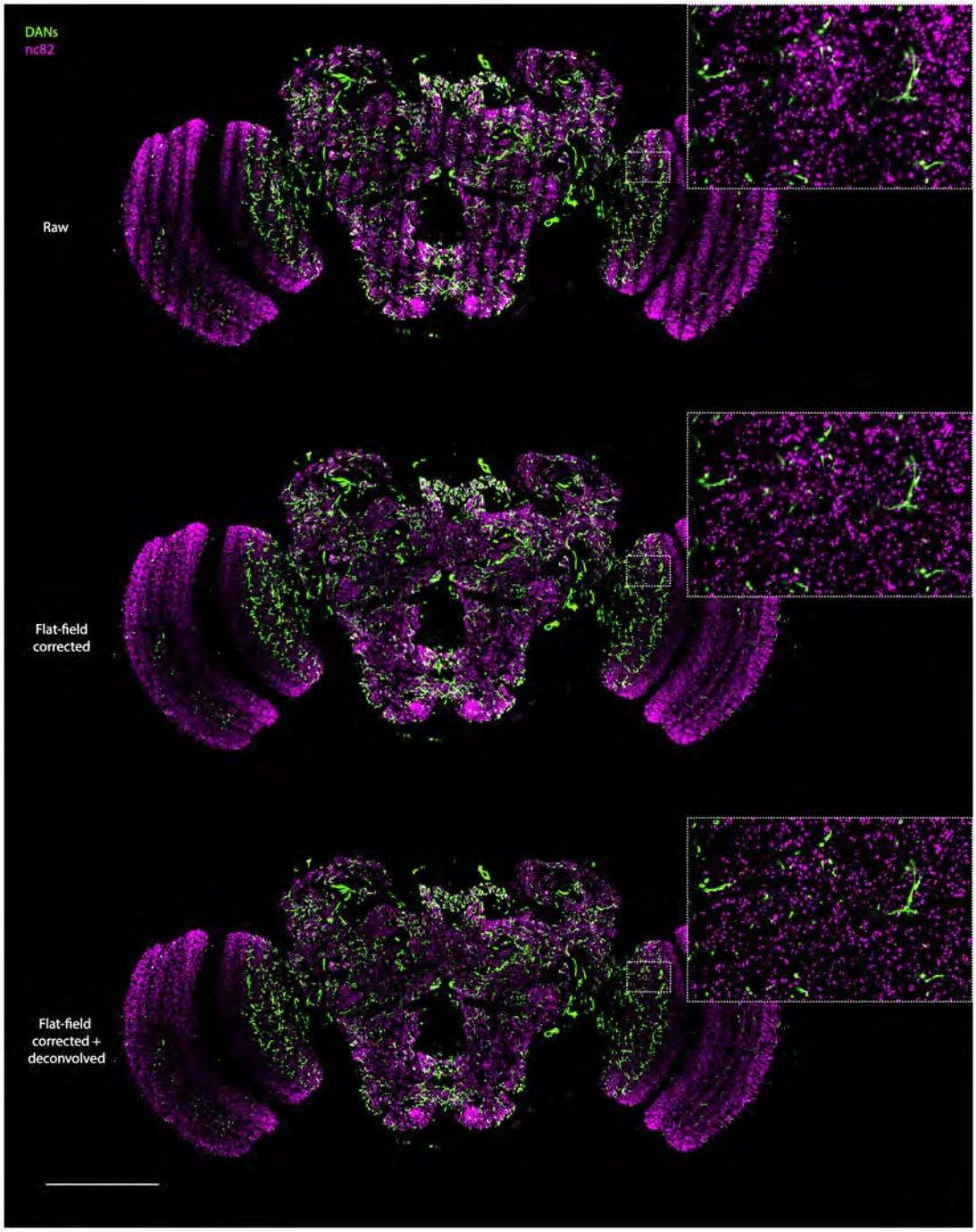

Fig. S6. Flat-field correction. Cross-sectional view of stitched 3D image tiles of an ExLLSM adult *Drosophila* brain dataset (nc82 channel, Sample 12, table S2) using raw (top), flat-field corrected (middle), and flat-field corrected + deconvolved tiles (bottom). The two color channels of the dataset are shown in green (DANs) and magenta (nc82). The 2D cross-sectional plane encompasses 2248 3D image tiles per color channel. Scale bar, 100 μm. Insets, magnified view of the boxed regions.

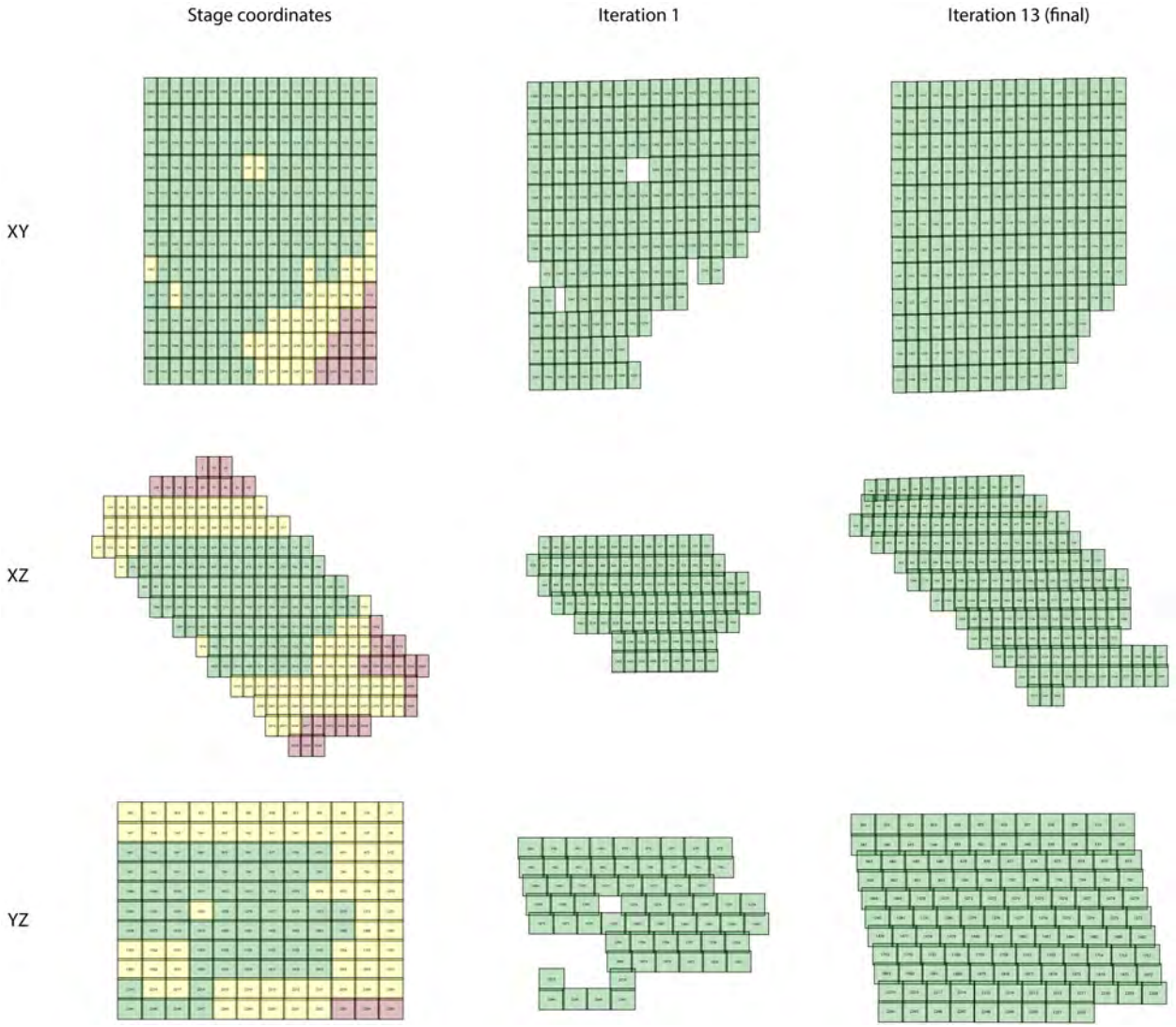

Fig. S7. Automated iterative stitching. Image tile layouts of an ExLLSM *Drosophila* brain dataset (Sample 11, table S2) using stage coordinates (left column), coordinates after 1 stitching iteration (middle column) and 13 stitching iterations (1 stitching iteration starting with the stage coordinates + 12 iterations of prediction-based rematching, right column). Only the image tiles from the mid cross-sectional planes of XY (top row), XZ (middle row), and YZ (bottom row) of the dataset are shown for simplicity. The color-coded tiles indicate those included in the final stitched dataset after iteration 1 (green) and iteration 13 (yellow), and those rejected after iteration 13 (red) due to lack of signals or low cross-correlation with other tiles.

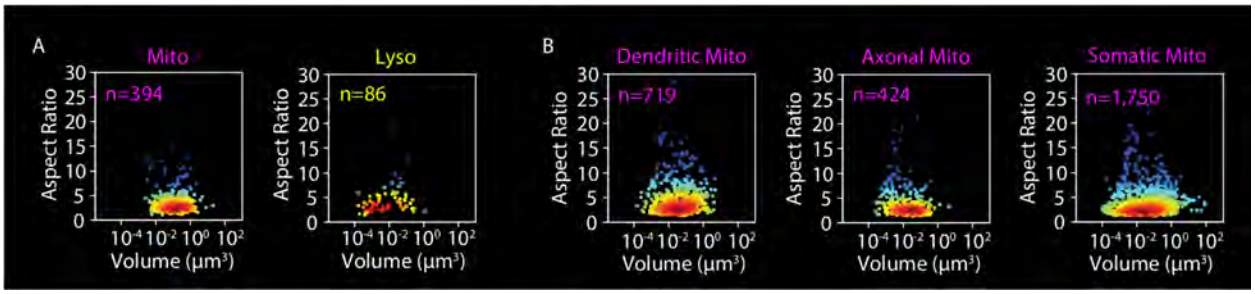

Fig. S8. Mitochondria and lysosome morphology of layer V pyramidal neurons in the mouse somatosensory cortex. (A) Scatter plot of aspect ratio versus volume for the mitochondria (Mito, magenta) and lysosomes (Lyso, yellow) in Fig. 2C. (B) Scatter plots for the mitochondria, further broken down by location within the neuron as shown. See Fig. 2, A to E.

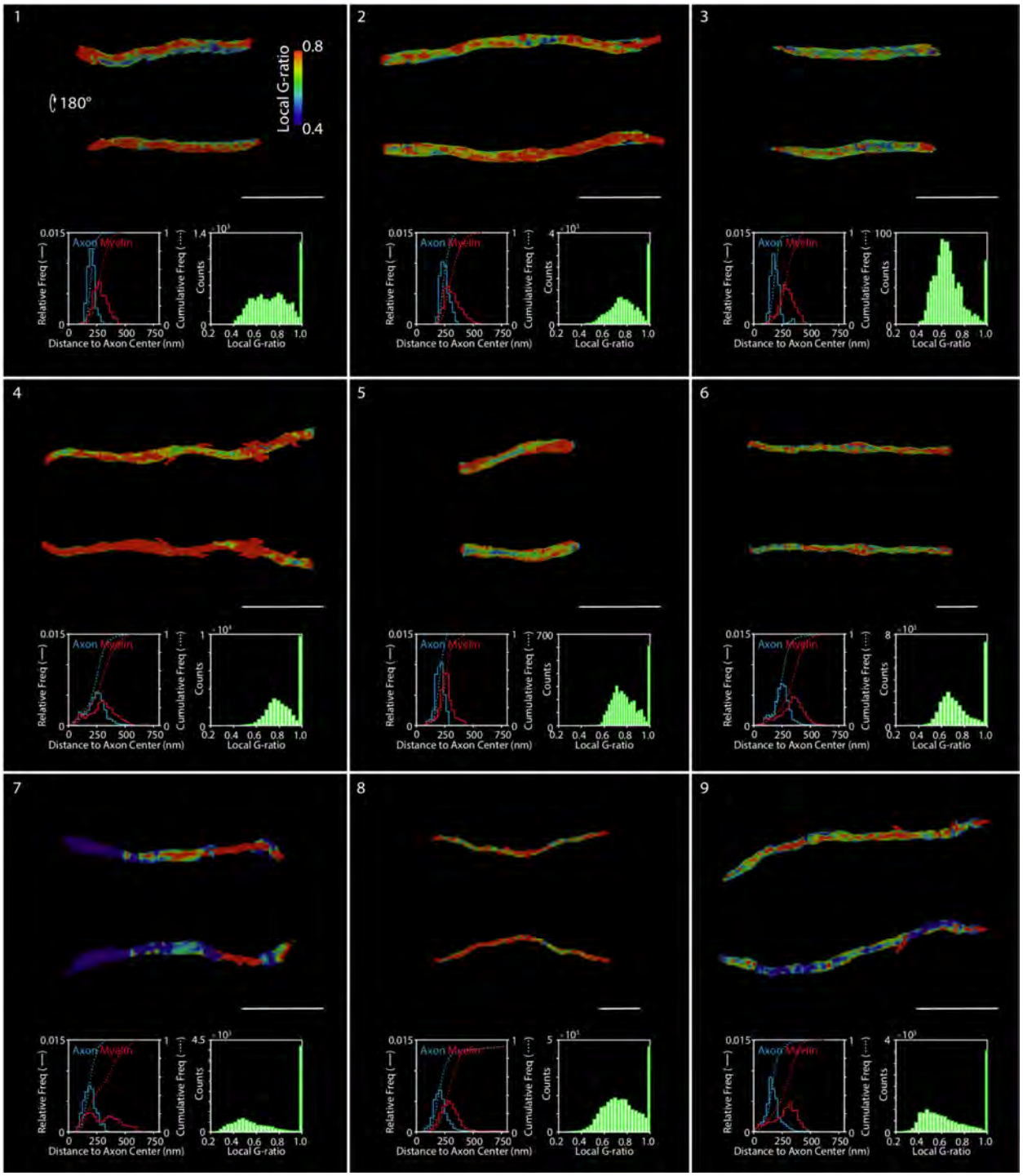

Fig. S9. Local g-ratio in nine myelinated axon segments of layer V pyramidal neurons in the mouse primary somatosensory cortex. Myelinated axon segments color-coded by local g-ratio (top), with distributions of axon radius, myelin outer radius (bottom left), and g-ratio (bottom right) at all points on each segment. Scale bars, 5 μm. See Fig. 2, F and G.

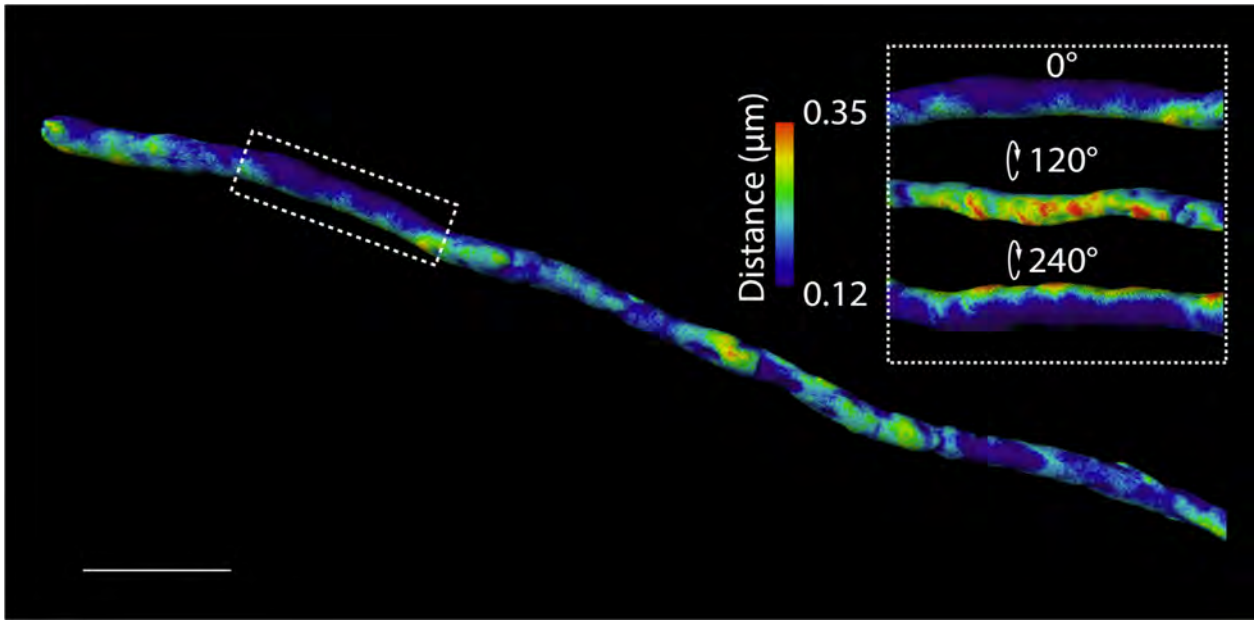

Fig. S10. Distance from axon outer radius to myelin sheath outer radius for the same axon segment in Fig. 2F. Scale bar, 5 μm. Inset shows azimuthal variation in gap distance in the rectangle at left. See Fig. 2G.

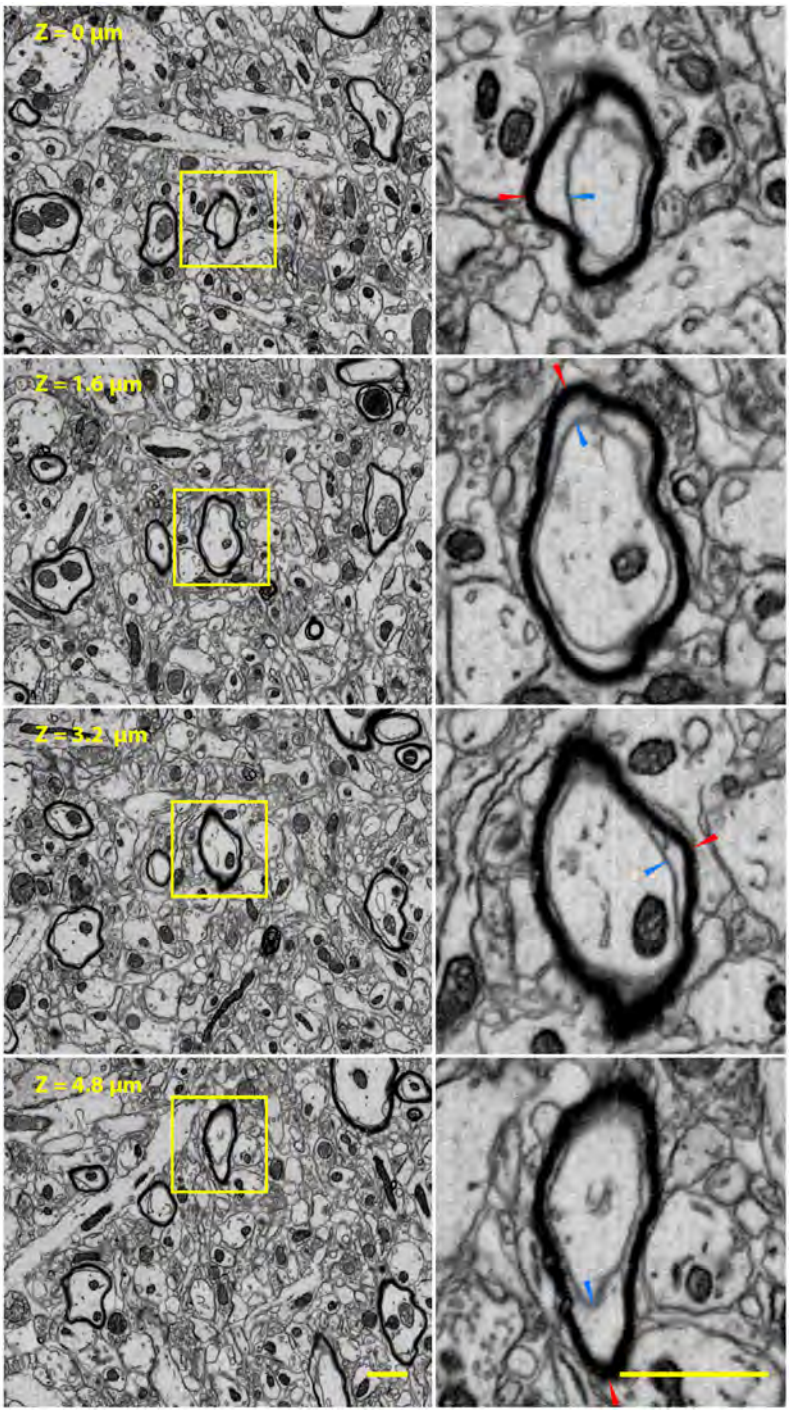

Fig. S11. FIB-SEM cross-sectional views of myelinated axons in the mouse hippocampus. Left: four successive views at 1.6 µm intervals. Right: magnified views from a single axon marked by the boxed regions at left. Arrows indicate the outer surfaces of the myelin sheath (red) and the axon (blue). Scale bars, 1 µm.

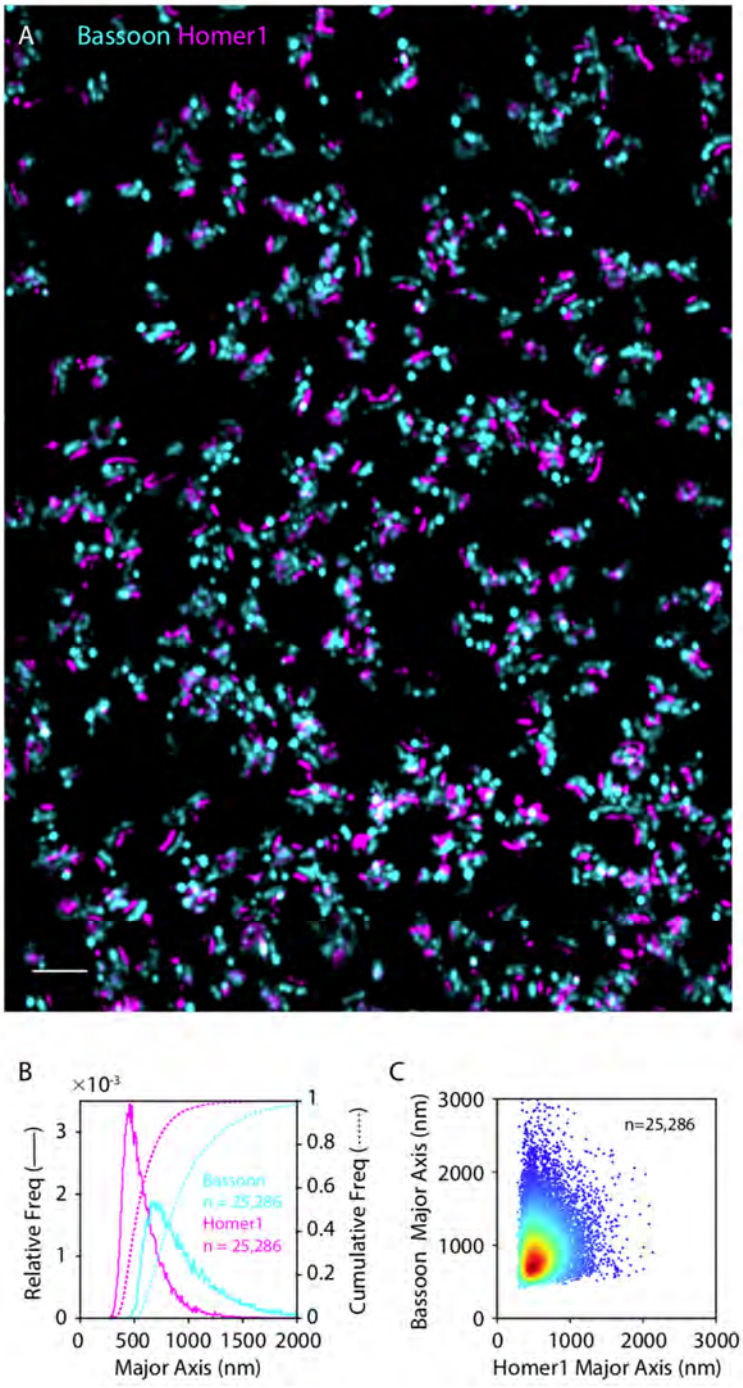

Fig. S12. Bassoon-Homer1 pairs in the mouse primary somatosensory cortex. (A) MIP view of a ~9.3 μm thick slab from a Thy1-YFP mouse of all Bassoon (cyan)-Homer1 (magenta) pairs within the slab. Scale bar, 1 μm. (B) Distribution of major axis lengths of all Bassoon (cyan) and Homer1 (magenta) structures within the imaged volume. (C) Scatter plot of the major axis lengths of all the paired Bassoon-Homer1 puncta within the imaged volume. See Fig. 2, I to K.

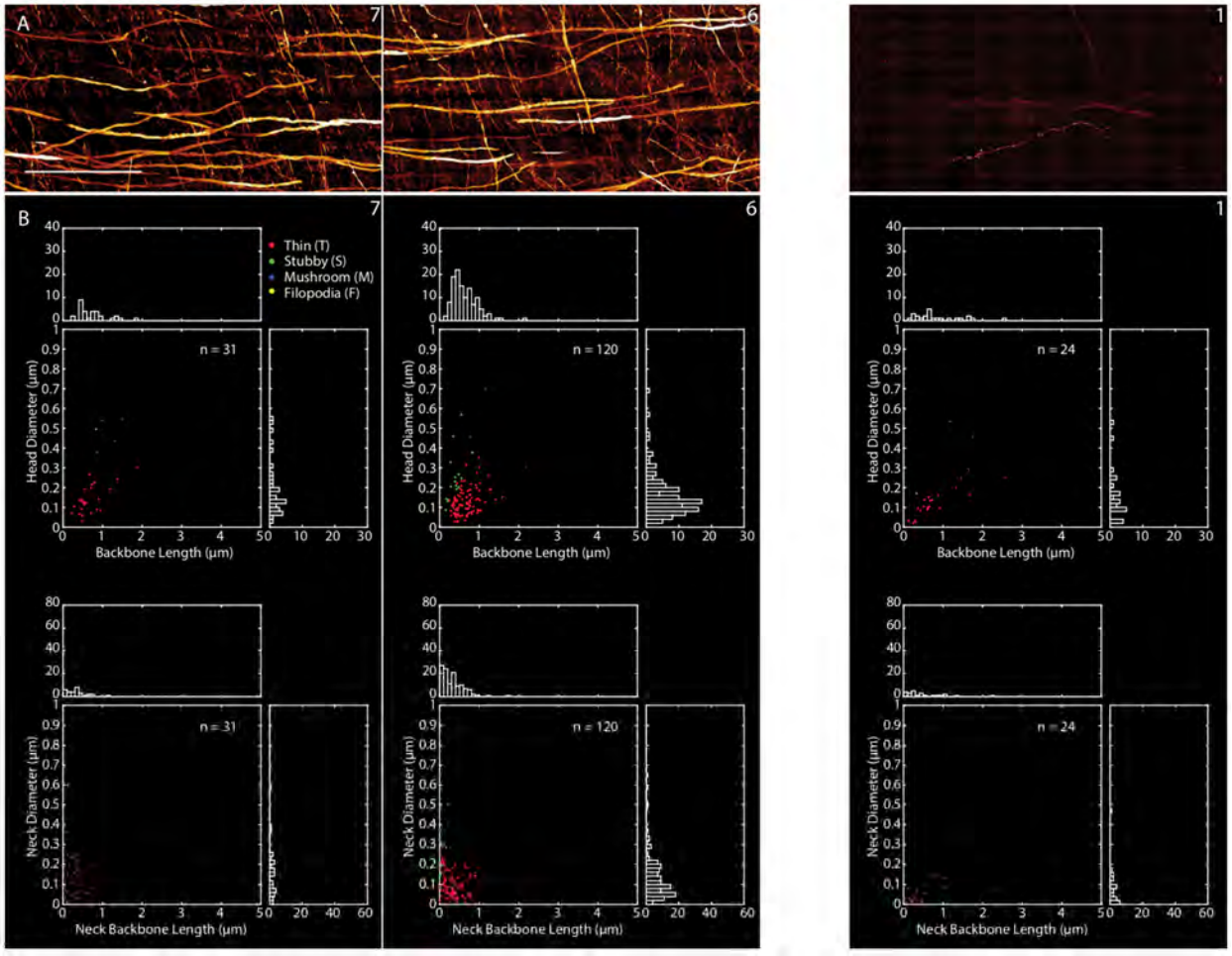

Fig. S13. Morphological parameters of dendritic spines of layer V pyramidal neurons in the mouse primary somatosensory cortex. (A) MIP views of the remaining three boxed regions from Fig. 3A. Scale bars, 50 µm. (B) Scatter plots and histograms of backbone length and head diameter (top row), and neck backbone length and neck diameter (bottom row) in each of the three regions. See Fig. 3C. Spines were semi-automatically reconstructed from four ~27 by 27 by 14 µm (~100 by 100 by 50 µm) subvolumes stereologically sampled at each position. T (red), S (green), M (blue), and F (yellow) indicate thin, stubby, mushroom, and filopodia dendritic spines, respectively.

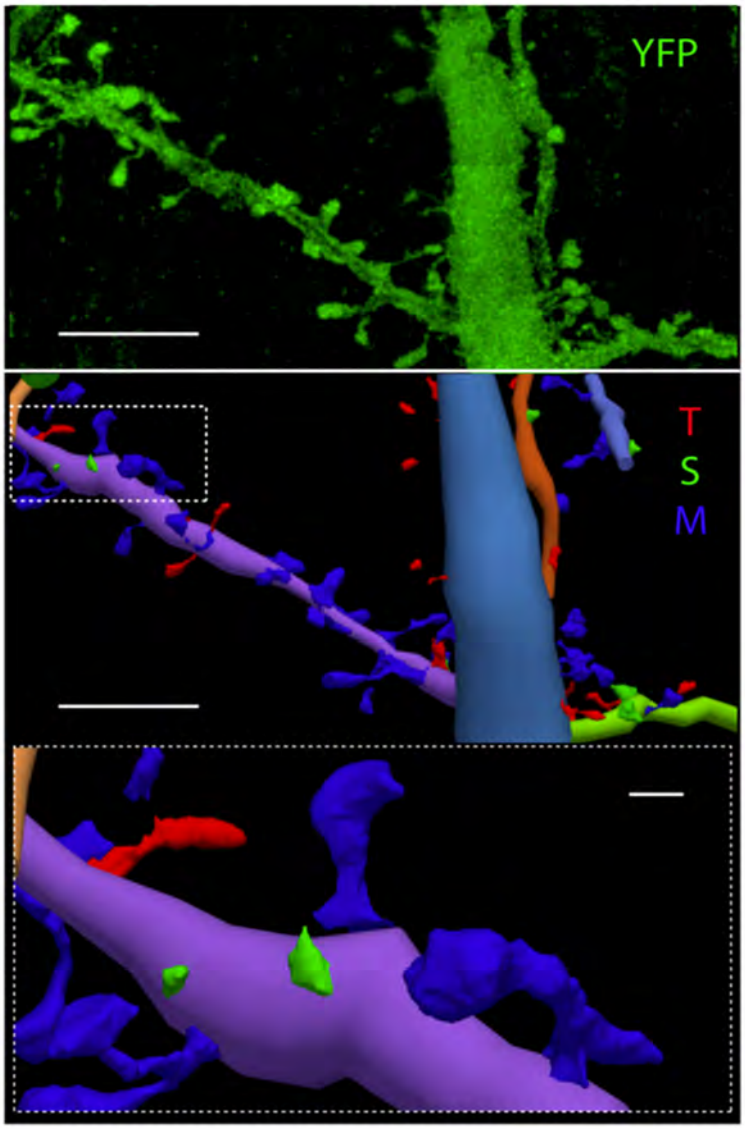

Fig. S14. Dendritic spine reconstruction. MIP view of the YFP channel from a ~27 by 27 by 14 µm (~100 by 100 by 50 µm) subvolume at position 3 of Fig. 3A (top) and the resulting reconstructed dendrites and dendritic spines (middle). Scale bars, 5 µm. A magnified view of the boxed region is shown at bottom. Scale bar, 1 µm. T (red), S (green), and M (blue) indicate thin, stubby, and mushroom dendritic spines, respectively. See also movie S2.

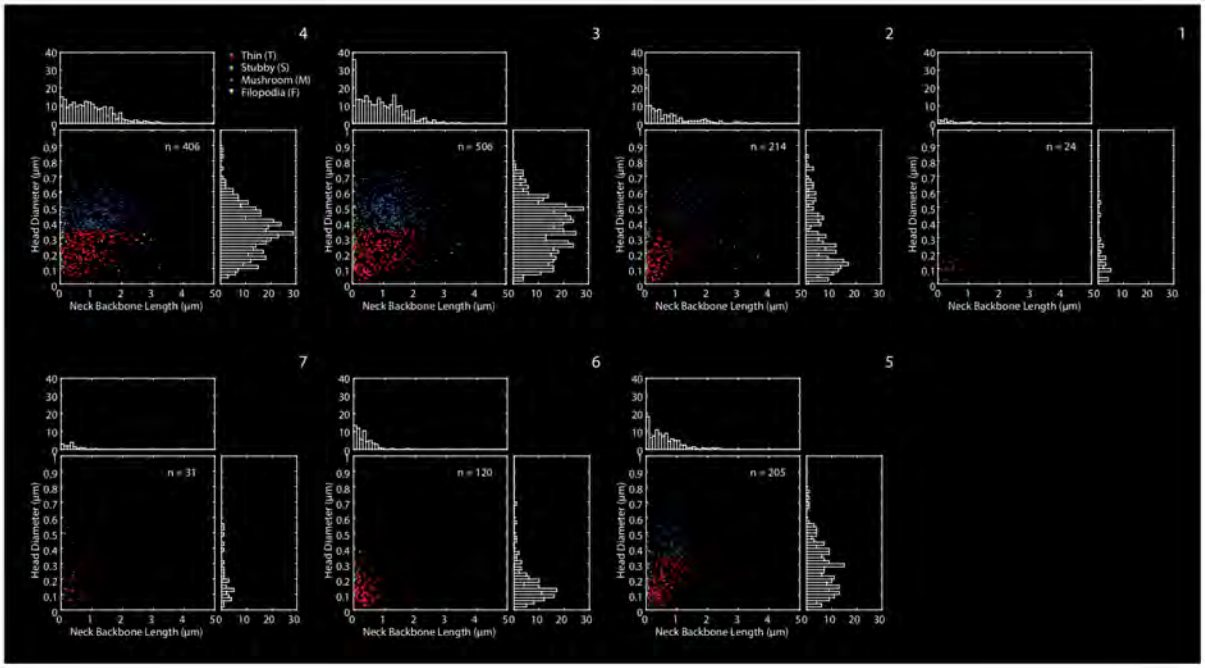

Fig. S15. Scatter plots of neck backbone length versus head diameter for layer V pyramidal neuron dendritic spines in seven different regions of the mouse primary somatosensory cortex. Dendritic spines were semi-automatically reconstructed from four ~27 by 27 by 14 µm (~100 by 100 by 50 µm) subvolumes in each of the seven regions in Fig. 3A. T (red), S (green), M (blue), and F (yellow) indicate thin, stubby, mushroom, and filopodia dendritic spines, respectively.

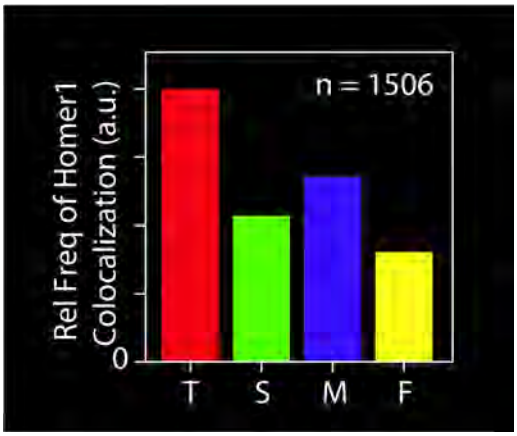

Fig. S16. Relative frequency of dendritic spine association with Homer1 puncta for each spine morphology type of layer V pyramidal neurons in the mouse primary somatosensory cortex. The results combine data from all 28 subvolumes sampled across the cortex. T (red), S (green), M (blue), and F (yellow) indicate thin, stubby, mushroom, and filopodia dendritic spines, respectively.

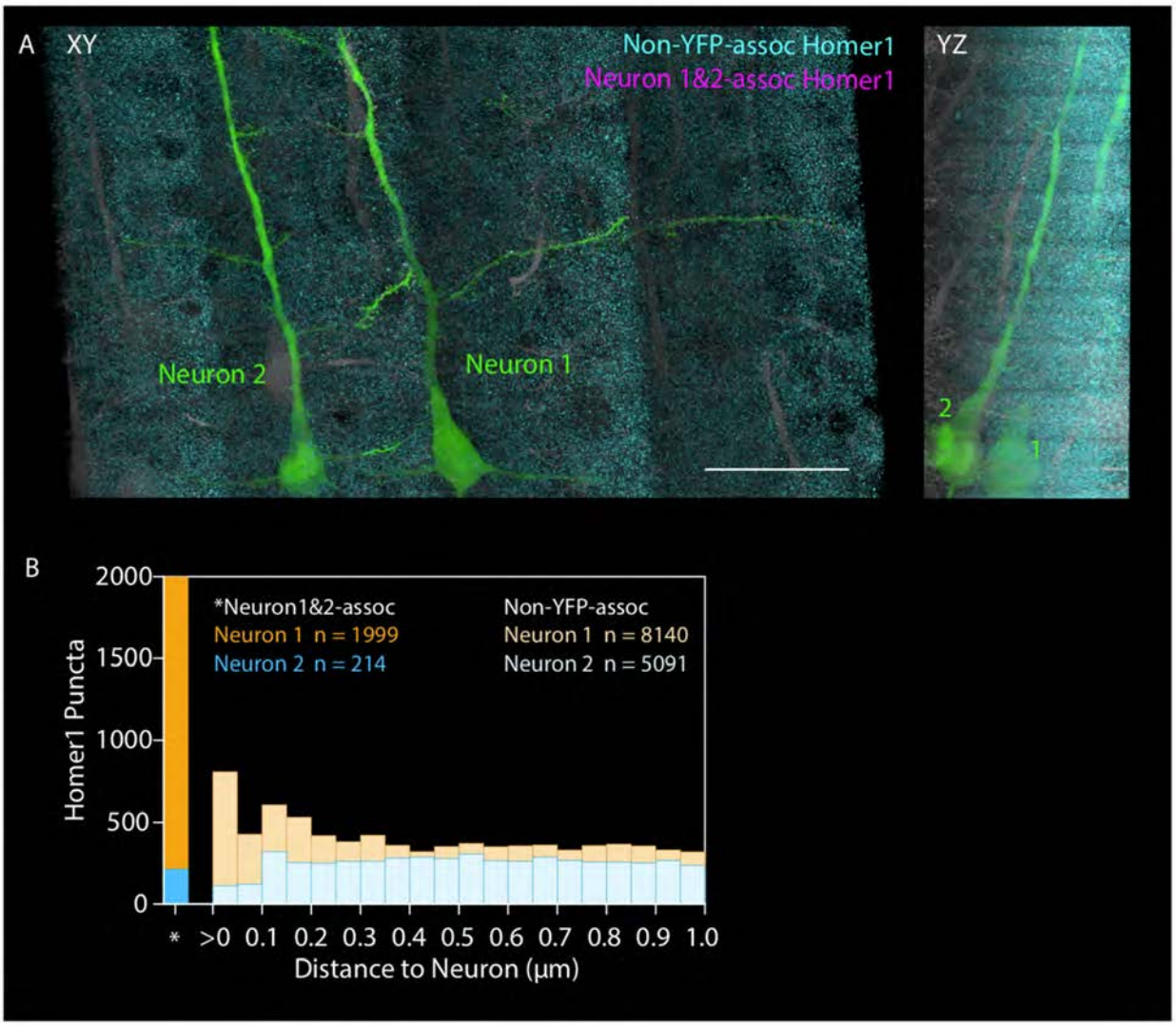

Fig. S17. Local density of neuron-associated and neuron-vicinity Homer1 puncta near the layer V pyramidal neurons shown in Fig. 3D in the mouse primary somatosensory cortex. (A) (Left) XY MIP of the layer V pyramidal neurons (Neuron 1 and 2) in Fig. 3D (green) in the mouse primary somatosensory cortex, and all the non-YFP-associated (cyan) and Neuron 1 and 2-associated Homer1 puncta (magenta) near the two neurons. All other YFP filled neurons are shown in dark grey. (Right) YZ MIP of the same region. Scale bars, 50 µm (for all panels). (B) Histogram showing the number of Neuron 1- (orange) and Neuron 2- (blue) associated Homer1 puncta and the number of non-YFP-associated Homer1 puncta at different distance from Neuron 1 (pale orange) and Neuron 2 (pale blue).

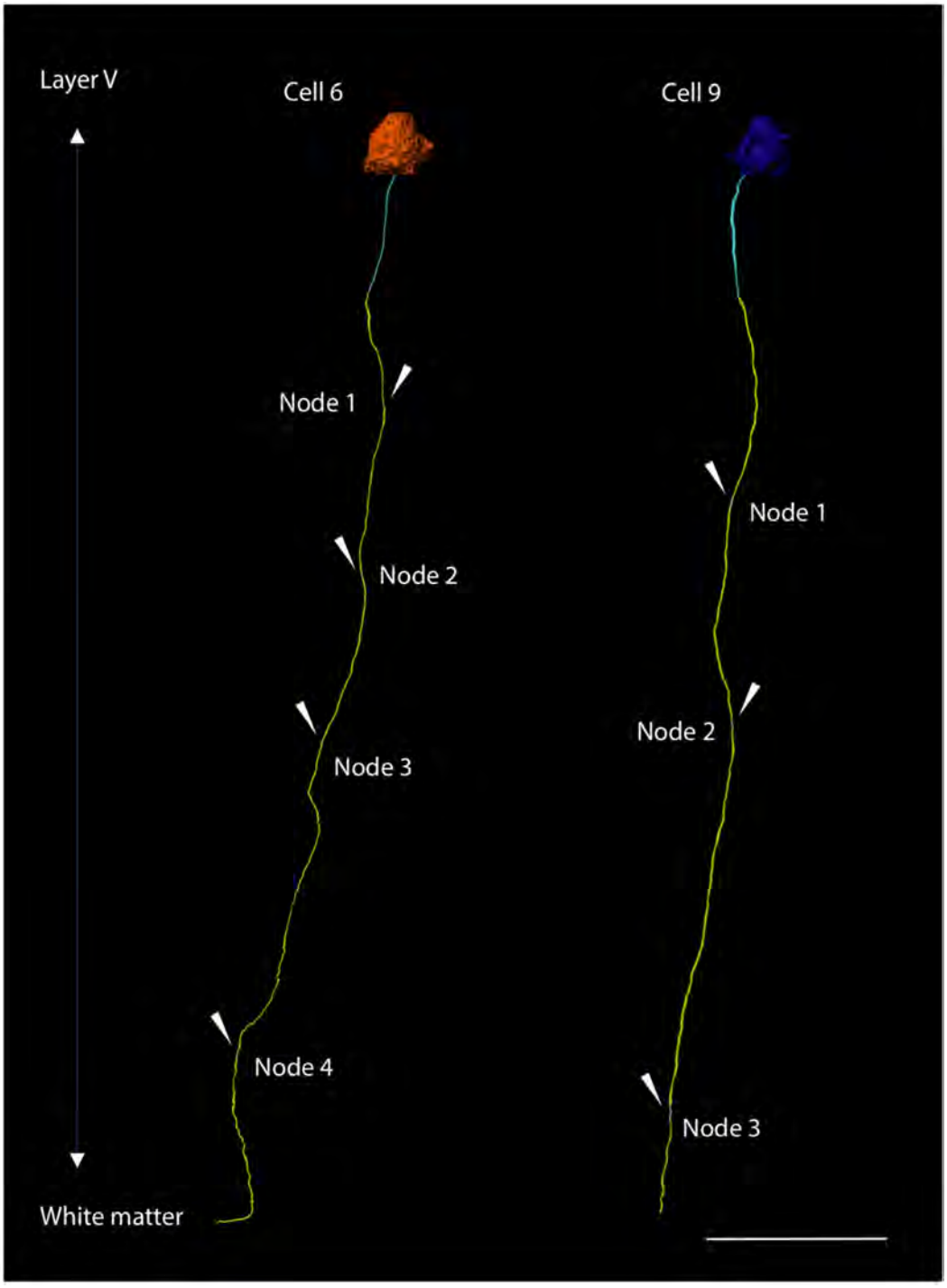

Fig. S18. Axon tracing and myelination pattern of two layer V pyramidal neurons in the mouse primary visual cortex. Reconstructed main axon tracts of two neurons (Cell 6 and Cell 9 from the left of Fig. 5B, top row) extending from layer V to the white matter, with arrows indicating the nodes of Ranvier. Note the increasing internodal distance with increasing distance from the soma. See also Fig. 5C. Scale bar, 50 μm.

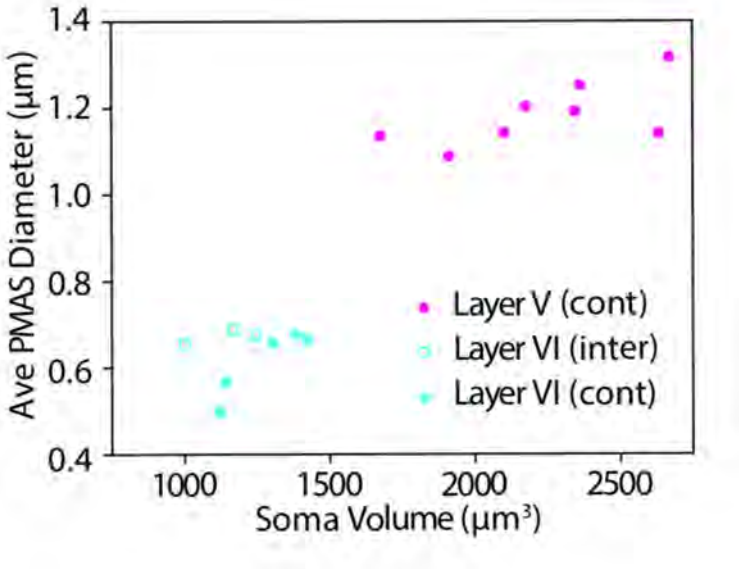

Fig. S19. Average pre-myelin axonal segment (PMAS) diameter and soma volume of the layer V and VI pyramidal neurons shown in Fig. 5B in the mouse primary visual cortex.

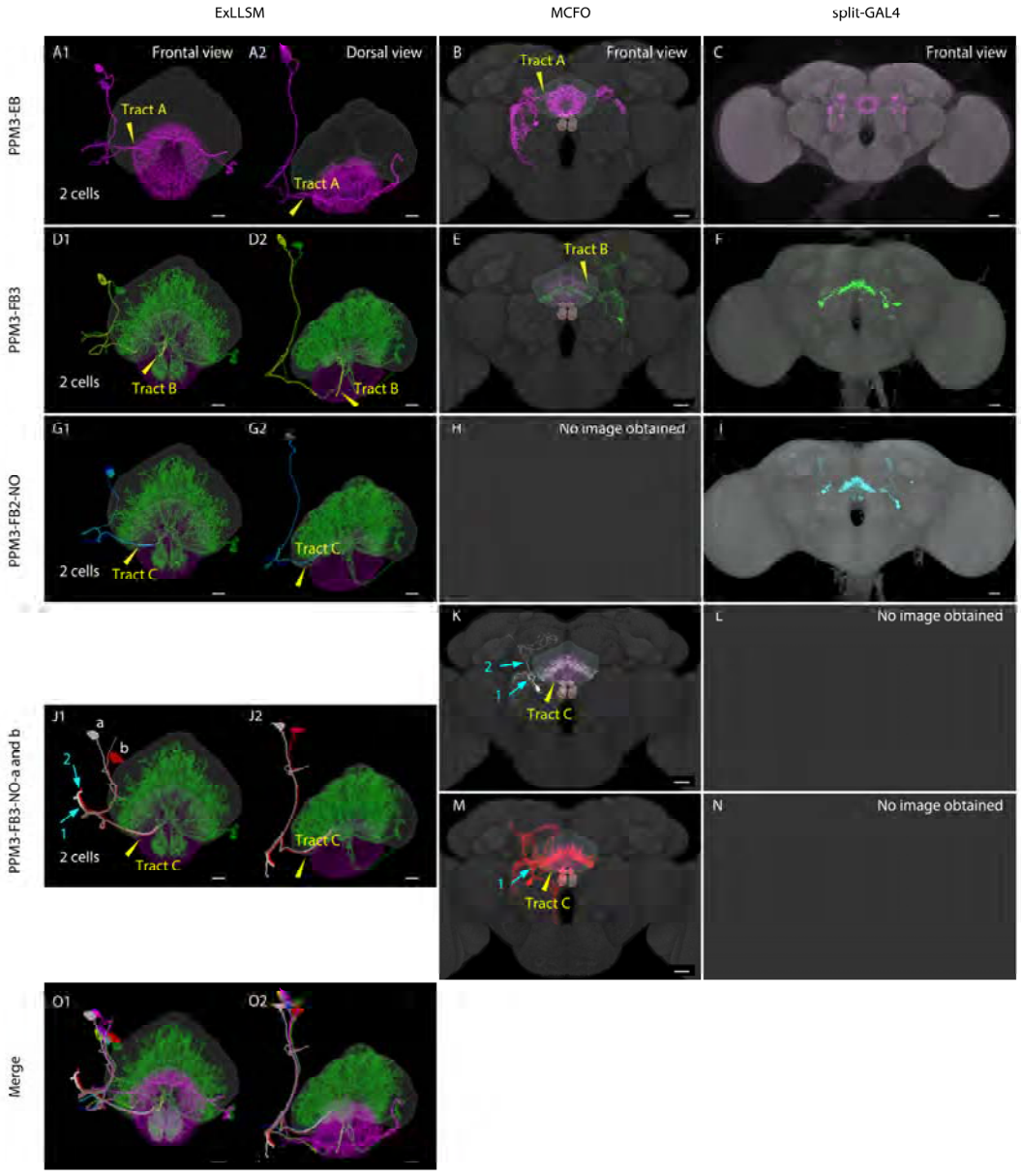

Fig. S20. Cell type classification of PPM3 cluster neurons in the adult *Drosophila* brain. (Left) Eight cells in the PPM3 cluster neurons were classified into five morphologically distinguishable cell types by tracing their primary neurites in ExLLSM data from the cell bodies to their target neuropils (two views at left). (Center) Multicolor flip-out (MCFO) images of TH-p65ADZp in attP40; DDC-ZpGAL4DBD in attP2 split-GAL4 driver were collected from 63 brain samples, registered to the standard brain JFRC2013, and segmented manually on Fluorender/VVDViewer. Representative images of each cell type are shown. (Right) Split-GAL4 drivers for subsets of PPM3 cluster neurons were designed based on the confocal image database of GAL4 driver lines. Images of successful intersections are displayed. See supplementary note 6f, table S5, and fig. S21 for morphological description of cell types and matching of cell type between ExLLSM, MCFO and split-GAL4 data. Scale bars, (ExLLSM) 10 μm and (MCFO and split-GAL4) 20 μm.

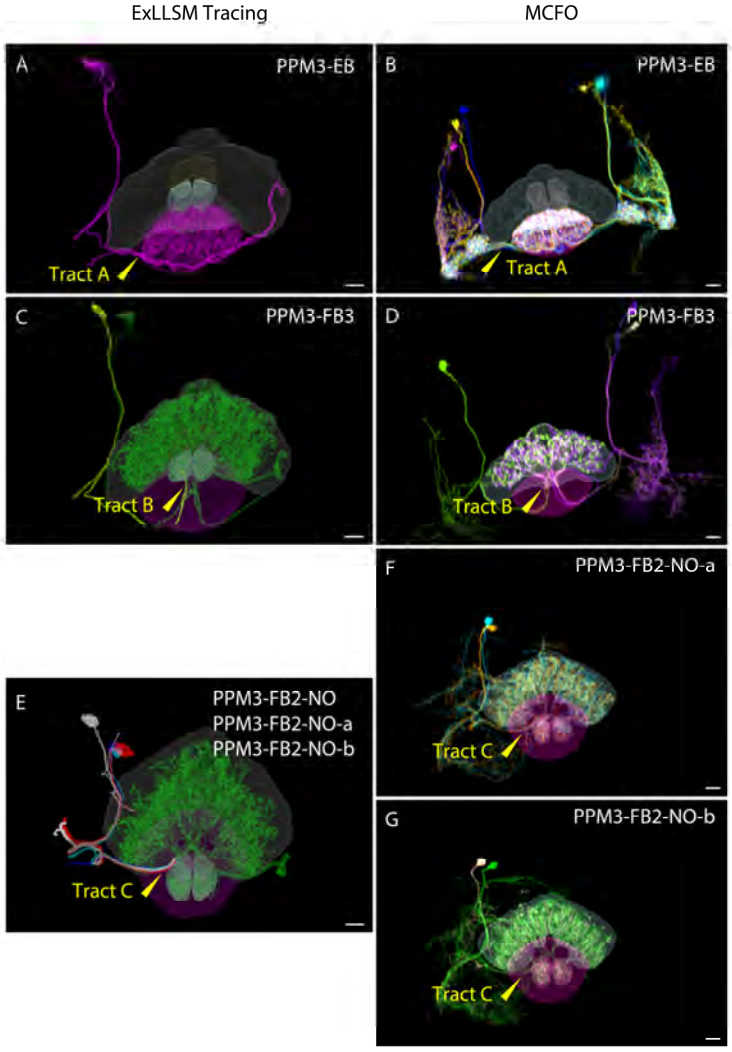

Fig. S21. Cell type identification of PPM3 cluster neurons by primary neurites. (Left) The primary neurites of PPM3 neurons were traced in the ExLLSM images and separately displayed with axonal arborizations in the target neuropils and outline of the ellipsoid body, fan-shaped body and noduli. (Right) Multiple examples of multicolor flip-out (MCFO) single cell images were collected for each cell type, and overplayed in the standard brain. Arrowheads indicate tracts to innervate the central complex. Scale bars, 10 μm.

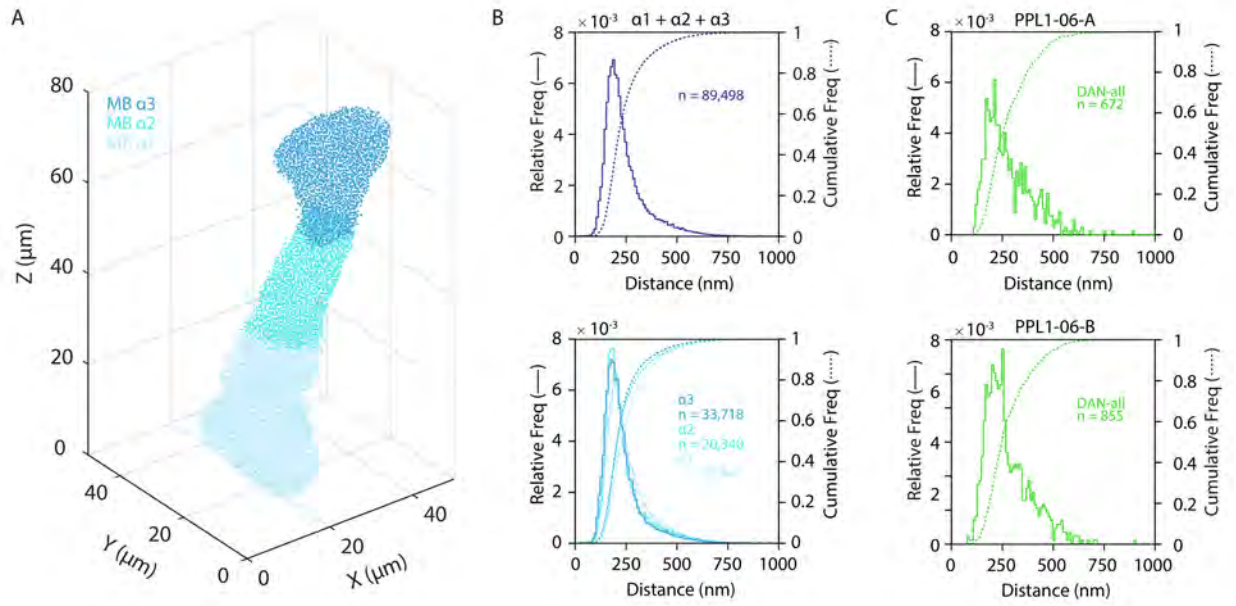

Fig. S22. Pre-synaptic densities in the *Drosophila* mushroom body (MB) α lobe from FIB-SEM tracing and reconstruction (*83*)**.** (A) 3D plot of all presynaptic densities in the MB α lobe. Color code indicates α3 (dark blue), α2 (blue), and α1 (pale blue) subregions. (B) Distribution of nearest-neighbor distances between presynaptic densities (top) across the α lobe and (bottom) in each of the α3, α2, α1 subregions. (C) Distance from (top) PPL1-06-A and (bottom) PPL1-06-B associated presynaptic densities to the nearest presynaptic density of any kinds in the MB α3.

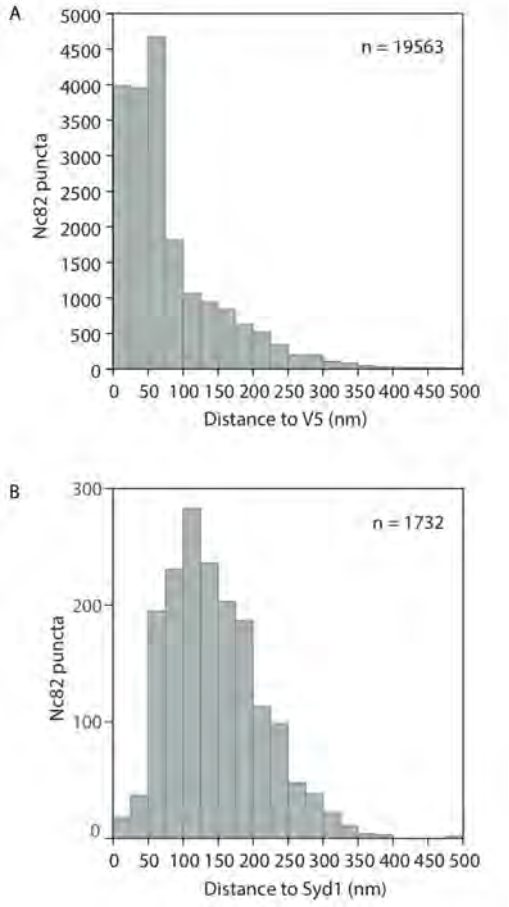

Fig. S23. Colocalization of presynaptic markers in ExLLSM images of adult *Drosophila* active zones (AZ). (A) Distance of each nc82 puncta to the nearest V5 puncta in the calyx (CA). (B) Distance of each nc82 puncta to the nearest Syd1 puncta on the surface of DC3 olfactory projection neuron (PN) boutons in the CA and lateral horn (LH).

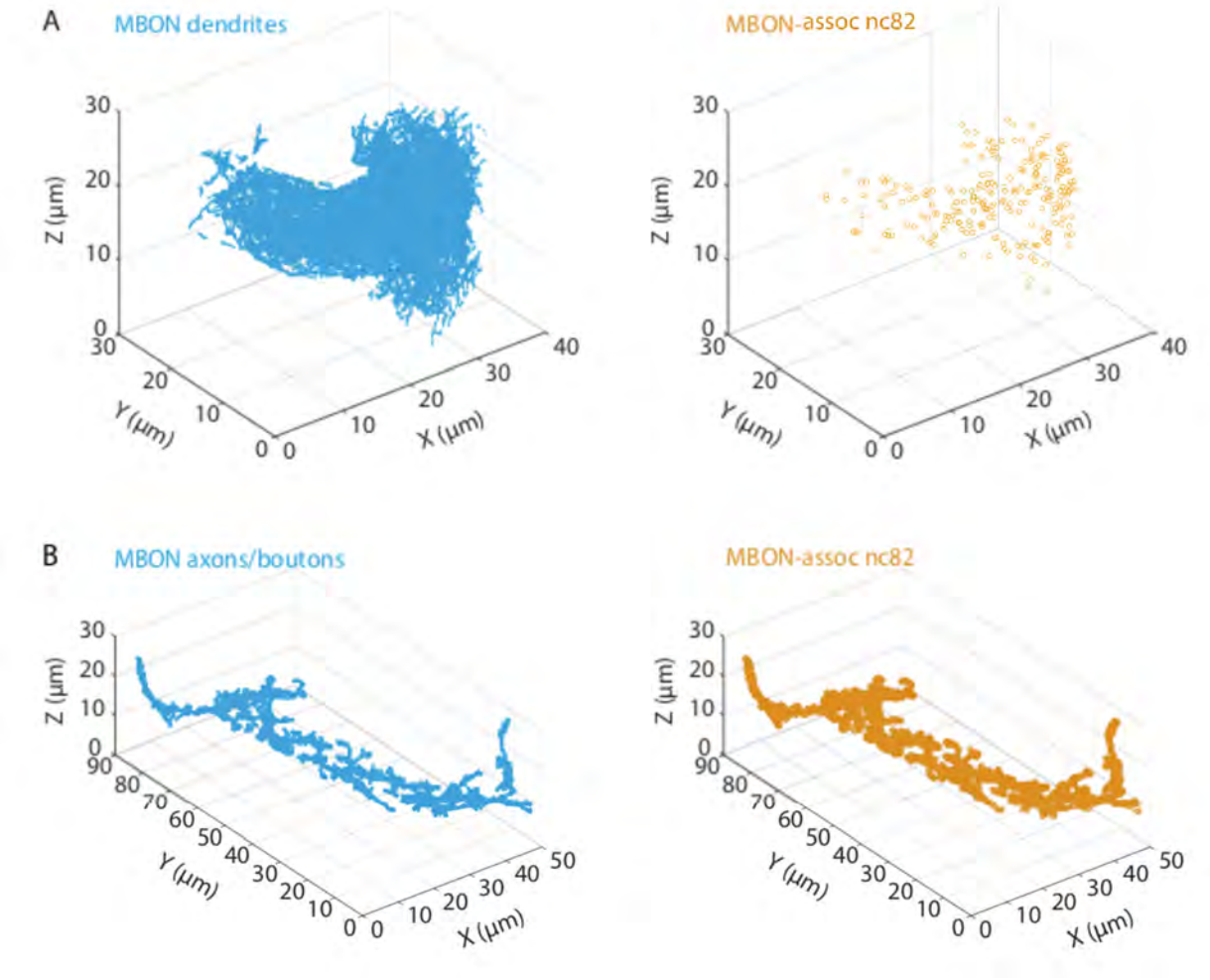

Fig. S24. Comparative surface densities of nc82 puncta on dendrites and axons/boutons of the mushroom body output neuron (MBON) in an adult *Drosophila*. (A) Segmented MBON dendrites (left, blue) and 3D point cloud plot of MBON-associated nc82 puncta in the same volume (right, orange). (B) Segmented MBON axons/boutons (left, blue) and 3D point cloud plot of MBON-associated nc82 puncta in the same volume (right, orange).

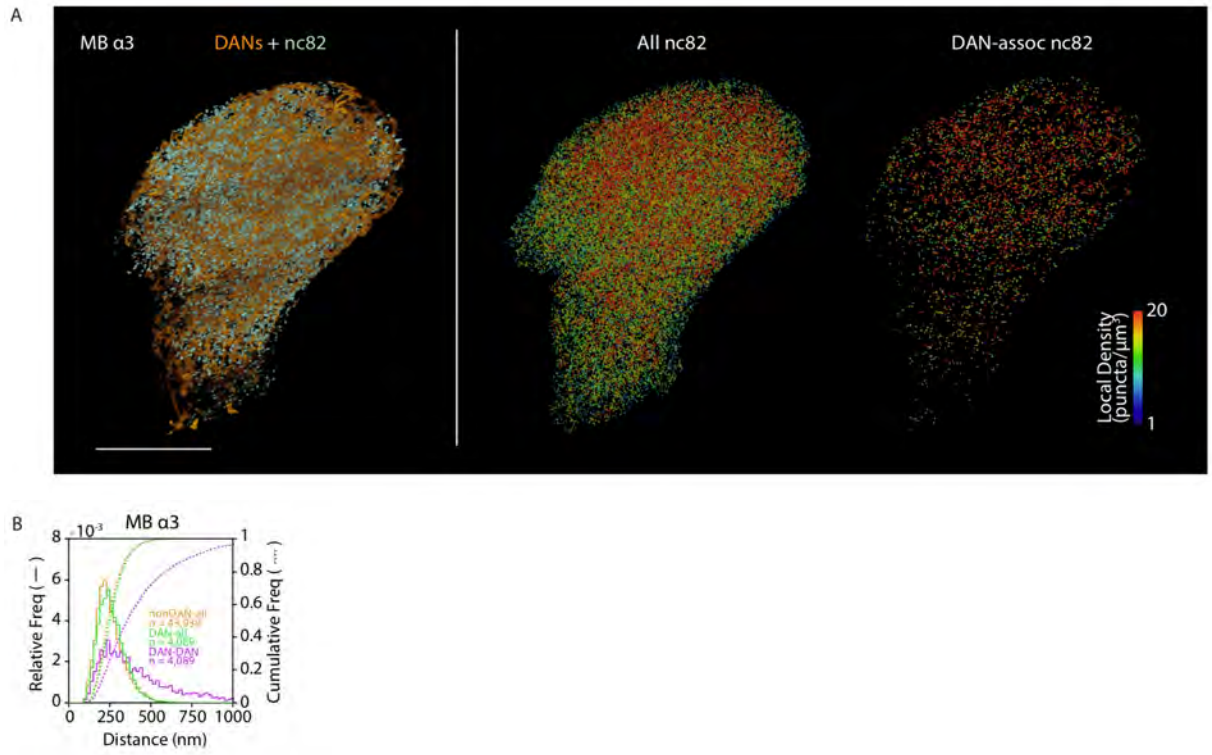

Fig. S25. Pre-synaptic sites and dopaminergic neurons in the α3 lobe of the adult *Drosophila* MB. (A) 3D rendered images of: (left) membranes of dopaminergic neurons (DANs, orange) and nc82 puncta (mint green); (center) density of all nc82; and (right) density of only those nc82 puncta associated with DANs. Nc82 puncta density was calculated from the number of nc82 puncta within a 1 μm radius from each punctum. Scale bar, 10 μm. (B) Distribution of distances from each DAN-associated (green) or non-DAN-associated (orange) nc82 punctum to the nearest nc82 punctum of any kind, and between nearest neighbor DAN-associated puncta (magenta).

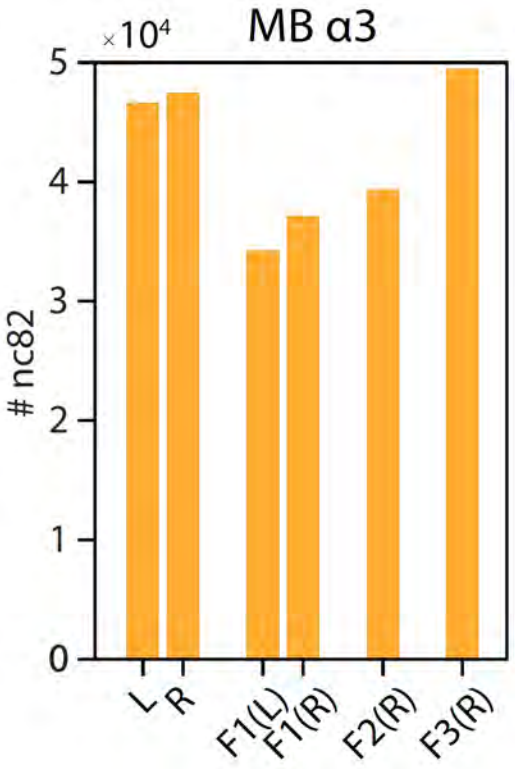

Fig. S26. Cross-animal comparison of the number of pre-synaptic sites in the α3 lobe of the adult *Drosophila* MB. The number of nc82 puncta from left (L) and right (R) MB α3 lobes of the whole brain dataset in figs. S25 to S30 (leftmost pair of bars) and four additional MB α3 lobes from three different female adults (*F1-F4*).

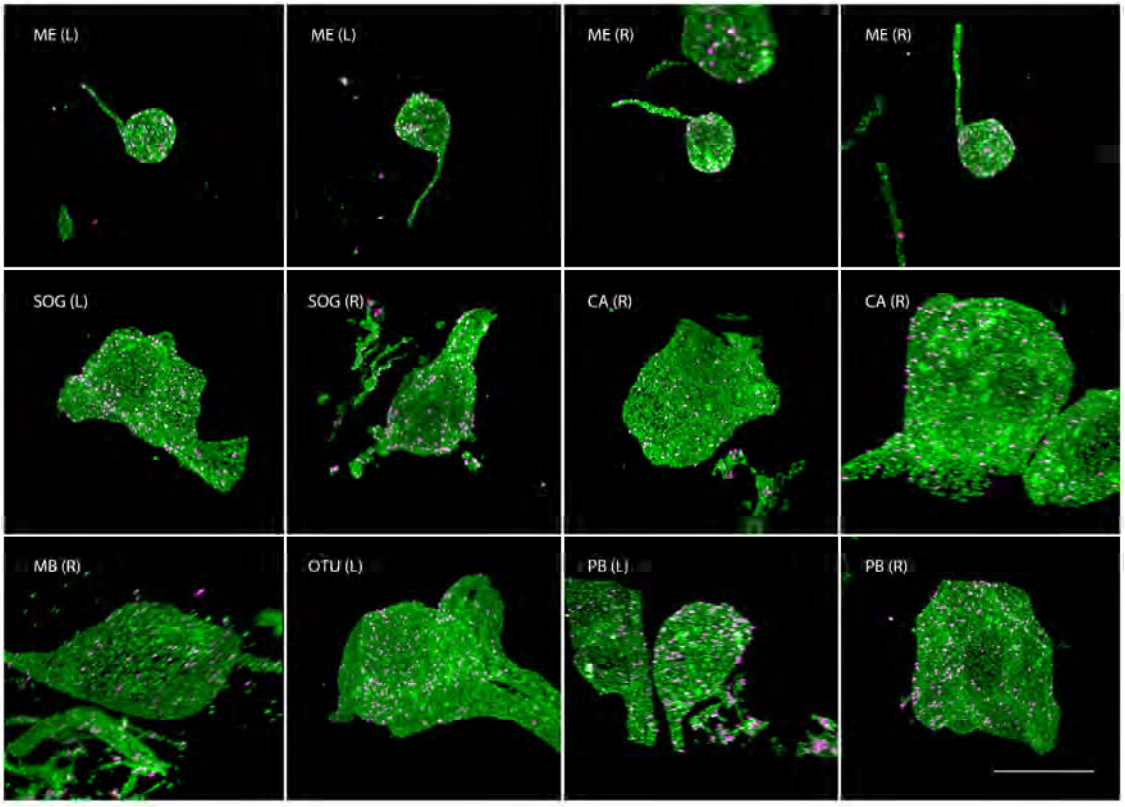

Fig. S27. Somata of DANs and DAN-associated nc82 puncta in distinctive brain regions of an adult *Drosophila*. DAN somata (green) and DAN-associated nc82 puncta (magenta) in proximity to specified brain regions are shown. Brain region abbreviations are given in Fig. 7. Scale bar, 5 μm.

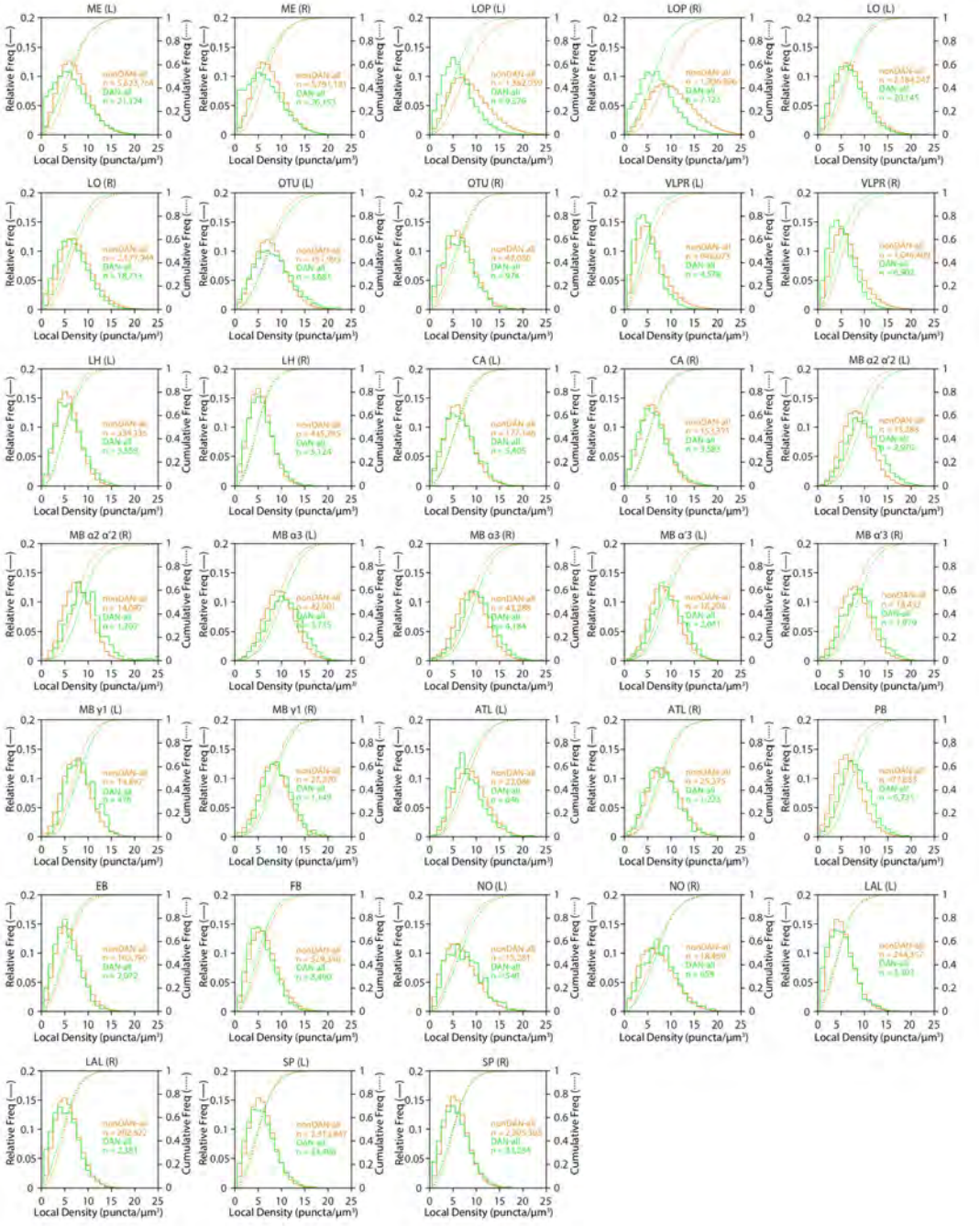

Fig. S28. Density of pre-synaptic sites across an adult *Drosophila* brain. Distributions of local density of nc82 puncta, either DAN-associated (green) or nonDAN-associated (orange), in 33 different brain regions. See also Fig. 7B.

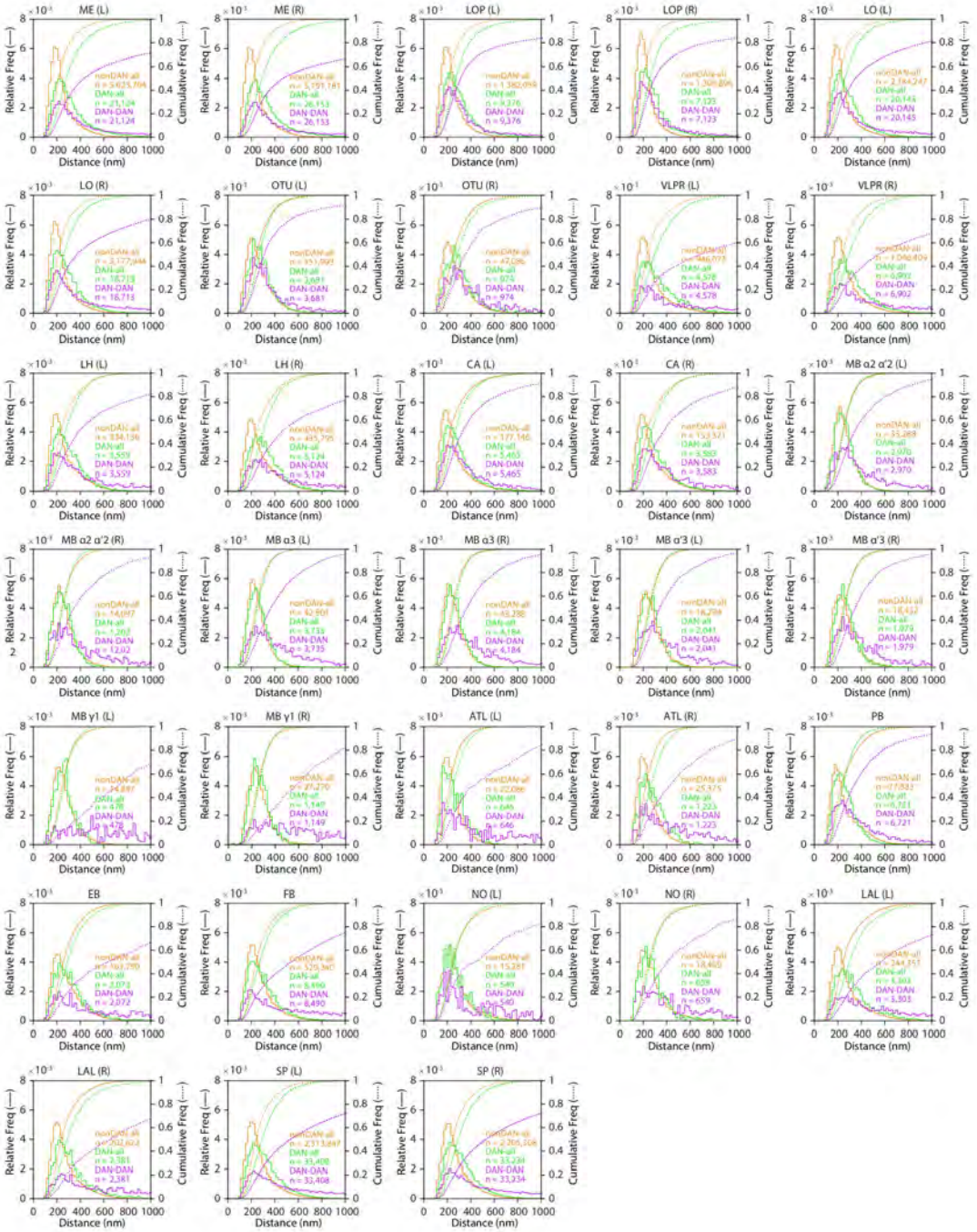

Fig. S29. Distances between pre-synaptic sites across an adult *Drosophila* brain. Distributions of distances from each DAN-associated (green) or non-DAN-associated (orange) nc82 punctum to the nearest nc82 punctum of any kind, and between nearest neighbor DAN-associated nc82 puncta (magenta), in 33 different brain regions. See also Fig. 7C.

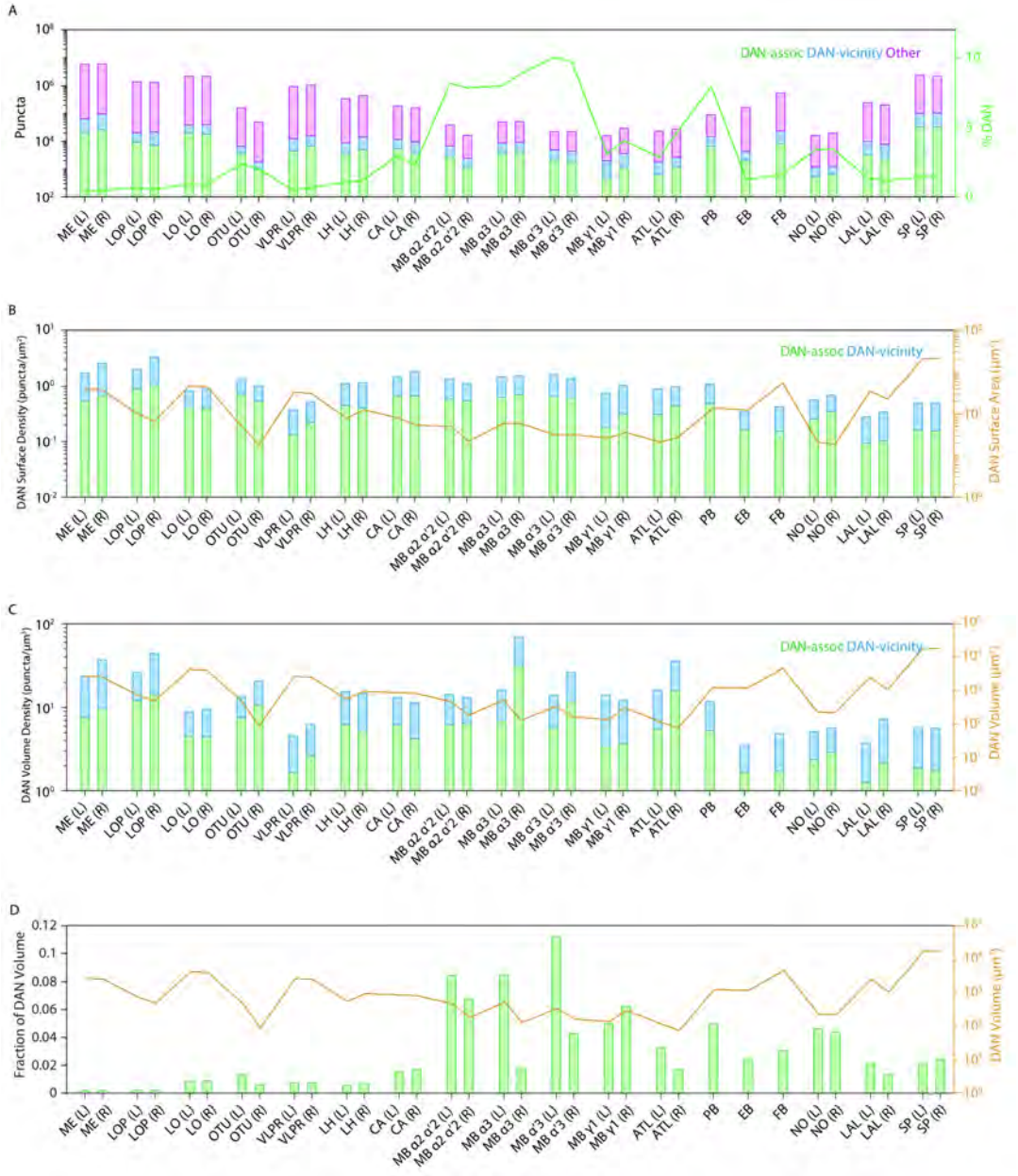

Fig. S30. Statistics of DANs and pre-synaptic sites across an adult *Drosophila* brain. (A) Number of DAN-associated nc82 puncta (green bars), DAN-vicinity nc82 puncta (blue bars) and all other nc82 puncta (purple bars), and the percentage of all nc82 puncta that are DAN-associated (green curve) in 33 different brain regions in adult *Drosophila*. (B) Density of DAN-vicinity nc82 puncta (blue bars) and DAN-associated nc82 puncta (green bars) per unit of DAN surface area, and the total DAN surface area (orange curve) in 33 different brain regions. (C) Density of DAN-vicinity nc82 puncta (blue bars) and DAN-associated nc82 puncta (green bars) per unit of DAN volume, and the total DAN volume (orange curve) in 33 different brain regions. (D) Fraction of DAN volume to the total brain region volume (green bars), and the total DAN volume (orange curve) in 33 different brain regions. Brain region abbreviations are given in Fig. 7. See also Fig. 7D.

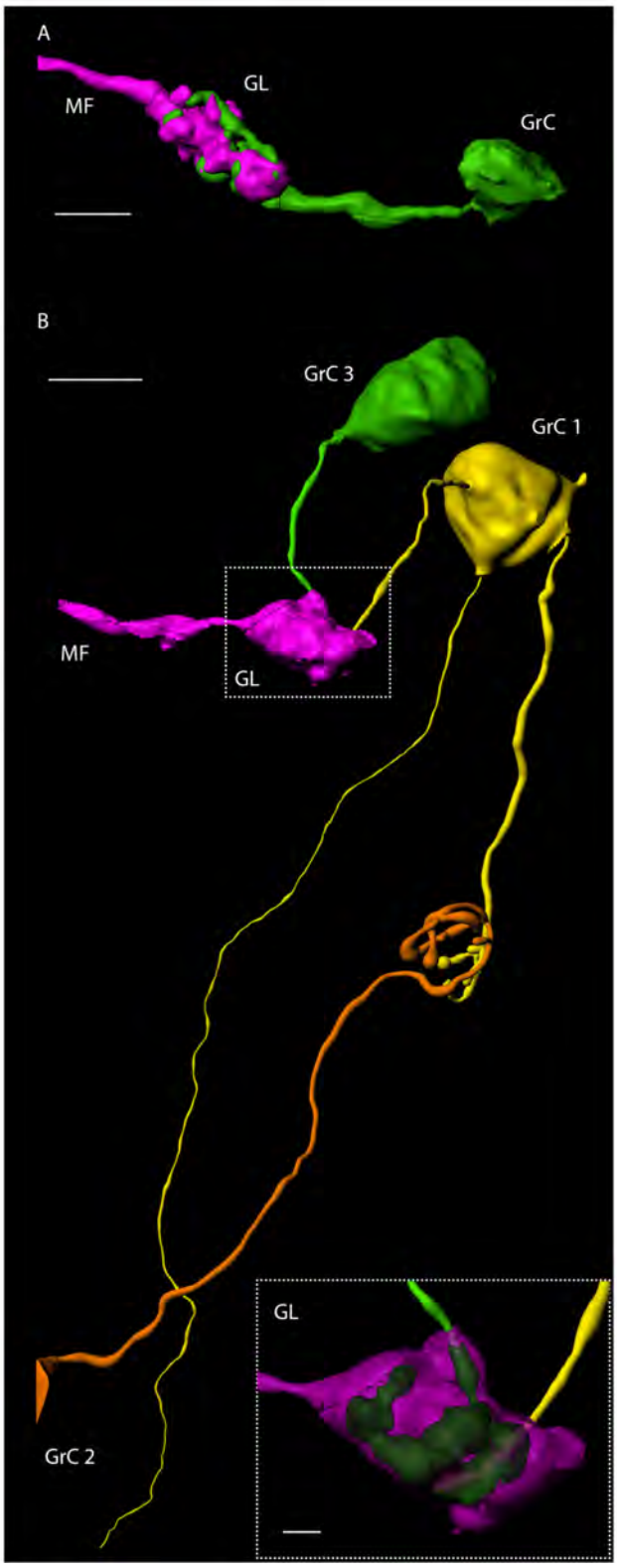

Fig. S31. Reconstruction of mouse cerebellar glomerulus and granule cells. (A) Reconstructed mouse cerebellar glomerulus (GL) formed between a pontine mossy fiber (magenta, MF) and a granule cell (green, GrC). MFs were retrogradely labeled by modified rabies virus (mCherry) and GrCs endogenously expressed mCitrine. Scale bar, 5 μm. (B) Reconstructed mouse pontine mossy fiber (magenta, MF), granule cells labeled by low-level anterograde infection with the modified rabies virus (yellow, GrC 1; orange, GrC 2), and a granule cell without such anterograde infection (green, GrC 3). Scale bar, 5 μm (20.5 μm). Inset, magnified view of the cerebellar GL formed between MF, GrC 1 and GrC 3. Scale bar, 1 μm.

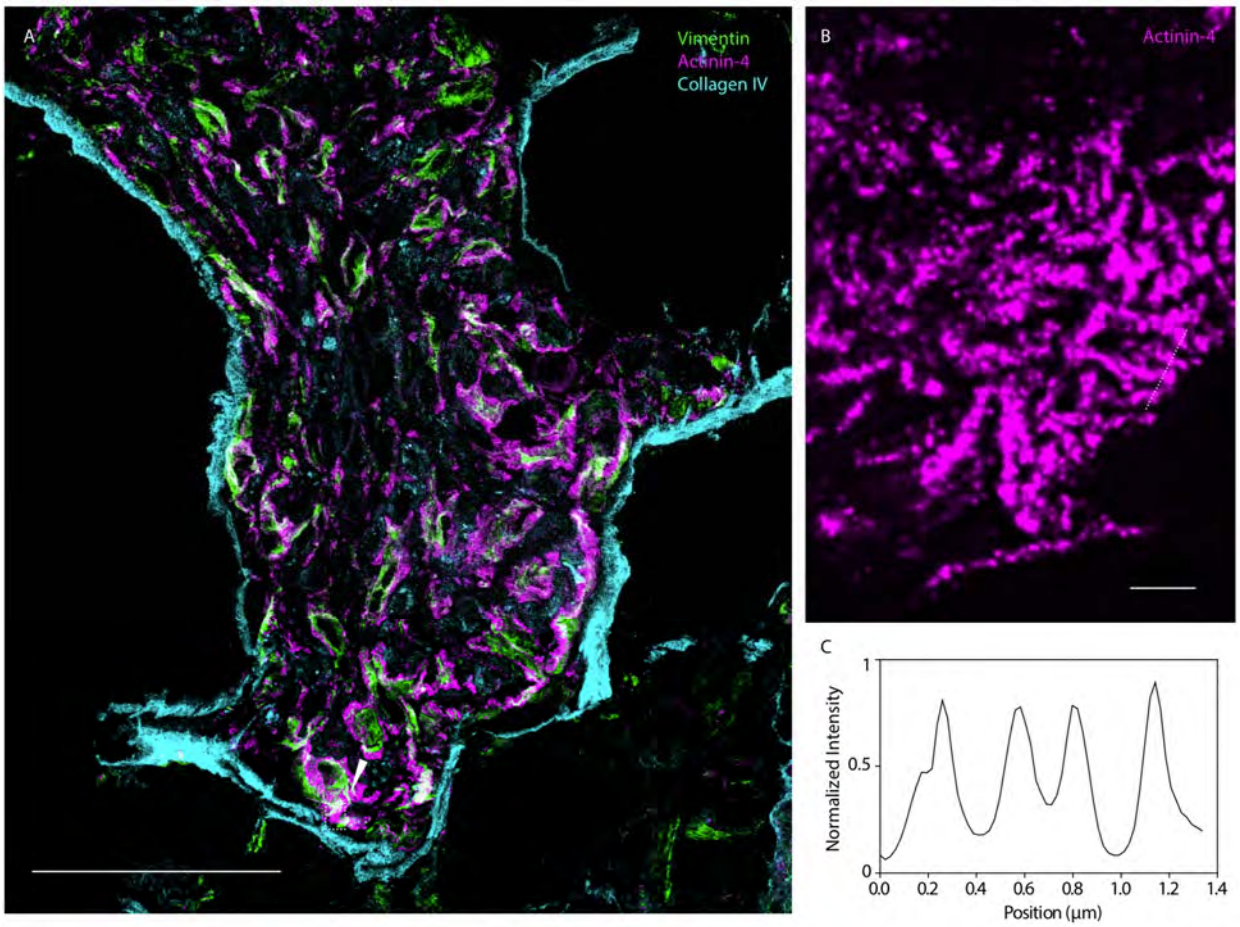

Fig. S32. Human renal glomerulus. (A) MIP view of a ~5μm thick human kidney glomerulus section immunostained against vimentin (green), actinin-4 (magenta), and collagen IV (cyan). Scale bar, 50 μm. (B) Magnified view of the actinin-4 channel in the boxed region at the bottom of A, denoted with arrow. Scale bar, 1 μm. (C) Normalized fluorescence intensity of the actinin-4 channel along the line in B.

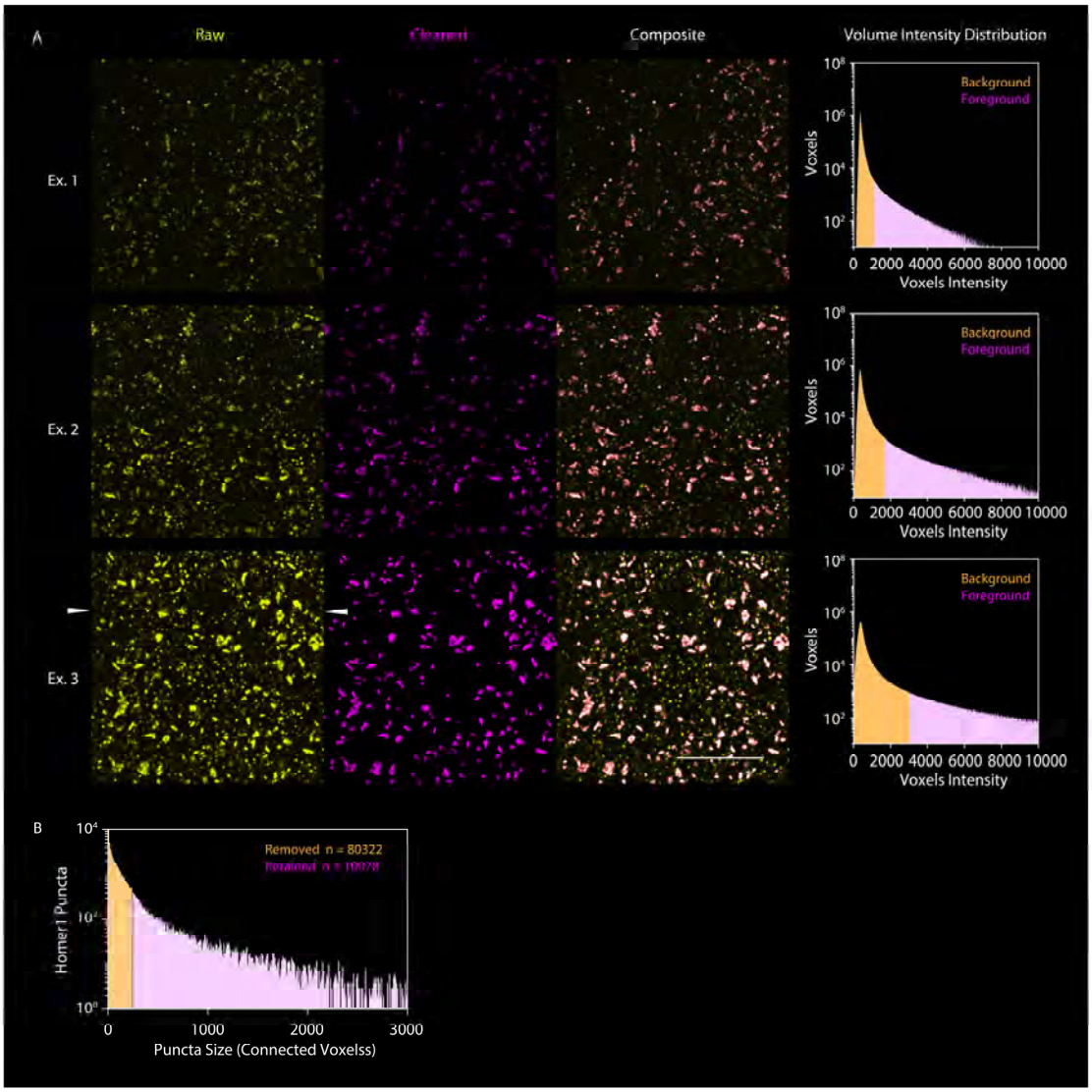

Fig. S33. Filtering of non-specific antibody signals. (A) MIP views of ~2.5 µm thick slabs from three different regions (Ex. 1-3) of the primary somatosensory cortex of a Thy1-YFP mouse shown in Fig. 3, showing the raw Homer1 channel (yellow), the filtered Homer1 channel (magenta), the composite of both the raw and filtered channels, and the voxel intensity distribution in the same volume. To differentiate the foreground (magenta in the histogram) from the background (orange in the histogram), a dynamic Otsu threshold was applied in order to account for the fluorescence intensity difference at different regions of the dataset. Scale bar, 5 µm. The arrows in Ex. 3 indicate a stitching boundary. (B) Histogram showing the number of Homer1 puncta removed (orange) and retained (magenta) after the filtering (size filter = 246 voxels), for ~ 90,000 puncta from five regions of 500^3 voxels each across the cortical section shown in Fig. 3.

Supplementary Table

Table S1. Comparison of volumetric nanoscale imaging methods for brain tissues.

Imaging Method	References	Reported Total Imaged Volume (mm^3)	Reported Total Imaging Time	Imaging Time per 1 mm^3 (/mm^3·color)	Volume Speed (μm^3/sec·color) *(normalized to the ExLLSM (SS) volume speed)*	Voxel Volume (dx, dy, dz) (nm^3) (*normalized to ExLLSM (SS) voxel volume*)	Voxel Speed (voxels/sec·color) (*normalized to the ExLLSM (SS) voxel speed*)
FIB-SEM	(*4*)	0.18 x 0.1 x 0.05	100 days	2.67 x 10^6 hours = 304.4 years	0.104 *(1/22400)*	8 x 8 x 8 *(0.0150)*	2.03 x 10^5 *(1/337)*
ssTEM	(*5*)	~0.08	~16 months	0.144 x 10^6 hours = 16.7 years	1.92 *(1/1210)*	4 x 4 x (35-40) *(0.0164)*	3.44 x 10^6 *(1/19.9)* (35 nm z-sections) (net camera pixel rate: 5.0 x 10^7 pixels/sec)
Automatic tape-collecting ultramicrotome (ATUM) + single-beam SEM	(*33*)	0.04 x 0.04 x 0.05	~82 hours (net camera frame rate)	1.03 x 10^6 hours = 117 years	0.27 *(1/8630)*	3 x 3 x 30 *(0.00793)*	1.0 x 10^6 *(1/68.5)*
		~0.5 x 1.0 x 0.0074 (mid-resolution dataset)	~38 hours (net camera frame rate)	1.03 x 10^4 hours = 1.17 years	27 *(1/86.3)*	30 x 30 x 30 *(0.793)*	1.0 x 10^6 *(1/68.5)*
Large scale array tomography (LSAT)	(*7*)	1.0 x 0.83 x 0.21 (three colors)	~877.5 hours	1.68 x 10^3 hours = 70 days (fluorescence imaging only)	165 *(1/14.1)*	65 x 65 x 200 *(24.7)* (dx/dy estimated from Zeiss Axio Observer Microscope with 100x objective)	1.96 x 10^5 *(1/350)*
3D-STED	(*22*)	~0.60 x 0.60 mm^2 FOV (Fig. S2E)	Pixel dwell time = 10-20 µs	8.33 x 10^4 hours = 9.51 years (assuming 15 µs dwell time and no time spent between the z-steps)	3.33 *(1/700)*	20 x 20 x 125 *(1.46)* (Fig. S7A z-step)	6.67 x 10^4 *(1/1030)* (assuming 15 µs dwell time and no time spent between the z-steps)
PALM/STORM	(*131*)	~0.08 x 0.08 mm^2 FOV generated from ~80000 frames	~3.7 hours/FOV	5.78 x 10^5 hours = 65 years (assuming 1 µm z-step)	0.480 *(1/4850)*	9 x 9 x 19 *(0.0452)* (estimated from the localization precisions (FWHM))	3.12 x 10^5 *(1/219)* (assuming 1 µm z-step)

Table S1 Cont'd. Comparison of volumetric nanoscale imaging methods for brain tissues.

Imaging Method	References	Reported Total Imaged Volume (mm^3)	Reported Total Imaging Time	Imaging Time per 1 mm^3 ($/mm^3 \cdot color$)	Volume Speed ($\mu m^3/sec \cdot color$) *(normalized to the ExLLSM (SS) volume speed)*	Voxel Volume (dx, dy, dz) (nm^3) (*normalized to ExLLSM (SS) voxel volume*)	Voxel Speed (voxels/sec·color) (*normalized to the ExLLSM (SS) voxel speed*)
PALM/STORM Cont'd	(*47*)	0.03 x 0.03 x 0.00065 (three colors)	2 min (several minutes)	1.90×10^4 hours = 2.17 years (net imaging time)	14.6 *(1/160)*	14 x 14 x 35 *(0.201)* (estimated from the localization precisions (SD))	2.13×10^6 *(1/32.1)* (voxel volume estimated from the localization precisions (SD))
iSIM	(*132*)	~0.09 x 0.08 mm^2 FOV (1745 x 1500 pixels) (one color)	50 ms/FOV (assuming 10 ms z-step)	38.6 hours	10223 *(3.08)*	56.0 x 56.0 x 50.0 *(4.59)*	5.24×10^7 *(1/1.31)*
Super-resolution spinning disk	(*133*)	~0.06 x 0.05 mm^2 FOV for full sCMOS chip (2560 x 2160 pixels) (one color)	210 ms/FOV for fluorescent beads (assuming 10 ms z-step)	150 hours = 6.2 days	1964 *(1/1.26)*	23.4 x 23.4 x 130 (assuming 130 nm z-step at 1.4 NA) *(2.08)*	2.63×10^7 *(1/2.61)*
ExLLSM (SS)	Fig. 1	~0.25 x 0.25 x 0.14 (expansion factor = 3.95x) (two colors)	130 min	119 hours = 5.0 days	2330 *(1)*	31.1 x 26.3 x 41.8 (after deskewing/rotation) *(1)*	6.84×10^7 *(1)*
ExLLSM (OS)	fig. S4	~0.10 x 0.10 x 0.14 (expansion factor = 3.95x) (two colors)	175 min	1001 hours = 41.7 days	277 (*1/8.40*)	24.6 x 24.6 x 45.6 *(0.807)*	1.00×10^7 *(1/6.85)*
ExM + spinning disk	Fig. 1	~0.14 x 0.14 x 0.11 (expansion factor = 3.95x) (two colors)	237 min	815 hours = 34 days	340 (*1/6.85*)	40.5 x 40.5 x 63.3 *(3.04)*	3.27×10^6 *(1/20.9)*
ExM + Airyscan (Fast mode)	Fig. 1	~0.076 x 0.076 x 0.105 (expansion factor = 3.95x) (two colors)	441 min	4813 hours = 201 days	57.5 *(1/40.5)*	13.1 x 13.1 x 68.4 *(0.342)*	4.36×10^6 *(1/15.7)*

Table S2. Sample preparation, imaging, and image processing conditions for all experiments.

Sample #	Figure #	Sample Name	Sample Preparation				Imaging Conditions *(post-expansion (as imaged) size)*							Image Preprocessing		Image Analysis & Visualization
			Genotype	Fluorescent proteins and target proteins/epitopes for immunostaining	Antibodies	ExM expansion factor	Imaging mode	Voxel volume (dx, dy, dz) (nm^3)	Voxels per tile (x, y, z)	Imaged volume (μm^3)	Color channels (exposure time per frame)	Power	Total imaging time in hours	Stitching conditions (# of starting tiles)	Stitching results	Corrections: linear unmixing; gamma; additional flat-field
1	Fig.1; figs. S2 to S4	**Mouse (Thy1-YFP) primary somatosensory cortex with Tom20 immunostaining**	Thy1-YFP-H	YFP	NA	3.95	Sample scan	26.3 x 26.3 x 86.1 *(104 x 104 x 340)* (dz in the scanning direction); 31.1 x 26.3 x 41.8 *(122.9 x 104 x 165.2)* (after deskewing /rotation)	360 x 1600 x 3236 (z in the scanning direction)	~250 x 250 x 140 *(~1000 x 1000 x 560)*	488 (3 ms) 560 (3 ms)	45% 35%	2.17 (130 min)	No iterative rematching (278 tiles x 2 colors)	Performed 1 iteration Retained 278 tiles Transfer error: avg = 0.91 px, max = 3.74 px	No; Yes; Yes (only for Fig. 1B)
							Objective scan	24.6 x 24.6 x 45.6 *(97 x 97 x 180)*	360 x 704 x 501	~100 x 100 x 140 *(~400 x 400 x 560)*	488 (7 ms) 560 (7 ms)	60% 45%	2.91 (175 min)	No iterative rematching (960 tiles x 2 colors)	Performed 1 iteration Retained 949 tiles Transfer error: avg = 1.61 px, max = 4.93 px	Yes; No; No
				Tom20	Primary: rabbit polyclonal (Santa Cruz Biotech, sc-11415) Secondary: goat anti-rabbit Alexa Fluor 546 (ThermoFisher, A-11035)		Spinning disk confocal	40.5 x 40.5 x 63.3 *(160 x 160 x 250)*	3584 x 3584 x 1816 (stitched and saved as one tile on the run)	~550 x 550 x 440 *(~140 x 140 x 110)*	488 (200 ms) 561 (200 ms)	20% 30%	3.95 (237 min)	Default stitching using NIS-Elements Viewer (Nikon) (4 tiles x 2 colors)	Retained 4 tiles	Yes; Yes; Yes (only for Fig. 1B)
							Airyscan Fast mode	13.1 x 13.1 x 68.4 *(51.7 x 51.7 x 270)*	2044 x 2044 x 1645 (9 tiles in total)	~76 x 76 x 105 *(~300 x 300 x 415)*	488 561 dwell time: 0.54 µs/px	1.1% (561)	7.35 (441 min)	MIP-stitching using Grid/Collection stitching plug-in of ImageJ (9 tiles x 2 colors)	Retained 9 tiles	Yes; Yes; Yes (only for Fig. 1B)
2	Fig. 2, A to E; fig. S8; Movie 1; movie S1	**Mouse (Thy1-YFP) somatosensory cortex with Tom20 and LAMP1 immunostaining**	Thy1-YFP-H	YFP	NA	3.95	Objective scan	24.6 x 24.6 x 45.6 *(97 x 97 x 180)*	284 x 544 x 501	~100 x 150 x 150 *(~400 x 600 x 600)*	488 (7 ms) 560 (7 ms) 642 (7 ms)	55% 30% 30%	9.58 (575 min)	Rematching mode: incremental Fusion mode: blending (2296 tiles x 3 colors)	Performed 1 iteration Retained 2296 tiles Transfer error: avg = 0.78 px, max = 2.88 px	No; No; No
				Tom20	Primary: rabbit polyclonal (Santa Cruz Biotech, sc-11415) Secondary: goat anti-rabbit Alexa Fluor 546 (ThermoFisher, A-11035)											
				LAMP1	Primary: rabbit polyclonal (Abcam, ab24170) Secondary: goat anti-rabbit Atto 647N (ThermoFisher, 40839-1ML-F)											

Table S2 Cont'd. Sample preparation, imaging, and image processing conditions for all experiments.

Sample #	Figure #	Sample name	Genotype	Fluorescent proteins and target proteins/epitopes for immunostaining	Antibodies	ExM expansion factor	Imaging mode	Voxel volume (dx, dy, dz) (nm^3)	Voxels per tile (x, y, z)	Imaged volume (μm^3)	Color channels (exposure time per frame)	Power	Total imaging time (hours)	Stitching conditions (# of starting tiles)	Stitching results	Corrections: linear unmixing; gamma; additional flat-field
3	Fig. 2, F to H; figs. S9 and S10; Movie 2	**Mouse (Thy1-YFP) primary somatosensory cortex with MBP immunostaining**	Thy1-YFP-H	YFP	NA	3.95	Objective scan (two camera set-up)	24.6 x 24.6 x 38.0 *(97 x 97 x 150)*	320 x 640 x 534	~320 x 280 x 60 *(~1500 x 1100 x 240)*	488 (3 ms) 560 (3 ms)	30% 30%	5.85 (351 min)	Custom pipeline setup with independent channel stitching and subsequent channel alignment (2478 tiles x 2 colors)	Retained 1898 tiles Transfer error: avg (488 channel) = 1.54 px, max (488 channel) = 4.54 px; avg (560 channel) = 1.40 px, max (560 channel) = 3.87 px	No; Yes (only for Fig. 2F); No
				Myelin basic protein (MBP)	Primary: rabbit polyclonal (Abcam, ab40390) Secondary: goat anti-rabbit Alexa Fluor 568 (ThermoFisher, A-11011)											
4	Fig. 2, I to K; fig. S12; Movie 3	**Mouse (Thy1-YFP) primary somatosensory cortex with Bassoon and Homer1 immunostaining**	Thy1-YFP-H	YFP	NA	4.04	Objective scan	24.0 x 24.0 x 61.9 *(97 x 97 x 250)*	360 x 704 x 301	~75 x 100 x 125 *(~300 x 400 x 500)* (triangular prism filling about half of the volume)	488 (10 ms) 560 (10 ms) 642 (15 ms)	30% 40% 100%	0.62 (37 min)	Rematching mode: incremental Fusion mode: blending (162 tiles x 3 colors)	Performed 3 iterations Retained 162 tiles Transfer error: avg = 2.42 px, max = 10.80 px	No; Yes (only for Fig. 2I); No
				Homer1	Primary: rabbit polyclonal (Synaptic Systems, 160 003) Secondary: goat anti-rabbit Alexa Fluor 546 (ThermoFisher, A-11035)											
				Bassoon	Primary: mouse monoclonal (Abcam, ab82958) Secondary: donkey anti-mouse CF 633 (Biotium, 20124)											
5	fig. S31; movie S5	**Mouse (Slc17a7-cre X TCGO) cerebellum**	Slc17a7-cre X TCGO	mCitrine (cytosolic granule cells)	NA	4.1	Objective scan	23.7 x 23.7 x 36.6 *(97 x 97 x 150)*	320 x 640 x 534	~100 x 120 x 150 *(~400 x 500 x 600)*	488 (3 ms) 560 (3 ms)	50% 100%	2.22 (133 min)	Custom pipeline setup with limited search radius (1160 tiles x 2 colors)	Retained 1068 tiles Transfer error: avg = 2.04 px, max = 8.93 px	No; No; No
				mCherry (selective retrograde labeling of basal pontine nucleus (BPN) mossy fiber projections and a sparse subset of granule cells and Golgi cells with modified rabies virus)	NA											
6	fig. S32	**Human kidney (US BioMAX, HuFTS241) with vimentin, Actinin-4, and Collagen IV immunostaining**	NA	Vimentin	Primary: chicken polyclonal (Abcam, ab24525) Secondary: goat anti-chicken Alexa Fluor 488 (ThermoFisher, A-11039)	4.5	Objective scan	21.6 x 21.6 x 40 *(97 x 97 x 180)*	360 x 704 x 501	~220 x 220 x 22 *(~1000 x 1000 x 100)*	488 (10 ms) 560 (10 ms) 642 (10 ms)	20% 40% 80%	9.33 (560 min)	Rematching mode: incremental Manually adjusted stage (1632 tiles x 3 colors)	Performed 15 iterations Retained 770 tiles Transfer error: avg = 2.71 px, max = 18.46 px	No; Yes; No
				Actinin-4	Primary: rabbit polyclonal (Sigma Aldrich, HPA001873) Secondary: goat anti-rabbit Alexa Fluor 546 (ThermoFisher, A-11035)											

Table S2 Cont'd. Sample preparation, imaging, and image processing conditions for all experiments.

Sample #	Figure #	Sample name	Genotype	Fluorescent proteins and target proteins/epitopes for immunostaining	Antibodies	ExM expansion factor	Imaging mode	Voxel volume (dx, dy, dz) (nm^3)	Voxels per tile (x, y, z)	Imaged volume (μm^3)	Color channels (exposure time per frame)	Power	Total imaging time (hours)	Stitching conditions (# of starting tiles)	Stitching results	Corrections: linear unmixing; gamma; additional flat-field
6 Cont'd				Collagen IV	Primary: mouse monoclonal (Santa Cruz Biotech, sc-59814) Secondary: goat anti-mouse CF633 (Biotium, 20120)											
7	Fig. 3; figs. S13 to S17, and S33; Movie 4; movie S2	**Mouse (Thy1-YFP) primary somatosensory cortex with Bassoon and Homer1 immunostaining**	Thy1-YFP-H	YFP	NA	3.62	Objective scan (1mM NaOH)	26.8 x 26.8 x 49.7 *(97 x 97 x 180)*	360 x 704 x 501	~280 x 1900 x 70 *(~1000 x 7000 x 250)*	488 (7 ms) 560 (7 ms) 642 (7 ms)	100% 100% 100%	80.92 (3.37 days)	Custom pipeline setup with limited search radius (18079 tiles x 3 colors)	Performed 3 iterations Retained 13193 tiles Transfer error: avg = 1.07 px, max = 17.56 px	No; Yes; No
				Bassoon	Primary: mouse monoclonal (Abcam, ab82958) Secondary: donkey anti-mouse Alexa Fluor 568 (ThermoFisher, A10037)											
				Homer1	Primary: rabbit polyclonal (Synaptic Systems, 160 003) Secondary: goat anti-rabbit Atto 647N (ThermoFisher, 40839-1ML-F)											
8	Figs. 4 and 5; figs. S18 and S19; Movies 5 and 6	**Mouse (Thy1-YFP) primary visual cortex with MBP and Caspr immunostaining**	Thy1-YFP-H	YFP	NA	3.62	Objective scan (1mM NaOH)	26.8 x 26.8 x 49.7 *(97 x 97 x 180)*	360 x 704 x 501	~280 x 1100 x 83 *(~1000 x 4000 x 300)*	488 (3 ms) 560 (3 ms) 642 (3 ms)	20% 40% 20%	34.45 (1.44 days)	Rematching mode: incremental (11224 tiles x 3 colors)	Performed 6 iterations Retained 10965 tiles Transfer error: avg = 1.28 px, max = 15.64 px	No; Yes; No
				Myelin basic protein (MBP)	Primary: chicken polyclonal (Abcam, ab134018) Secondary: goat anti-chicken Alexa Fluor 568 (ThermoFisher, A-11041)											
				Caspr	Primary: rabbit polyclonal (Abcam, ab34151) Secondary: goat anti-rabbit Atto 647N (ThermoFisher, 40839-1ML-F)											
9	Fig. 6, A and B; Movie 7	***Drosophila* olfactory projection neurons from the DC3 glomerulus of the antennal lobes (DC3 adPNs) with nc82 and Syd1 immunostaining**	w, pJFRC200-10XUAS-IVS-myr::smGFP-HA in attP18/w, UAS-Syd1-FLAG ; R44A02-p65ADZp in attP40/+ ; VT033006-ZpGAL4DBD in attP2/+	GFP	Primary: rabbit polyclonal (Thermo A-11122, 1:1000) Secondary: goat anti-rabbit Alexa Fluor 488 (Thermo A-11034, 1:200)	3.99	Objective scan	24.3 x 24.3 x 45.1 *(97 x 97 x 180)*	360 x 704 x 501	~250 x 175 x 125 *(~1000 x 700 x 500)*	488 (3 ms) 560 (3 ms) 642 (3 ms)	10% 60% 70%	8.03 (482 min)	Manually adjusted stage coordinates (2500 tiles x 3 colors)	Retained 2184 tiles Transfer error: avg = 2.84 px, max = 17.66 px	No; Yes; No
				nc82	Primary: mouse monoclonal (DSHB, 1:40) Secondary: goat anti-mouse Alexa Fluor 568 (Thermo, A-11031, 1:200)											

Table S2 Cont'd. Sample preparation, imaging, and image processing conditions for all experiments.

Sample #	Figure #	Sample name	Genotype	Fluorescent proteins and target proteins/epitopes for immunostaining	Antibodies	ExM expansion factor	Imaging mode	Voxel volume (dx, dy, dz) (nm^3)	Voxels per tile (x, y, z)	Imaged volume (μm^3)	Color channels (exposure time per frame)	Power	Total imaging time (hours)	Stitching conditions (# of starting tiles)	Stitching results	Corrections: linear unmixing; gamma; additional flat-field
9 Cont'd				Syd1-FLAG	Primary: rat monoclonal (Novus Biologicals, NBP1-06712, 1:200) Secondary: goat anti-rat Atto 647N (Rockland, 612-156-120, 1:200)											
10	Fig. 6, C to E	***Drosophila* olfactory projection neurons from the DC3 glomerulus of the antennal lobes (DC3 adPNs) with nc82 immunostaining (five brains, *D*1-*D*5)**	w, pJFRC200-10XUAS-IVS-myr::smGFP-HA in attP18/w ; R44A02-p65ADZp in attP40/+ ; VT033006-ZpGAL4DBD in attP2/+	GFP	Primary: rabbit polyclonal (Thermo A-11122, 1:1000) Secondary: goat anti-rabbit Alexa Fluor 488 (Thermo A-11034, 1:200)	3.99	Objective scan	24.3 x 24.3 x 45.1 *(97 x 97 x 180)*	360 x 704 x 501	(*D*1) ~250 x 155 x 150 *(~1000 x 620 x 600)* (*D2*-*D5*) ~80 x 80 x 60 *(~320 x 320 x 240)*	(*D*1-*D5*) 488 (7 ms) 560 (7 ms)	(*D*1) 12% 50% (*D2*-*D3*) 5% 40% (*D4*-*D5*) 5% 30%	(*D1*) 7.52 (451 min) (*D2*) 0.42 (25 min) (*D3*) 0.47 (28 min) (*D4*) 0.62 (37 min) (*D5*) 0.62 (37 min)	(*D*1) Rematching mode: incremental (2760 tiles x 2 colors) (*D2*-*D5*) No iterative rematching (*D2*: 160 tiles x 2 colors; *D3*: 180 tiles x 2 colors; *D4*: 230 tiles x 2 colors; *D5*: 230 tiles x 2 colors)	(*D*1) Performed 5 iterations Retained 2694 tiles Transfer error: avg = 2.02 px, max = 16.88 px (*D2*) Retained 132 tiles Transfer error: avg = 0.96 px, max = 1.57 px (*D3*) Retained 157 tiles Transfer error: avg = 0.92 px, max = 1.72 px (*D4*) Retained 162 tiles Transfer error: avg = 12.34 px, max = 183.41 px (*D5*) Retained 194 tiles Transfer error: avg = 0.90 px, max = 2.04 px	No; Yes; No
				nc82	Primary: mouse monoclonal (DSHB, 1:40) Secondary: goat anti-mouse Alexa Fluor 568 (Thermo, A-11031, 1:200)											
11	fig. S7	***Drosophila* olfactory projection neurons from the DC1 glomerulus of the antennal lobes (DC1 adPNs) with nc82 immunostaining**	w, pJFRC200-10XUAS-IVS-myr::smGFP-HA in attP18/w ; SS01189 (R54A11-p65ADZp in attP40; VT033006-ZpGAL4DBD in attP2)/+	GFP	Primary: rabbit polyclonal (Thermo A-11122, 1:1000) Secondary: goat anti-rabbit Alexa Fluor 488 (Thermo A-11034, 1:200)	3.99	Objective scan	24.3 x 24.3 x 37.6 *(97 x 97 x 150)*	360 x 704 x 601	~230 x 200 x 105 *(~920 x 800 x 420)*	488 (5 ms) 560 (5 ms)	80% 100%	8.22 (493 min)	Rematching mode: incremental (2556 tiles x 2 colors)	Performed 13 iterations Retained 2128 tiles Transfer error: avg = 3.54px, max = 16.70px	No; No; No
				nc82	Primary: mouse monoclonal (DSHB, 1:40) Secondary: goat anti-mouse Alexa Fluor 568 (Thermo, A-11031, 1:200)											
12	Figs. 6, F and G, and 7; figs. S1, S20, S21, S25, and S27 to S30; Movies 8 to 10; movies S4, S6, and S7	***Drosophila* broad dopaminergic neurons (DANs) with nc82 immunostaining**	w/w; ;TH-GAL4/ pJFRC12-10XUAS-IVS-myr::GFP in attP2	GFP	Primary: rabbit polyclonal (Thermo A-11122, 1:1000) Secondary: goat anti-rabbit Alexa Fluor 488 (Thermo A-11034, 1:200)	4.09	Objective scan	23.7 x 23.7 x 44.0 *(97 x 97 x 180)*	360 x 704 x 501	~340 x 660 x 90 *(~1400 x 2700 x 370)*	488 (3 ms) 560 (3 ms)	65% 100%	62.54 (2.61 days)	Stitched slabs + warping No iterative rematching (25788 tiles x 2 colors)	Performed 1 iteration for each slab; retained 13519 tiles	No; Yes (only for Figs. 6, F and G, and 7E; fig. S25A); No

Table S2 Cont'd. Sample preparation, imaging, and image processing conditions for all experiments.

Sample #	Figure #	Sample name	Genotype	Fluorescent proteins and target proteins/epitopes for immunostaining	Antibodies	ExM expansion factor	Imaging mode	Voxel volume (dx, dy, dz) (nm^3)	Voxels per tile (x, y, z)	Imaged volume (μm^3)	Color channels (exposure time per frame)	Power	Total imaging time (hours)	Stitching conditions (# of starting tiles)	Stitching results	Corrections: linear unmixing; gamma; additional flat-field
12 Cont'd				nc82	Primary: mouse monoclonal (DSHB, 1:40) Secondary: goat anti-mouse Alexa Fluor 568 (Thermo, A-11031, 1:200)											
13	fig. S20, B, E, K, and M	**Multicolor flip-out (MFCO) *Drosophila* broad dopaminergic neurons (DANs) with nc82 immunostaining**	w, pBPhsFlp2::PEST in attP3/w; TH-p65ADZp in attP40/+; DDC-ZpGAL4DBD in attP2/pJFRC201-10XUAS-FRT>STOP>FRT-myr::smGFP-HA in VK0005, pJFRC240-10XUAS-FRT>STOP>FRT-myr::smGFP-V5-THS-10XUAS-FRT>STOP>FRT-myr::smGFP-FLAG in su(Hw)attP1	nc82	Primary: mouse monoclonal (DSHB, 1:30) Secondary: donkey anti-mouse Alexa Fluor 488 (Jackson Immuno Research, 715-545-151, 1:400)	Not ExM sample										No; Yes; No
				HA	Primary: rabbit monoclonal (Cell Signaling Technologies, 3724S, 1:300) Secondary: donkey anti-rabbit Alexa Fluor 594 (Jackson Immuno Research, 711-585-152, 1:500)											
				FLAG	Primary: rat monoclonal (Novus Biologicals, NBP1-06712, 1:200) Secondary: donkey anti-rat Alexa Fluor 647 (Jackson Immuno Research,712-605-153, 1:150)											
				V5	Primary: mouse monoclonal (DyLight 549-conjugated, AbD Serotec, MCA1360D549 ,1:500)											
14	fig. S20C	***Drosophila* PPM3-EB neurons with nc82 immunostaining**	w, 20xUAS-CsChrimson-mVenus in attP18/w; R14C08p65ADZp in attP40/+; DDC-ZpGAL4DBD in attP2/+	GFP	Primary: rabbit polyclonal (Thermo A-11122, 1:1000) Secondary: goat anti-rabbit Alexa Fluor 488 (Thermo A-11034, 1:200)	Not ExM sample										No; Yes; No
				nc82	Primary: mouse monoclonal (DSHB, 1:40) Secondary: goat anti-mouse Alexa Fluor 568 (Thermo, A-11031, 1:200)											
15	fig. S20F	***Drosophila* PPM3-FB3 (a.k.a., PPM3-FBm) neurons with nc82 immunostaining**	w, 20xUAS-CsChrimson-mVenus in attP18/w; SS48802 (VT014729-p65ADZp in attP40; VT033647-ZpGAL4DBD in attP2)/+	GFP	Primary: rabbit polyclonal (Thermo A-11122, 1:1000) Secondary: goat anti-rabbit Alexa Fluor 488 (Thermo A-11034, 1:200)	Not ExM sample										No; Yes; No
				nc82	Primary: mouse monoclonal (DSHB, 1:40) Secondary: goat anti-mouse Alexa Fluor 568 (Thermo, A-11031, 1:200)											

Table S2 Cont'd. Sample preparation, imaging, and image processing conditions for all experiments.

Sample #	Figure #	Sample name	Genotype	Fluorescent proteins and target proteins/epitopes for immunostaining	Antibodies	ExM expansion factor	Imaging mode	Voxel volume (dx, dy, dz) (nm^3)	Voxels per tile (x, y, z)	Imaged volume (μm^3)	Color channels (exposure time per frame)	Power	Total imaging time (hours)	Stitching conditions (# of starting tiles)	Stitching results	Corrections: linear unmixing; gamma; additional flat-field
16	fig. S20l	***Drosophila* PPM3-FB2-NO (a.k.a., PPM3-FBv) neurons with nc82 immunostaining**	w, 20xUAS-CsChrimson-mVenus in attP18/w;SS48817 (VT009650-p65ADZp in attP40; VT033647-ZpGAL4DBD in attP2)/+	GFP	Primary: rabbit polyclonal (Thermo A-11122, 1:1000) Secondary: goat anti-rabbit Alexa Fluor 488 (Thermo A-11034, 1:200)	Not ExM sample										No; Yes; No
				nc82	Primary: mouse monoclonal (DSHB, 1:40) Secondary: goat anti-mouse Alexa Fluor 568 (Thermo, A-11031, 1:200)											
17	movie S3	***Drosophila* dorsal paired medial (DPM) neurons with nc82 immunostaining**	w/w; SS01240 (VT046004-p65ADZp in attP40; R13F04-ZpGAL4DBD in attP2) / pJFRC12-10XUAS-IVS-myr::GFP in attP2	GFP	Primary: rabbit polyclonal (Thermo A-11122, 1:1000) Secondary: goat anti-rabbit Alexa Fluor 488 (Thermo A-11034, 1:200)	3.99	Objective scan	24.3 x 24.3 x 45.1 *(97 x 97 x 180)*	360 x 704 x 601	~145 x 250 x 250 *(~580 x 1000 x 1000)*	488 (5 ms) 560 (5 ms)	30% 90%	14.73 (884 min)	Rematching mode: incremental Increased maximum allowed transfer error to 30 px (5344 tiles x 2 colors)	Performed 12 iterations Retained 4193 tiles Transfer error: avg = 2.57 px, max = 29.31 px	No; Yes; No
				nc82	Primary: mouse monoclonal (DSHB, 1:40) Secondary: goat anti-mouse Alexa Fluor 568 (Thermo, A-11031, 1:200)											
18	fig. S24	***Drosophila* mushroom body output neuron (MBON)-alpha1 with nc82 immunostaining**	w, 20xUAS-CsChrimson-mVenus in attP18/w; MB310C-split-GAL4/+	GFP	Primary: rabbit polyclonal (Thermo A-11122, 1:1000) Secondary: goat anti-rabbit Alexa Fluor 488 (Thermo A-11034, 1:200)	3.99	Objective scan	24.3 x 24.3 x 45.1 *(97 x 97 x 180)*	360 x 704 x 501	~100 x 160 x 150 *(~400 x 640 x 600)*	488 (7 ms) 560 (7 ms)	60% 80%	3.22 (193 min)	Rematching mode: full (934 tiles x 2 colors)	Performed 5 iterations Retained 402 tiles Transfer error: avg = 1.31 px, max = 5.33 px	No; No; No
				nc82	Primary: mouse monoclonal (DSHB, 1:40) Secondary: goat anti-mouse Alexa Fluor 568 (Thermo, A-11031, 1:200)											
19	fig. S23	***Drosophila* pan-neuronal with Brp-V5 and nc82 immunostaining**	w/w; df(2R)BSC29/Df(2R)brp6.1; brp-FRT-V5-2A-LexAVP16/+	Brp-V5	Primary: mouse monoclonal (Alex Fluor 488-conjugated, BIO-RAD, MCA1360A488, 1:500)	3.99	Objective scan	24.3 x 24.3 x 45.1 *(97 x 97 x 180)*	360 x 704 x 501	~180 x 145 x 120 *(~720 x 580 x 470)*	488 (10 ms) 560 (10 ms)	80% 40%	6.80 (408 min)	Rematching mode: full (1710 tiles x 2 colors)	Performed 5 iterations Retained 1445 tiles Transfer error: avg = 2.00 px, max = 17.22 px	No; No; No
				nc82	Primary: mouse monoclonal (DSHB, 1:40) Secondary: goat anti-mouse Alexa Fluor 568 (Thermo, A-11031, 1:200)											
20	fig. S3	**Mouse (Thy1-YFP) cortex**	Thy1-YFP-H	YFP	NA	6.81	Objective scan	14.2 x 14.2 x 36.7 *(97 x 97 x 250)*	360 x 704 x 361	~88 x 230 x 47 *(~600 x 1600 x 320)* (triangular prism filling about half of the volume)	488 (10 ms)	100%	3.90 (234 min)	Rematching mode: full Fusion mode: blending (1381 tiles x 1 color)	Performed 3 iterations Retained 935 tiles Transfer error: avg = 2.02 px; max = 13.35 px	No; Yes; No

Table S2 Cont'd. Sample preparation, imaging, and image processing conditions for all experiments.

Sample #	Figure #	Sample name	Genotype	Fluorescent proteins and target proteins/epitopes for immunostaining	Antibodies	ExM expansion factor	Imaging mode	Voxel volume (dx, dy, dz) (nm^3)	Voxels per tile (x, y, z)	Imaged volume (μm^3)	Color channels (exposure time per frame)	Power	Total imaging time (hours)	Stitching conditions (# of starting tiles)	Stitching results	Corrections: linear unmixing; gamma; additional flat-field
21	fig. S26	***Drosophila* mushroom body alpha 3 with nc82 immunostaining**	Canton-S	nc82	Primary: mouse monoclonal (DSHB, 1:40) Secondary: goat anti-mouse Alexa Fluor 568 (Thermo, A-11031, 1:200)	3.99	Objective scan	26.0 x 26.0 x 45.1 *(104 x 104 x 180)*	360 x 1600 x 501	~100 x 38 x 88-100 *(~400 x 150 x 350-400)*	(*F1(L)-F2(R)*) 560 (15 ms) (*F3(R)*) 488 (30 ms; not used) 560 (30 ms)	(*F1(L)-F2(R)*) 50% (*F3(R)*) 40%	(*F1(L)*) 0.3 (18 min) (*F1(R)*) 0.3 (18 min) (*F2(R)*) 0.4 (24 min) (*F3(R)*) 1.47 (88 min)	*(F1(L)-F2(R))* Rematching mode: incremental Fusion mode: blending (*F1(L)*: 112 tiles x 1 color; *F1(R)*: 112 tiles x 1 colors; *F2(R)*: 146 tiles x 1 color) *(F3(R))* Stage coordinate-based stitching Fusion mode: blending (176 tiles x 2 colors)	*(F1(L))* Performed 5 iterations Retained 108 tiles Transfer error: avg = 3.85 px, max = 13.09 px *(F1(R))* Performed 1 iteration Retained 112 tiles Transfer error: avg = 1.13 px, max = 3.68 px *(F2(R))* Performed 1 iteration Retained 146 tiles Transfer error: avg = 1.24 px, max = 4.64 px (*F3(R)*) Retained 176 tiles	No; Yes; No

Table S3. Morphology of reconstructed subcellular compartments, mitochondria and lysosomes of layer V pyramidal neurons in mouse somatosensory cortex (Fig. 2, A to E, and fig. S8).

Figure #	Volume (μm^3) (median ± MAD (median absolute deviation))	Major axis (μm) (median ± MAD)	Aspect ratio (median ± MAD)
All subcellular compartments (Fig. 2B)	$2.54 \times 10^{-2} \pm 2.33 \times 10^{-2}$	$5.09 \times 10^{-1} \pm 2.82 \times 10^{-1}$	$2.78 \times 10^{0} \pm 1.03 \times 10^{0}$
Mitochondria (Fig. 2D; fig. S8A)	$1.49 \times 10^{-1} \pm 1.25 \times 10^{-1}$	$8.98 \times 10^{-1} \pm 4.46 \times 10^{-1}$	$2.79 \times 10^{0} \pm 8.23 \times 10^{-1}$
Lysosomes (Fig. 2D; fig. S8A)	$5.77 \times 10^{-3} \pm 5.36 \times 10^{-3}$	$3.11 \times 10^{-1} \pm 2.20 \times 10^{-1}$	$3.50 \times 10^{0} \pm 9.62 \times 10^{-1}$
Dendritic mitochondria (Fig. 2E; fig. S8B)	$3.22 \times 10^{-2} \pm 3.09 \times 10^{-2}$	$6.09 \times 10^{-1} \pm 3.62 \times 10^{-1}$	$3.39 \times 10^{0} \pm 1.40 \times 10^{0}$
Axonal mitochondria (Fig. 2E; fig. S8B)	$9.17 \times 10^{-3} \pm 8.94 \times 10^{-3}$	$3.84 \times 10^{-1} \pm 2.55 \times 10^{-1}$	$2.76 \times 10^{0} \pm 8.49 \times 10^{-1}$
Somatic mitochondria (Fig. 2E; fig. S8B)	$2.26 \times 10^{-2} \pm 2.19 \times 10^{-2}$	$4.52 \times 10^{-1} \pm 2.92 \times 10^{-1}$	$2.49 \times 10^{0} \pm 8.04 \times 10^{-1}$
Dendritic lysosomes (Fig. 2E; fig. S8B)	$4.80 \times 10^{-2} \pm 4.00 \times 10^{-2}$	$6.97 \times 10^{-1} \pm 1.58 \times 10^{-1}$	$4.91 \times 10^{0} \pm 1.79 \times 10^{0}$
Axonal lysosomes (Fig. 2E; fig. S8B)	$3.64 \times 10^{-2} \pm 1.77 \times 10^{-2}$	$6.57 \times 10^{-1} \pm 2.11 \times 10^{-1}$	$4.69 \times 10^{0} \pm 1.90 \times 10^{0}$
Somatic lysosomes (Fig. 2E; fig. S8B)	$9.05 \times 10^{-2} \pm 7.28 \times 10^{-2}$	$7.69 \times 10^{-1} \pm 2.06 \times 10^{-1}$	$3.33 \times 10^{0} \pm 1.16 \times 10^{0}$

Table S4. Morphology of dendritic spines in the mouse primary somatosensory cortex (Fig. 3 and figs. S13 to S16).

Position	Spine types (T: thin; S: stubby; M: mushroom; F: filopodia)	Backbone length (µm) (median ± MAD (median absolute deviation))	Head diameter (µm) (median ± MAD)	Neck backbone length (µm) (median ± MAD)	Neck diameter (µm) (median ± MAD)	Correlation coefficient: Head diameter vs. neck diameter (*pval* < 0.05)	Correlation coefficient: Backbone length vs. head diameter (*pval* < 0.05)	Correlation coefficient: Backbone length vs. neck diameter (*pval* < 0.05)	Correlation coefficient: Neck backbone length vs. head diameter (*pval* < 0.05)	Correlation coefficient: Neck backbone length vs. neck diameter (*pval* < 0.05)
1	T: 21 S: 1 M: 2 F: 0	$6.41 \times 10^{-1} \pm 2.96 \times 10^{-1}$	$1.36 \times 10^{-1} \pm 4.38 \times 10^{-2}$	$3.22 \times 10^{-1} \pm 2.11 \times 10^{-1}$	$6.08 \times 10^{-2} \pm 4.08 \times 10^{-8}$	0.98	0.85	0.78	0.79	0.74
2	T: 118 S: 39 M: 53 F: 4	$7.64 \times 10^{-1} \pm 5.00 \times 10^{-1}$	$2.14 \times 10^{-1} \pm 1.08 \times 10^{-1}$	$4.08 \times 10^{-1} \pm 3.52 \times 10^{-1}$	$1.55 \times 10^{-1} \pm 6.75 \times 10^{-2}$	0.25	0.43	0.30	0.17	0.24
3	T: 221 S: 59 M: 233 F: 3	$1.41 \times 10^{0} \pm 5.94 \times 10^{-1}$	$3.51 \times 10^{-1} \pm 1.30 \times 10^{-1}$	$8.14 \times 10^{-1} \pm 5.32 \times 10^{-1}$	$1.55 \times 10^{-1} \pm 6.97 \times 10^{-2}$	0.58	0.51	n.c.	0.32	-0.1
4	T: 200 S: 27 M: 172 F: 7	$1.49 \times 10^{0} \pm 5.59 \times 10^{-1}$	$3.30 \times 10^{-1} \pm 1.06 \times 10^{-1}$	$8.94 \times 10^{-1} \pm 4.96 \times 10^{-1}$	$1.49 \times 10^{-1} \pm 5.11 \times 10^{-2}$	0.65	0.49	n.c.	0.35	n.c.
5	T: 127 S: 26 M: 52 F: 0	$9.38 \times 10^{-1} \pm 4.44 \times 10^{-1}$	$2.48 \times 10^{-1} \pm 1.13 \times 10^{-1}$	$4.95 \times 10^{-1} \pm 3.14 \times 10^{-1}$	$1.28 \times 10^{-1} \pm 6.80 \times 10^{-2}$	0.80	0.67	0.31	0.52	0.21
6	T: 101 S: 16 M: 3 F: 0	$5.57 \times 10^{-1} \pm 1.74 \times 10^{-1}$	$1.35 \times 10^{-1} \pm 5.32 \times 10^{-2}$	$2.86 \times 10^{-1} \pm 1.77 \times 10^{-1}$	$1.03 \times 10^{-1} \pm 5.17 \times 10^{-2}$	0.94	0.70	0.60	0.50	0.47
7	T: 26 S: 1 M: 4 F: 0	$6.71 \times 10^{-1} \pm 2.10 \times 10^{-1}$	$1.35 \times 10^{-1} \pm 6.42 \times 10^{-2}$	$3.18 \times 10^{-1} \pm 1.53 \times 10^{-1}$	$1.42 \times 10^{-1} \pm 7.87 \times 10^{-2}$	0.97	0.91	0.85	0.81	0.80
Sum of 1-7	T: 814 S:169 M: 509 F: 14	$1.15 \times 10^{0} \pm 6.00 \times 10^{-1}$	$2.83 \times 10^{-1} \pm 1.32 \times 10^{-1}$	$6.15 \times 10^{-1} \pm 4.52 \times 10^{-1}$	$1.44 \times 10^{-1} \pm 6.30 \times 10^{-2}$	0.31	0.43	n.c.	0.23	-0.11

Table S5. Assignment of PPM3 dopaminergic neuron cell types (Fig. 6, F and G, and figs. S20 and S21).

Cells	Criteria for cell type assignment					
	Tracts to the central complex	Additional branch #1	Additional branch #2	Number of cells	Innervation in the central complex	Cell type assignment
ExLLSM tracing cell #1	tract A	no	no	1	EB	PPM3-EB
ExLLSM tracing cell #2	tract A	no	no	1	EB	PPM3-EB
ExLLSM tracing cell #3	tract B	no	no	1	N.D. (FB and/or NO)	PPM3-FB3
ExLLSM tracing cell #4	tract B	no	no	1	N.D. (FB and/or NO)	PPM3-FB3
ExLLSM tracing cell #5	tract C	no	no	1	N.D. (FB and/or NO)	PPM3-FB2-NO
ExLLSM tracing cell #6	tract C	no	no	1	N.D. (FB and/or NO)	PPM3-FB2-NO
ExLLSM tracing cell #7	tract C	yes	yes	1	N.D. (FB and/or NO)	PPM3-FB3-NO-a
ExLLSM tracing cell #8	tract C	yes	no	1	N.D. (FB and/or NO)	PPM3-FB3-NO-b
MCFO single cell in fig. S20B	tract A	no	no	1	EB	PPM3-EB
MCFO single cell in fig. S20E	tract B	no	no	1	FB layer 3	PPM3-FB3
MCFO single cell in fig. S20K	tract C	yes	yes	1	FB layer 3 and NO	PPM3-FB3-NO-a
MCFO single cell in fig. S20M	tract C	yes	no	1	FB layer 3 and NO	PPM3-FB3-NO-b
Split-GAL4 (R14C08p65ADZp in attP40; DDC-ZpGAL4DBD in attP2) in fig. S20C	tract A	no	no	2	EB	PPM3-EB
Split-GAL4 SS48802 in fig. S20F	tract B	no	no	2	FB layer 3	PPM3-FB3
Split-GAL4 SS48817 in fig. S20I	tract C	no	no	2	FB layer2 and NO	PPM3-FB2-NO

Table S6. Pre-synaptic sites and dopaminergic neurons in 33 brain regions in adult *Drosophila* (Fig. 7 and figs. S28 to S30). Brain region abbreviations are given in Fig. 7.

Brain region	Region volume (μm^3)	DAN volume (μm^3)	DAN surface area (μm^2)	# of nc82 puncta	# of DAN-vicinity nc82 puncta	# of DAN-assoc nc82 puncta	Nc82 puncta volume density (# puncta /μm^3)	DAN-assoc nc82 puncta volume density (# puncta/ μm^3)	% DAN-assoc	DAN-assoc nc82 puncta DAN volume density (# puncta/ μm^3)	DAN-assoc nc82 puncta DAN surface density (# puncta/μm^2)
ME (L)	1454110	2783	38717	5644888	45302	21124	3.882	0.0145	0.374	7.592	0.546
ME (R)	1404647	2656	38153	5817334	72028	26153	4.141	0.0186	0.450	9.848	0.685
LOP (L)	321037	761	10284	1391435	10939	9376	4.334	0.0292	0.674	12.318	0.912
LOP (R)	235107	492	6626	1313992	14526	7123	5.589	0.0303	0.542	14.471	1.075
LO (L)	502852	4424	47366	2204392	19100	20145	4.384	0.0401	0.914	4.554	0.425
LO (R)	467888	4204	45506	2196657	21539	18713	4.695	0.0400	0.852	4.451	0.411
OTU (L)	36664	485	5045	155674	2921	3681	4.246	0.1004	2.365	7.584	0.730
OTU (R)	14689	89	1805	48060	869	974	3.272	0.0663	2.027	10.932	0.540
VLPR (L)	372326	2741	33411	950651	8111	4578	2.553	0.0123	0.482	1.670	0.137
VLPR (R)	346278	2594	30927	1053311	9284	6902	3.042	0.0199	0.655	2.661	0.223
LH (L)	98899	568	7885	337695	5250	3559	3.415	0.0360	1.054	6.271	0.451
LH (R)	141139	968	12538	440919	9236	5124	3.124	0.0363	1.162	5.291	0.409
CA (L)	58486	885	8018	182611	6215	5465	3.122	0.0934	2.993	6.176	0.682
CA (R)	49550	843	5289	157154	6037	3583	3.172	0.0723	2.280	4.253	0.677
MB α2 α'2 (L)	5627	476	5045	36258	3888	2970	6.443	0.5278	8.191	6.241	0.589
MB α2 α'2 (R)	2730	185	2178	15299	1252	1202	5.603	0.4402	7.857	6.483	0.552
MB α3 (L)	6273	533	5931	46636	4938	3735	7.434	0.5954	8.009	7.003	0.630
MB α3 (R)	7237	130	5884	47472	4952	4184	6.559	0.5781	8.814	32.193	0.711
MB α'3 (L)	3129	350	3083	20335	2899	2041	6.499	0.6523	10.037	5.832	0.662
MB α'3 (R)	3861	165	3143	20431	2403	1979	5.291	0.5125	9.686	11.991	0.630
MB γ1 (L)	2786	140	2638	15375	1502	478	5.518	0.1716	3.109	3.426	0.181
MB γ1 (R)	4949	309	3593	28419	2597	1149	5.743	0.2322	4.043	3.717	0.320
ATL (L)	3583	116	2086	22732	1225	646	6.345	0.1803	2.842	5.559	0.310
ATL (R)	4412	75	2753	26598	1454	1223	6.029	0.2772	4.598	16.241	0.444
PB	25429	1267	13649	84404	8222	6721	3.319	0.2643	7.963	5.304	0.492
EB	50873	1230	12456	165862	2246	2072	3.260	0.0407	1.249	1.684	0.166
FB	157813	4839	55568	537830	15165	8490	3.408	0.0538	1.579	1.755	0.153
NO (L)	4954	230	2080	15821	638	540	3.194	0.1090	3.413	2.352	0.260
NO (R)	5132	226	1868	19128	627	659	3.727	0.1284	3.445	2.914	0.353
LAL (L)	121280	2609	35068	247660	6511	3303	2.042	0.0272	1.334	1.266	0.094
LAL (R)	81398	1086	22915	205003	5426	2381	2.519	0.0293	1.161	2.192	0.104
SP (L)	810946	17701	204857	2347255	68329	33408	2.894	0.0412	1.423	1.887	0.163
SP (R)	765183	18603	211037	2238542	71722	33234	2.925	0.0434	1.485	1.786	0.157

Captions for Supplementary Movies

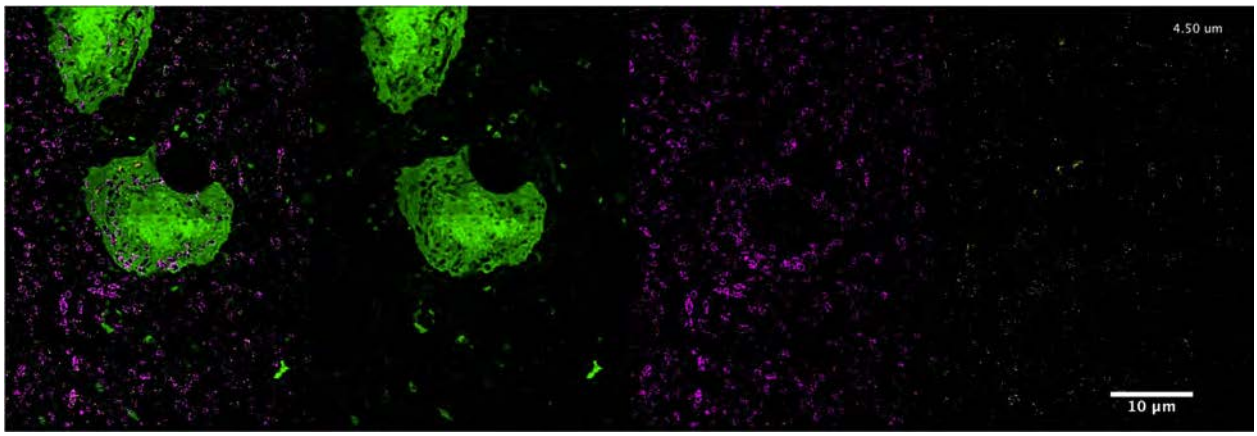

Movie S1. Immunolabeling determines organelle identity of cytosolic voids in Thy1-YFP expressing neurons. Orthoslices through an expanded tissue section from the primary somatosensory cortex of a Thy1-YFP transgenic mouse immunostained against Tom20 and LAMP1 to identify cytosolic voids that represent mitochondria and multivesicular bodies / autolysosomes, respectively. See also Fig. 2, A to E, and Movie 1.

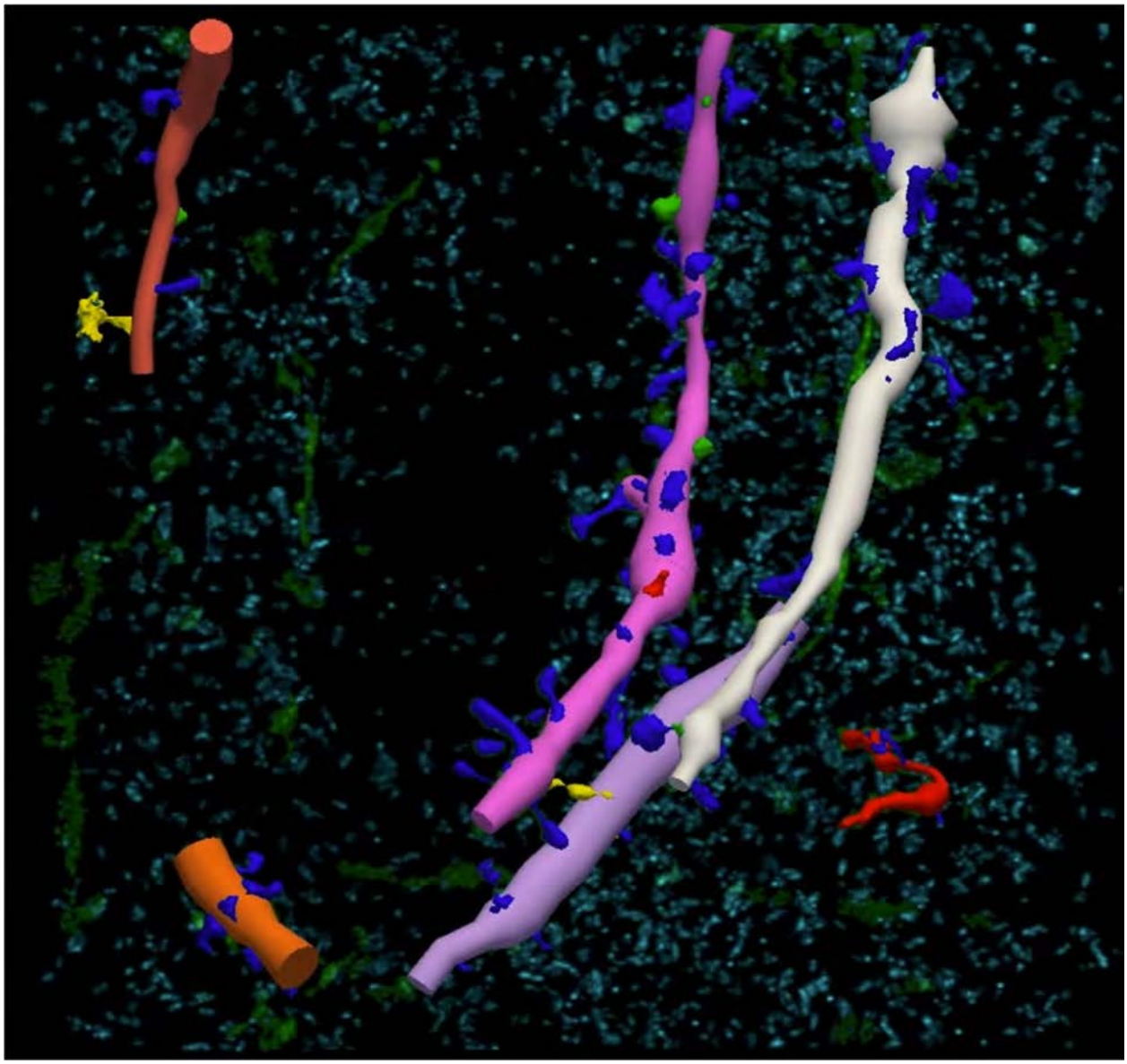

Movie S2. Reconstruction of dendritic spines of layer V pyramidal neurons in the mouse primary somatosensory cortex. One of the four 27 by 27 by 14 μm subvolumes in each of seven different regions spanning the primary somatosensory cortex (28 total subvolumes) used to quantify the morphologies of ~1500 dendritic spines, showing the reconstruction of dendrites and spines within the subvolume using Neurolucida 360. Also shown are Homer1 puncta (cyan) marking post-synaptic densities across the volume. This particular subvolume was from position 3 in Fig. 3A.

Movie S3. Dorsal paired medial (DPM) neurons and DPM-associated presynaptic sites in an adult *Drosophila* brain.

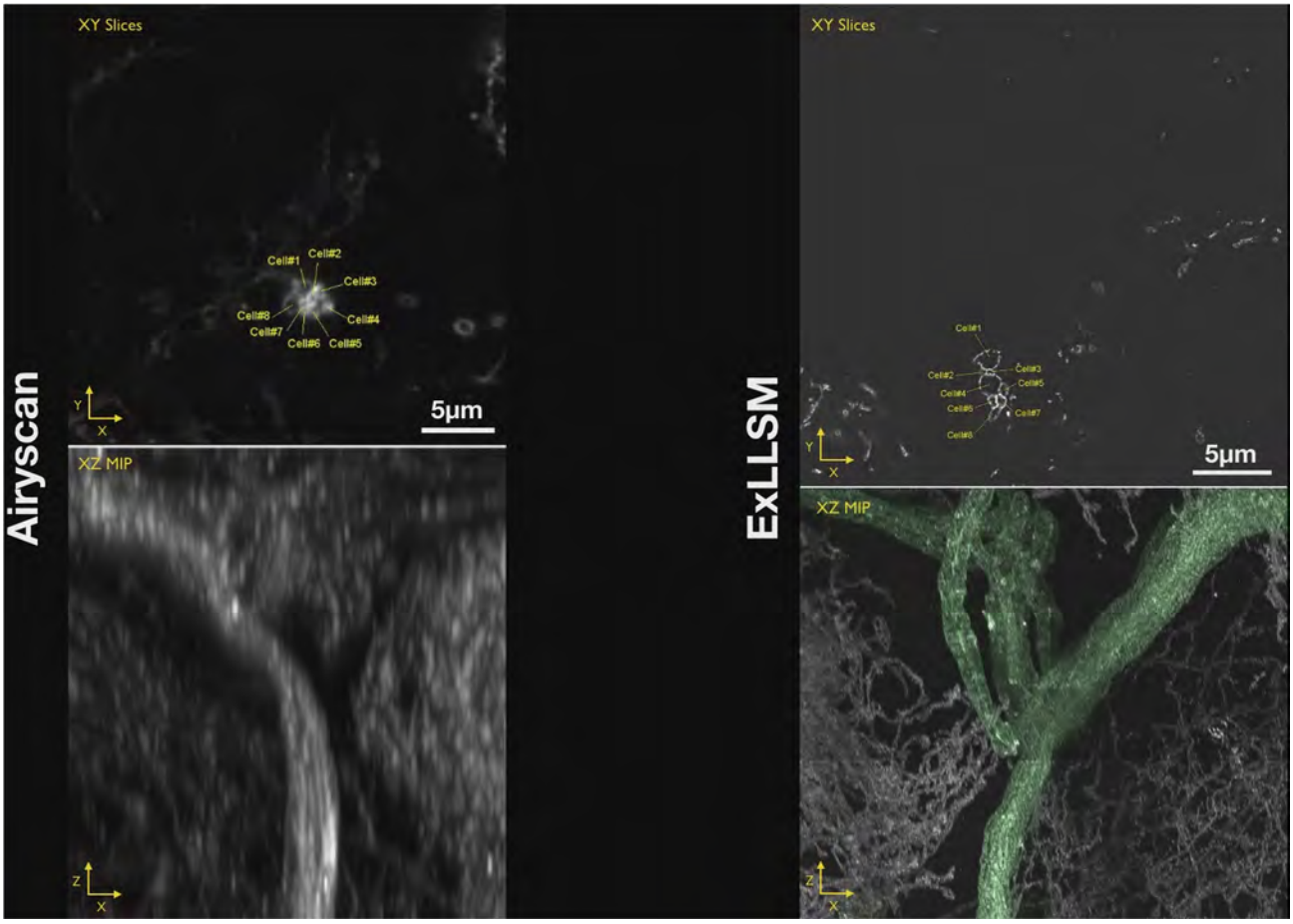

Movie S4. PPM3 dopaminergic neurons (DANs) in an adult *Drosophila* brain imaged by Airyscan (left) and ExLLSM (right).

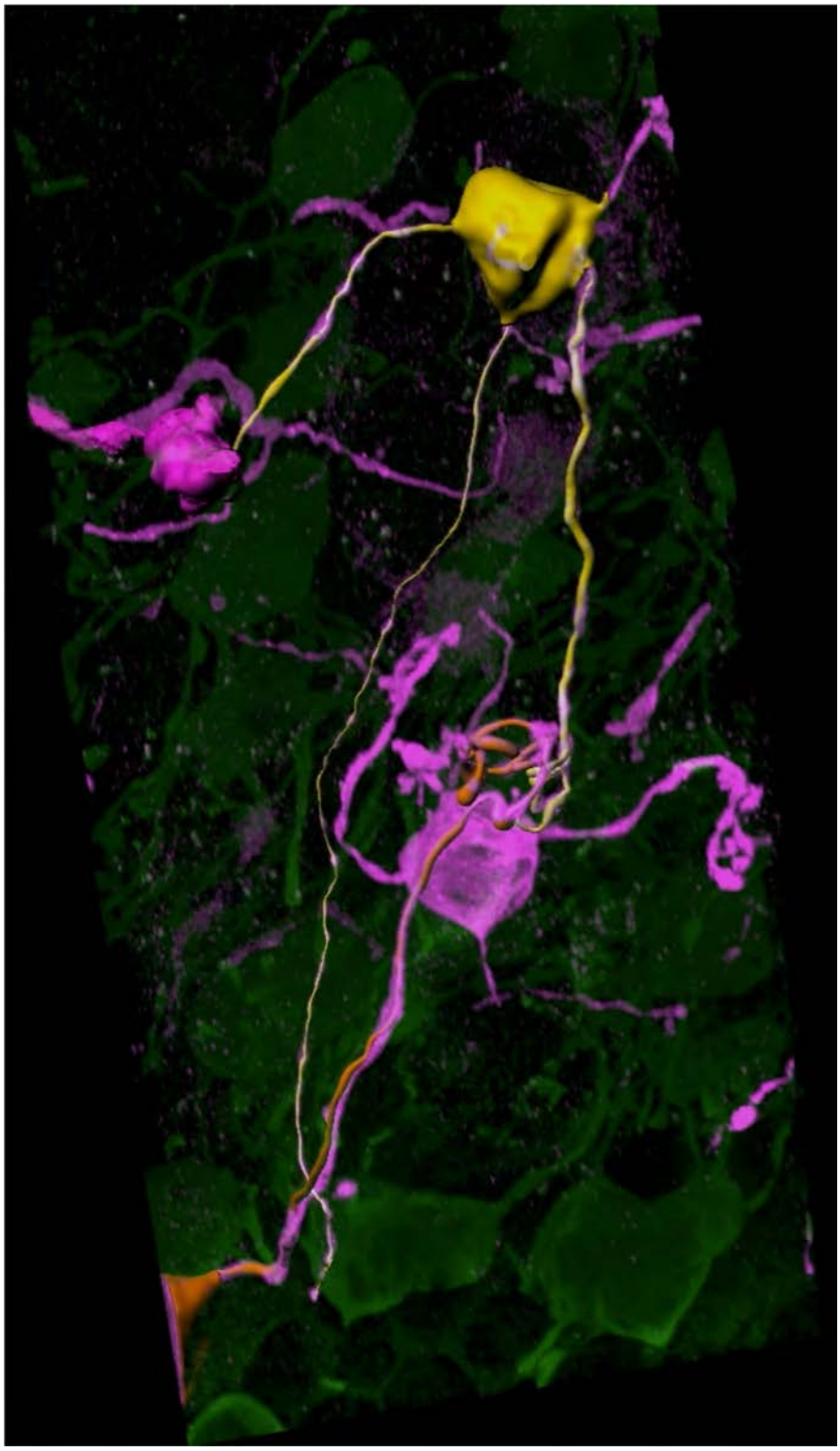

Movie S5. Tracing of sparsely labeled mossy fibers and granule cells in the mouse cerebellum. See also fig. S31.

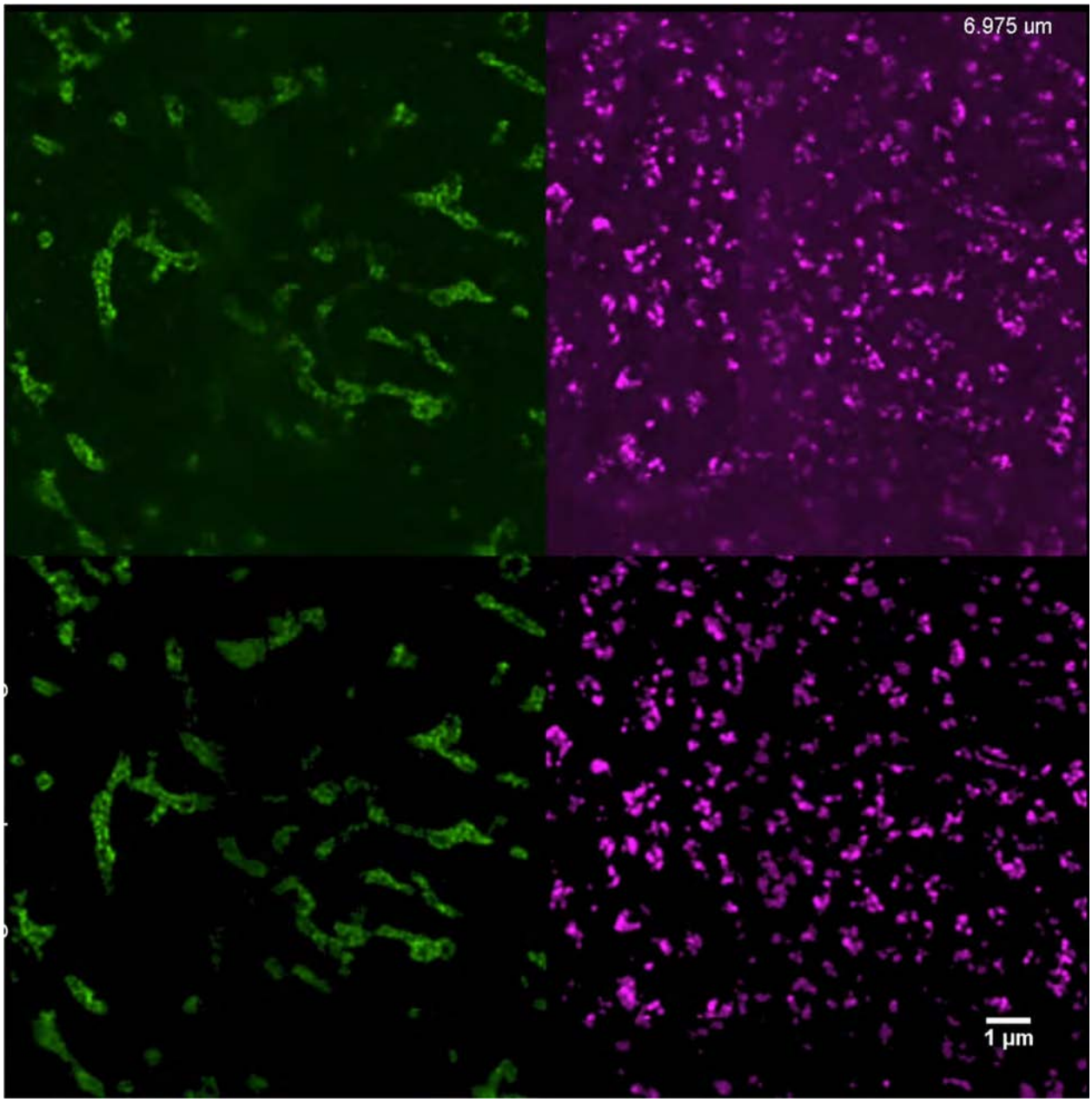

Movie S6. Flat-field corrected, deconvolved image slices (top), and flat-field corrected, deconvolved and filtered images slices (bottom) of membrane-stained dopaminergic neurons (DANs, green) and nc82 puncta (magenta).

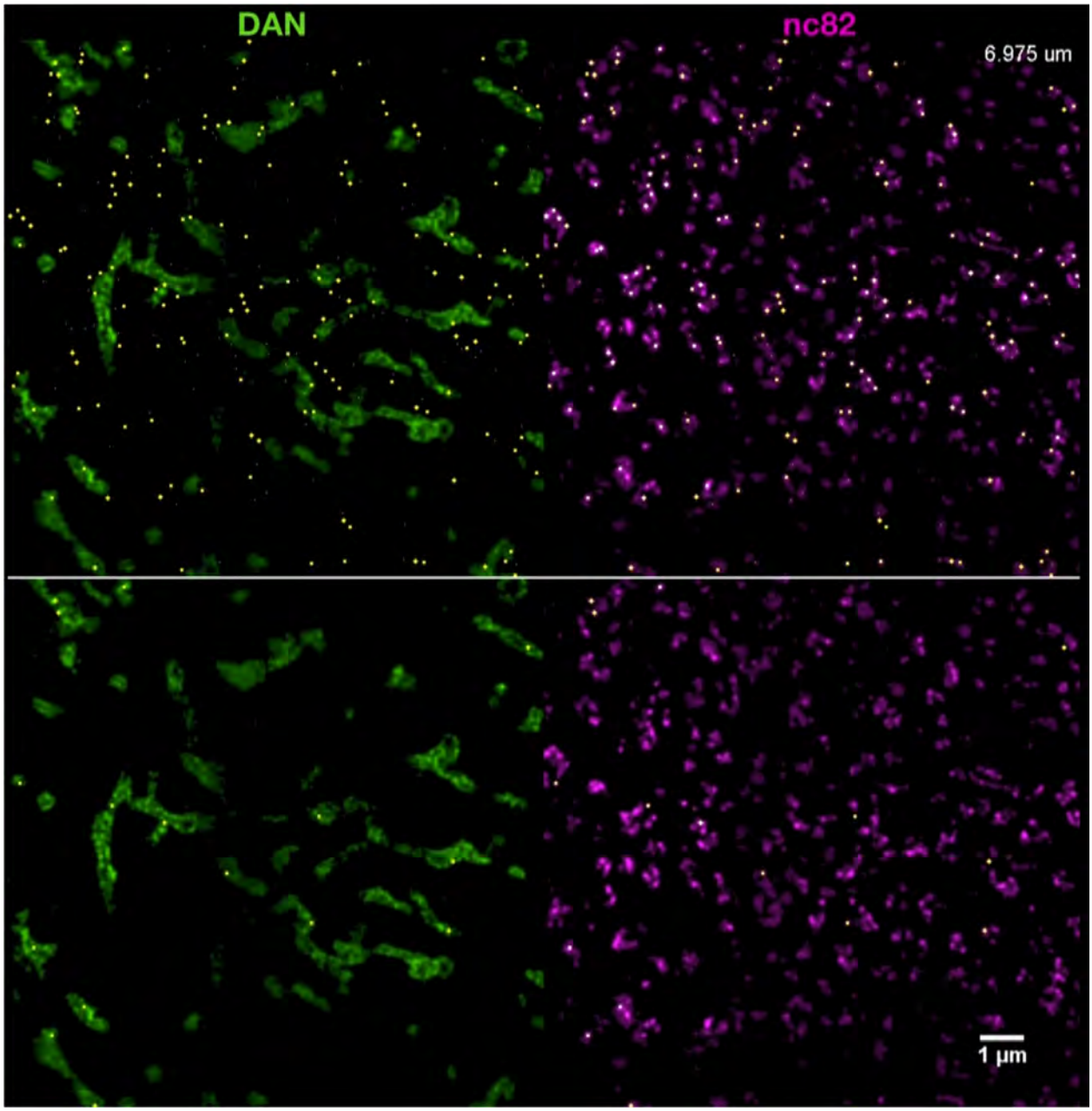

Movie S7. Detected nc82 puncta localizations (top, yellow diamonds), and DAN-associated nc82 puncta localizations (bottom, yellow diamonds) overlaid with DANs (green) and nc82 puncta (magenta).

References and Notes

1. S. Herculano-Houzel, The human brain in numbers: A linearly scaled-up primate brain. *Front. Hum. Neurosci.* **3**, 31 (2009). doi:10.3389/neuro.09.031.2009 Medline

2. K. Sharma, S. Schmitt, C. G. Bergner, S. Tyanova, N. Kannaiyan, N. Manrique-Hoyos, K. Kongi, L. Cantuti, U.-K. Hanisch, M.-A. Philips, M. J. Rossner, M. Mann, M. Simons, Cell type- and brain region-resolved mouse brain proteome. *Nat. Neurosci.* **18**, 1819–1831 (2015). doi:10.1038/nn.4160 Medline

3. J. E. Heuser, T. S. Reese, Evidence for recycling of synaptic vesicle membrane during transmitter release at the frog neuromuscular junction. *J. Cell Biol.* **57**, 315–344 (1973). doi:10.1083/jcb.57.2.315 Medline

4. C. S. Xu, K. J. Hayworth, Z. Lu, P. Grob, A. M. Hassan, J. G. García-Cerdán, K. K. Niyogi, E. Nogales, R. J. Weinberg, H. F. Hess, Enhanced FIB-SEM systems for large-volume 3D imaging. *eLife* **6**, e25916 (2017). doi:10.7554/eLife.25916 Medline

5. Z. Zheng, J. S. Lauritzen, E. Perlman, C. G. Robinson, M. Nichols, D. Milkie, O. Torrens, J. Price, C. B. Fisher, N. Sharifi, S. A. Calle-Schuler, L. Kmecova, I. J. Ali, B. Karsh, E. T. Trautman, J. A. Bogovic, P. Hanslovsky, G. S. X. E. Jefferis, M. Kazhdan, K. Khairy, S. Saalfeld, R. D. Fetter, D. D. Bock, A complete electron microscopy volume of the brain of adult *Drosophila melanogaster*. *Cell* **174**, 730–743.e22 (2018). doi:10.1016/j.cell.2018.06.019 Medline

6. K. D. Micheva, S. J. Smith, Array tomography: A new tool for imaging the molecular architecture and ultrastructure of neural circuits. *Neuron* **55**, 25–36 (2007). doi:10.1016/j.neuron.2007.06.014 Medline

7. J.-C. Rah, E. Bas, J. Colonell, Y. Mishchenko, B. Karsh, R. D. Fetter, E. W. Myers, D. B. Chklovskii, K. Svoboda, T. D. Harris, J. T. R. Isaac, Thalamocortical input onto layer 5 pyramidal neurons measured using quantitative large-scale array tomography. *Front. Neural Circuits* **7**, 177 (2013). doi:10.3389/fncir.2013.00177 Medline

8. A. S. Chiang, C.-Y. Lin, C.-C. Chuang, H.-M. Chang, C.-H. Hsieh, C.-W. Yeh, C.-T. Shih, J.-J. Wu, G.-T. Wang, Y.-C. Chen, C.-C. Wu, G.-Y. Chen, Y.-T. Ching, P.-C. Lee, C.-Y. Lin, H.-H. Lin, C.-C. Wu, H.-W. Hsu, Y.-A. Huang, J.-Y. Chen, H.-J. Chiang, C.-F. Lu, R.-F. Ni, C.-Y. Yeh, J.-K. Hwang, Three-dimensional reconstruction of brain-wide wiring networks in *Drosophila* at single-cell resolution. *Curr. Biol.* **21**, 1–11 (2011). doi:10.1016/j.cub.2010.11.056 Medline

9. A. Jenett, G. M. Rubin, T.-T. B. Ngo, D. Shepherd, C. Murphy, H. Dionne, B. D. Pfeiffer, A. Cavallaro, D. Hall, J. Jeter, N. Iyer, D. Fetter, J. H. Hausenfluck, H. Peng, E. T. Trautman, R. R. Svirskas, E. W. Myers, Z. R. Iwinski, Y. Aso, G. M. DePasquale, A. Enos, P. Hulamm, S. C. B. Lam, H.-H. Li, T. R. Laverty, F. Long, L. Qu, S. D. Murphy, K. Rokicki, T. Safford, K. Shaw, J. H. Simpson, A. Sowell, S. Tae, Y. Yu, C. T. Zugates, A GAL4-driver line resource for *Drosophila* neurobiology. *Cell Reports* **2**, 991–1001 (2012). doi:10.1016/j.celrep.2012.09.011 Medline

10. M. N. Economo, N. G. Clack, L. D. Lavis, C. R. Gerfen, K. Svoboda, E. W. Myers, J. Chandrashekar, A platform for brain-wide imaging and reconstruction of individual neurons. *eLife* **5**, e10566 (2016). doi:10.7554/eLife.10566 Medline

11. S. Shah, E. Lubeck, W. Zhou, L. Cai, In situ transcription profiling of single cells reveals spatial organization of cells in the mouse hippocampus. *Neuron* **92**, 342–357 (2016). doi:10.1016/j.neuron.2016.10.001 Medline

12. J. R. Moffitt, J. Hao, G. Wang, K. H. Chen, H. P. Babcock, X. Zhuang, High-throughput single-cell gene-expression profiling with multiplexed error-robust fluorescence in situ hybridization. *Proc. Natl. Acad. Sci. U.S.A.* **113**, 11046–11051 (2016). doi:10.1073/pnas.1612826113 Medline

13. J. Tønnesen, U. V. Nägerl, Superresolution imaging for neuroscience. *Exp. Neurol.* **242**, 33–40 (2013). doi:10.1016/j.expneurol.2012.10.004 Medline

14. H. Zhong, Applying superresolution localization-based microscopy to neurons. *Synapse* **69**, 283–294 (2015). doi:10.1002/syn.21806 Medline

15. C. I. Bargmann, Beyond the connectome: How neuromodulators shape neural circuits. *BioEssays* **34**, 458–465 (2012). doi:10.1002/bies.201100185 Medline

16. J. Lu, J. C. Tapia, O. L. White, J. W. Lichtman, The interscutularis muscle connectome. *PLOS Biol.* **7**, e32 (2009). Medline

17. A. Nern, B. D. Pfeiffer, G. M. Rubin, Optimized tools for multicolor stochastic labeling reveal diverse stereotyped cell arrangements in the fly visual system. *Proc. Natl. Acad. Sci. U.S.A.* **112**, E2967–E2976 (2015). doi:10.1073/pnas.1506763112 Medline

18. F. Chen, P. W. Tillberg, E. S. Boyden, Expansion microscopy. *Science* **347**, 543–548 (2015). doi:10.1126/science.1260088 Medline

19. P. W. Tillberg, F. Chen, K. D. Piatkevich, Y. Zhao, C.-C. Yu, B. P. English, L. Gao, A. Martorell, H.-J. Suk, F. Yoshida, E. M. DeGennaro, D. H. Roossien, G. Gong, U. Seneviratne, S. R. Tannenbaum, R. Desimone, D. Cai, E. S. Boyden, Protein-retention expansion microscopy of cells and tissues labeled using standard fluorescent proteins and antibodies. *Nat. Biotechnol.* **34**, 987–992 (2016). doi:10.1038/nbt.3625 Medline

20. B. C. Chen, W. R. Legant, K. Wang, L. Shao, D. E. Milkie, M. W. Davidson, C. Janetopoulos, X. S. Wu, J. A. Hammer 3rd, Z. Liu, B. P. English, Y. Mimori-Kiyosue, D. P. Romero, A. T. Ritter, J. Lippincott-Schwartz, L. Fritz-Laylin, R. D. Mullins, D. M. Mitchell, J. N. Bembenek, A.-C. Reymann, R. Böhme, S. W. Grill, J. T. Wang, G. Seydoux, U. S. Tulu, D. P. Kiehart, E. Betzig, Lattice light-sheet microscopy: Imaging molecules to embryos at high spatiotemporal resolution. *Science* **346**, 1257998 (2014). doi:10.1126/science.1257998 Medline

21. I. Pisarev, S. Saalfeld, Stitcher and N5 viewer; https://github.com/saalfeldlab/stitching-spark, https://github.com/saalfeldlab/n5-viewer.

22. J. Tønnesen, V. V. G. K. Inavalli, U. V. Nägerl, Super-resolution imaging of the extracellular space in living brain tissue. *Cell* **172**, 1108–1121.e15 (2018). doi:10.1016/j.cell.2018.02.007 Medline

23. L. Freifeld, I. Odstrcil, D. Förster, A. Ramirez, J. A. Gagnon, O. Randlett, E. K. Costa, S. Asano, O. T. Celiker, R. Gao, D. A. Martin-Alarcon, P. Reginato, C. Dick, L. Chen, D. Schoppik, F. Engert, H. Baier, E. S. Boyden, Expansion microscopy of zebrafish for

neuroscience and developmental biology studies. *Proc. Natl. Acad. Sci. U.S.A.* **114**, E10799–E10808 (2017). doi:10.1073/pnas.1706281114 Medline

24. T. J. Mosca, D. J. Luginbuhl, I. E. Wang, L. Luo, Presynaptic LRP4 promotes synapse number and function of excitatory CNS neurons. *eLife* **6**, e27347 (2017). doi:10.7554/eLife.27347 Medline

25. C. K. Cahoon, Z. Yu, Y. Wang, F. Guo, J. R. Unruh, B. D. Slaughter, R. S. Hawley, Superresolution expansion microscopy reveals the three-dimensional organization of the *Drosophila* synaptonemal complex. *Proc. Natl. Acad. Sci. U.S.A.* **114**, E6857–E6866 (2017). doi:10.1073/pnas.1705623114 Medline

26. A. Tsai, A. K. Muthusamy, M. R. P. Alves, L. D. Lavis, R. H. Singer, D. L. Stern, J. Crocker, Nuclear microenvironments modulate transcription from low-affinity enhancers. *eLife* **6**, e28975 (2017). doi:10.7554/eLife.28975 Medline

27. N. Jiang, H.-J. Kim, T. J. Chozinski, J. E. Azpurua, B. A. Eaton, J. C. Vaughan, J. Z. Parrish, Superresolution imaging of *Drosophila* tissues using expansion microscopy. *Mol. Biol. Cell* **29**, 1413–1421 (2018). doi:10.1091/mbc.E17-10-0583 Medline

28. F. Guo, M. Holla, M. M. Diaz, M. Rosbash, A circadian output circuit controls sleep-wake arousal threshold in *Drosophila*. *bioRxiv* (2018). 10.1101/298067

29. J. B. Chang, F. Chen, Y.-G. Yoon, E. E. Jung, H. Babcock, J. S. Kang, S. Asano, H.-J. Suk, N. Pak, P. W. Tillberg, A. T. Wassie, D. Cai, E. S. Boyden, Iterative expansion microscopy. *Nat. Methods* **14**, 593–599 (2017). doi:10.1038/nmeth.4261 Medline

30. C. J. L. Sheppard, Super resolution in confocal imaging. *Optik (Stuttg.)* **80**, 53–54 (1988).

31. C. B. Müller, J. Enderlein, Image scanning microscopy. *Phys. Rev. Lett.* **104**, 198101 (2010). doi:10.1103/PhysRevLett.104.198101 Medline

32. X.-T. Cheng, Y.-X. Xie, B. Zhou, N. Huang, T. Farfel-Becker, Z.-H. Sheng, Characterization of LAMP1-labeled nondegradative lysosomal and endocytic compartments in neurons. *J. Cell Biol.* **217**, 3127–3139 (2018). doi:10.1083/jcb.201711083 Medline

33. N. Kasthuri, K. J. Hayworth, D. R. Berger, R. L. Schalek, J. A. Conchello, S. Knowles-Barley, D. Lee, A. Vázquez-Reina, V. Kaynig, T. R. Jones, M. Roberts, J. L. Morgan, J. C. Tapia, H. S. Seung, W. G. Roncal, J. T. Vogelstein, R. Burns, D. L. Sussman, C. E. Priebe, H. Pfister, J. W. Lichtman, Saturated reconstruction of a volume of neocortex. *Cell* **162**, 648–661 (2015). doi:10.1016/j.cell.2015.06.054 Medline

34. Q. A. Liu, H. Shio, Mitochondrial morphogenesis, dendrite development, and synapse formation in cerebellum require both Bcl-w and the glutamate receptor δ2. *PLOS Genet.* **4**, e1000097 (2008). doi:10.1371/journal.pgen.1000097 Medline

35. W. Kuehnel, *Color Atlas of Cytology, Histology, and Microscopic Anatomy* (Thieme Flexibook, ed. 4, 2003).

36. V. Popov, N. I. Medvedev, H. A. Davies, M. G. Stewart, Mitochondria form a filamentous reticular network in hippocampal dendrites but are present as discrete bodies in axons: A three-dimensional ultrastructural study. *J. Comp. Neurol.* **492**, 50–65 (2005). doi:10.1002/cne.20682 Medline

37. M. R. Duchen, Mitochondria in health and disease: Perspectives on a new mitochondrial biology. *Mol. Aspects Med.* **25**, 365–451 (2004). doi:10.1016/j.mam.2004.03.001 Medline

38. S. G. Waxman, M. V. I. Bennett, Relative conduction velocities of small myelinated and non-myelinated fibres in the central nervous system. *Nat. New Biol.* **238**, 217–219 (1972). doi:10.1038/newbio238217a0 Medline

39. K. A. Nave, Myelination and support of axonal integrity by glia. *Nature* **468**, 244–252 (2010). doi:10.1038/nature09614 Medline

40. J. J. Harris, D. Attwell, The energetics of CNS white matter. *J. Neurosci.* **32**, 356–371 (2012). doi:10.1523/JNEUROSCI.3430-11.2012 Medline

41. A. Compston, A. Coles, Multiple sclerosis. *Lancet* **372**, 1502–1517 (2008). doi:10.1016/S0140-6736(08)61620-7 Medline

42. W. A. H. Rushton, A theory of the effects of fibre size in medullated nerve. *J. Physiol.* **115**, 101–122 (1951). doi:10.1113/jphysiol.1951.sp004655 Medline

43. R. La Marca, F. Cerri, K. Horiuchi, A. Bachi, M. L. Feltri, L. Wrabetz, C. P. Blobel, A. Quattrini, J. L. Salzer, C. Taveggia, TACE (ADAM17) inhibits Schwann cell myelination. *Nat. Neurosci.* **14**, 857–865 (2011). doi:10.1038/nn.2849 Medline

44. L.-J. Oluich, J. A. S. Stratton, Y. L. Xing, S. W. Ng, H. S. Cate, P. Sah, F. Windels, T. J. Kilpatrick, T. D. Merson, Targeted ablation of oligodendrocytes induces axonal pathology independent of overt demyelination. *J. Neurosci.* **32**, 8317–8330 (2012). doi:10.1523/JNEUROSCI.1053-12.2012 Medline

45. M. Zonouzi, J. Scafidi, P. Li, B. McEllin, J. Edwards, J. L. Dupree, L. Harvey, D. Sun, C. A. Hübner, S. G. Cull-Candy, M. Farrant, V. Gallo, GABAergic regulation of cerebellar NG2 cell development is altered in perinatal white matter injury. *Nat. Neurosci.* **18**, 674–682 (2015). doi:10.1038/nn.3990 Medline

46. O. O. Glebov, S. Cox, L. Humphreys, J. Burrone, Neuronal activity controls transsynaptic geometry. *Sci. Rep.* **6**, 22703 (2016). doi:10.1038/srep22703 Medline

47. A. Dani, B. Huang, J. Bergan, C. Dulac, X. Zhuang, Superresolution imaging of chemical synapses in the brain. *Neuron* **68**, 843–856 (2010). doi:10.1016/j.neuron.2010.11.021 Medline

48. N. L. Rochefort, A. Konnerth, Dendritic spines: From structure to in vivo function. *EMBO Rep.* **13**, 699–708 (2012). doi:10.1038/embor.2012.102 Medline

49. H. Hering, M. Sheng, Dendritic spines: Structure, dynamics and regulation. *Nat. Rev. Neurosci.* **2**, 880–888 (2001). doi:10.1038/35104061 Medline

50. E. A. Nimchinsky, B. L. Sabatini, K. Svoboda, Structure and function of dendritic spines. *Annu. Rev. Physiol.* **64**, 313–353 (2002). doi:10.1146/annurev.physiol.64.081501.160008 Medline

51. M. Segal, Dendritic spines and long-term plasticity. *Nat. Rev. Neurosci.* **6**, 277–284 (2005). doi:10.1038/nrn1649 Medline

52. S. Konur, D. Rabinowitz, V. L. Fenstermaker, R. Yuste, Systematic regulation of spine sizes and densities in pyramidal neurons. *J. Neurobiol.* **56**, 95–112 (2003). doi:10.1002/neu.10229 Medline

53. D. Dumitriu, A. Rodriguez, J. H. Morrison, High-throughput, detailed, cell-specific neuroanatomy of dendritic spines using microinjection and confocal microscopy. *Nat. Protoc.* **6**, 1391–1411 (2011). doi:10.1038/nprot.2011.389 Medline

54. M. Jiang, R. T. Ash, S. A. Baker, B. Suter, A. Ferguson, J. Park, J. Rudy, S. P. Torsky, H.-T. Chao, H. Y. Zoghbi, S. M. Smirnakis, Dendritic arborization and spine dynamics are abnormal in the mouse model of MECP2 duplication syndrome. *J. Neurosci.* **33**, 19518–19533 (2013). doi:10.1523/JNEUROSCI.1745-13.2013 Medline

55. X. Yu, Y. Zuo, Two-photon in vivo imaging of dendritic spines in the mouse cortex using a thinned-skull preparation. *J. Vis. Exp.* **87**, e51520 (2014). Medline

56. J. I. Arellano, R. Benavides-Piccione, J. Defelipe, R. Yuste, Ultrastructure of dendritic spines: Correlation between synaptic and spine morphologies. *Front. Neurosci.* **1**, 131–143 (2007). doi:10.3389/neuro.01.1.1.010.2007 Medline

57. C. Bosch, A. Martínez, N. Masachs, C. M. Teixeira, I. Fernaud, F. Ulloa, E. Pérez-Martínez, C. Lois, J. X. Comella, J. DeFelipe, A. Merchán-Pérez, E. Soriano, FIB/SEM technology and high-throughput 3D reconstruction of dendritic spines and synapses in GFP-labeled adult-generated neurons. *Front. Neuroanat.* **9**, 60 (2015). doi:10.3389/fnana.2015.00060 Medline

58. K. Takasaki, B. L. Sabatini, Super-resolution 2-photon microscopy reveals that the morphology of each dendritic spine correlates with diffusive but not synaptic properties. *Front. Neuroanat.* **8**, 29 (2014). doi:10.3389/fnana.2014.00029 Medline

59. J. Tønnesen, G. Katona, B. Rózsa, U. V. Nägerl, Spine neck plasticity regulates compartmentalization of synapses. *Nat. Neurosci.* **17**, 678–685 (2014). doi:10.1038/nn.3682 Medline

60. D. L. Dickstein, D. R. Dickstein, W. G. M. Janssen, P. R. Hof, J. R. Glaser, A. Rodriguez, N. O'Connor, P. Angstman, S. J. Tappan, Automatic dendritic spine quantification from confocal data with neurolucida 360. *Curr. Protoc. Neurosci.* **77**, 1, 21 (2016). doi:10.1002/cpns.16 Medline

61. E. G. Jones, T. P. S. Powell, Morphological variations in the dendritic spines of the neocortex. *J. Cell Sci.* **5**, 509–529 (1969). Medline

62. J. Grutzendler, N. Kasthuri, W. B. Gan, Long-term dendritic spine stability in the adult cortex. *Nature* **420**, 812–816 (2002). doi:10.1038/nature01276 Medline

63. L. Anton-Sanchez, C. Bielza, A. Merchán-Pérez, J.-R. Rodríguez, J. DeFelipe, P. Larrañaga, Three-dimensional distribution of cortical synapses: A replicated point pattern-based analysis. *Front. Neuroanat.* **8**, 85 (2014). doi:10.3389/fnana.2014.00085 Medline

64. J. DeFelipe, L. Alonso-Nanclares, J. I. Arellano, Microstructure of the neocortex: Comparative aspects. *J. Neurocytol.* **31**, 299–316 (2002). doi:10.1023/A:1024130211265 Medline

65. C. Sala, V. Piëch, N. R. Wilson, M. Passafaro, G. Liu, M. Sheng, Regulation of dendritic spine morphology and synaptic function by Shank and Homer. *Neuron* **31**, 115–130 (2001). doi:10.1016/S0896-6273(01)00339-7 Medline

66. U. Thomas, Modulation of synaptic signalling complexes by Homer proteins. *J. Neurochem.* **81**, 407–413 (2002). doi:10.1046/j.1471-4159.2002.00869.x Medline

67. A. Dosemeci, R. J. Weinberg, T. S. Reese, J.-H. Tao-Cheng, The postsynaptic density: There is more than meets the eye. *Front. Synaptic Neurosci.* **8**, 23 (2016). doi:10.3389/fnsyn.2016.00023 Medline

68. G. H. Diering, R. S. Nirujogi, R. H. Roth, P. F. Worley, A. Pandey, R. L. Huganir, Homer1a drives homeostatic scaling-down of excitatory synapses during sleep. *Science* **355**, 511–515 (2017). doi:10.1126/science.aai8355 Medline

69. D. Debanne, E. Campanac, A. Bialowas, E. Carlier, G. Alcaraz, Axon physiology. *Physiol. Rev.* **91**, 555–602 (2011). doi:10.1152/physrev.00048.2009 Medline

70. G. S. Tomassy, D. R. Berger, H.-H. Chen, N. Kasthuri, K. J. Hayworth, A. Vercelli, H. S. Seung, J. W. Lichtman, P. Arlotta, Distinct profiles of myelin distribution along single axons of pyramidal neurons in the neocortex. *Science* **344**, 319–324 (2014). doi:10.1126/science.1249766 Medline

71. S. Einheber, G. Zanazzi, W. Ching, S. Scherer, T. A. Milner, E. Peles, J. L. Salzer, The axonal membrane protein Caspr, a homologue of neurexin IV, is a component of the septate-like paranodal junctions that assemble during myelination. *J. Cell Biol.* **139**, 1495–1506 (1997). doi:10.1083/jcb.139.6.1495 Medline

72. C. Porrero, P. Rubio-Garrido, C. Avendaño, F. Clascá, Mapping of fluorescent protein-expressing neurons and axon pathways in adult and developing Thy1-eYFP-H transgenic mice. *Brain Res.* **1345**, 59–72 (2010). doi:10.1016/j.brainres.2010.05.061 Medline

73. S. Ramaswamy, H. Markram, Anatomy and physiology of the thick-tufted layer 5 pyramidal neuron. *Front. Cell. Neurosci.* **9**, 233 (2015). doi:10.3389/fncel.2015.00233 Medline

74. L. M. Palmer, G. J. Stuart, Site of action potential initiation in layer 5 pyramidal neurons. *J. Neurosci.* **26**, 1854–1863 (2006). doi:10.1523/JNEUROSCI.4812-05.2006 Medline

75. S. J. C. Caron, V. Ruta, L. F. Abbott, R. Axel, Random convergence of olfactory inputs in the Drosophila mushroom body. *Nature* **497**, 113–117 (2013). doi:10.1038/nature12063 Medline

76. N. J. Butcher, A. B. Friedrich, Z. Lu, H. Tanimoto, I. A. Meinertzhagen, Different classes of input and output neurons reveal new features in microglomeruli of the adult Drosophila mushroom body calyx. *J. Comp. Neurol.* **520**, 2185–2201 (2012). doi:10.1002/cne.23037 Medline

77. K. Eichler, F. Li, A. Litwin-Kumar, Y. Park, I. Andrade, C. M. Schneider-Mizell, T. Saumweber, A. Huser, C. Eschbach, B. Gerber, R. D. Fetter, J. W. Truman, C. E. Priebe, L. F. Abbott, A. S. Thum, M. Zlatic, A. Cardona, The complete connectome of a learning and memory centre in an insect brain. *Nature* **548**, 175–182 (2017). doi:10.1038/nature23455 Medline

78. W. Fouquet, D. Owald, C. Wichmann, S. Mertel, H. Depner, M. Dyba, S. Hallermann, R. J. Kittel, S. Eimer, S. J. Sigrist, Maturation of active zone assembly by *Drosophila* Bruchpilot. *J. Cell Biol.* **186**, 129–145 (2009). doi:10.1083/jcb.200812150 Medline

79. N. Ehmann, S. van de Linde, A. Alon, D. Ljaschenko, X. Z. Keung, T. Holm, A. Rings, A. DiAntonio, S. Hallermann, U. Ashery, M. Heckmann, M. Sauer, R. J. Kittel, Quantitative super-resolution imaging of Bruchpilot distinguishes active zone states. *Nat. Commun.* **5**, 4650 (2014). doi:10.1038/ncomms5650 Medline

80. Z. Mao, R. L. Davis, Eight different types of dopaminergic neurons innervate the *Drosophila* mushroom body neuropil: Anatomical and physiological heterogeneity. *Front. Neural Circuits* **3**, 5 (2009). doi:10.3389/neuro.04.005.2009 Medline

81. E. C. Kong, K. Woo, H. Li, T. Lebestky, N. Mayer, M. R. Sniffen, U. Heberlein, R. J. Bainton, J. Hirsh, F. W. Wolf, A pair of dopamine neurons target the D1-like dopamine receptor DopR in the central complex to promote ethanol-stimulated locomotion in *Drosophila*. *PLOS ONE* **5**, e9954 (2010). doi:10.1371/journal.pone.0009954 Medline

82. O. V. Alekseyenko, Y.-B. Chan, M. P. Fernandez, T. Bülow, M. J. Pankratz, E. A. Kravitz, Single serotonergic neurons that modulate aggression in *Drosophila*. *Curr. Biol.* **24**, 2700–2707 (2014). doi:10.1016/j.cub.2014.09.051 Medline

83. S. Y. Takemura, Y. Aso, T. Hige, A. Wong, Z. Lu, C. S. Xu, P. K. Rivlin, H. Hess, T. Zhao, T. Parag, S. Berg, G. Huang, W. Katz, D. J. Olbris, S. Plaza, L. Umayam, R. Aniceto, L.-A. Chang, S. Lauchie, O. Ogundeyi, C. Ordish, A. Shinomiya, C. Sigmund, S. Takemura, J. Tran, G. C. Turner, G. M. Rubin, L. K. Scheffer, A connectome of a learning and memory center in the adult *Drosophila* brain. *eLife* **6**, e26975 (2017). doi:10.7554/eLife.26975 Medline

84. D. Owald, W. Fouquet, M. Schmidt, C. Wichmann, S. Mertel, H. Depner, F. Christiansen, C. Zube, C. Quentin, J. Körner, H. Urlaub, K. Mechtler, S. J. Sigrist, A Syd-1 homologue regulates pre- and postsynaptic maturation in *Drosophila*. *J. Cell Biol.* **188**, 565–579 (2010). doi:10.1083/jcb.200908055 Medline

85. S. Holbrook, J. K. Finley, E. L. Lyons, T. G. Herman, Loss of syd-1 from R7 neurons disrupts two distinct phases of presynaptic development. *J. Neurosci.* **32**, 18101–18111 (2012). doi:10.1523/JNEUROSCI.1350-12.2012 Medline

86. Y. Aso, D. Hattori, Y. Yu, R. M. Johnston, N. A. Iyer, T.-T. B. Ngo, H. Dionne, L. F. Abbott, R. Axel, H. Tanimoto, G. M. Rubin, The neuronal architecture of the mushroom body provides a logic for associative learning. *eLife* **3**, e04577 (2014). doi:10.7554/eLife.04577 Medline

87. Y. Aso, G. M. Rubin, Dopaminergic neurons write and update memories with cell-type-specific rules. *eLife* **5**, e16135 (2016). doi:10.7554/eLife.16135 Medline

88. L. Kahsai, T. Zars, Learning and memory in *Drosophila*: Behavior, genetics, and neural systems. *Int. Rev. Neurobiol.* **99**, 139–167 (2011). doi:10.1016/B978-0-12-387003-2.00006-9 Medline

89. H. Luan, N. C. Peabody, C. R. Vinson, B. H. White, Refined spatial manipulation of neuronal function by combinatorial restriction of transgene expression. *Neuron* **52**, 425–436 (2006). doi:10.1016/j.neuron.2006.08.028 Medline

90. B. D. Pfeiffer, T.-T. B. Ngo, K. L. Hibbard, C. Murphy, A. Jenett, J. W. Truman, G. M. Rubin, Refinement of tools for targeted gene expression in *Drosophila*. *Genetics* **186**, 735–755 (2010). doi:10.1534/genetics.110.119917 Medline

91. M. J. Dolan, H. Luan, W. C. Shropshire, B. Sutcliffe, B. Cocanougher, R. L. Scott, S. Frechter, M. Zlatic, G. S. X. E. Jefferis, B. H. White, Facilitating neuron-specific genetic manipulations in *Drosophila melanogaster* using a split GAL4 repressor. *Genetics* **206**, 775–784 (2017). doi:10.1534/genetics.116.199687 Medline

92. D. D. Bock, W.-C. A. Lee, A. M. Kerlin, M. L. Andermann, G. Hood, A. W. Wetzel, S. Yurgenson, E. R. Soucy, H. S. Kim, R. C. Reid, Network anatomy and in vivo physiology of visual cortical neurons. *Nature* **471**, 177–182 (2011). doi:10.1038/nature09802 Medline

93. T.-W. Chen, T. J. Wardill, Y. Sun, S. R. Pulver, S. L. Renninger, A. Baohan, E. R. Schreiter, R. A. Kerr, M. B. Orger, V. Jayaraman, L. L. Looger, K. Svoboda, D. S. Kim, Ultrasensitive fluorescent proteins for imaging neuronal activity. *Nature* **499**, 295–300 (2013). doi:10.1038/nature12354 Medline

94. B. F. Fosque, Y. Sun, H. Dana, C.-T. Yang, T. Ohyama, M. R. Tadross, R. Patel, M. Zlatic, D. S. Kim, M. B. Ahrens, V. Jayaraman, L. L. Looger, E. R. Schreiter, Neural circuits. Labeling of active neural circuits in vivo with designed calcium integrators. *Science* **347**, 755–760 (2015). doi:10.1126/science.1260922 Medline

95. P. de Boer, J. P. Hoogenboom, B. N. G. Giepmans, Correlated light and electron microscopy: Ultrastructure lights up! *Nat. Methods* **12**, 503–513 (2015). doi:10.1038/nmeth.3400 Medline

96. T. J. Chozinski, A. R. Halpern, H. Okawa, H.-J. Kim, G. J. Tremel, R. O. L. Wong, J. C. Vaughan, Expansion microscopy with conventional antibodies and fluorescent proteins. *Nat. Methods* **13**, 485–488 (2016). doi:10.1038/nmeth.3833 Medline

97. T. Ku, J. Swaney, J.-Y. Park, A. Albanese, E. Murray, J. H. Cho, Y.-G. Park, V. Mangena, J. Chen, K. Chung, Multiplexed and scalable super-resolution imaging of three-dimensional protein localization in size-adjustable tissues. *Nat. Biotechnol.* **34**, 973–981 (2016). doi:10.1038/nbt.3641 Medline

98. Y. Zhao, O. Bucur, H. Irshad, F. Chen, A. Weins, A. L. Stancu, E.-Y. Oh, M. DiStasio, V. Torous, B. Glass, I. E. Stillman, S. J. Schnitt, A. H. Beck, E. S. Boyden, Nanoscale imaging of clinical specimens using pathology-optimized expansion microscopy. *Nat. Biotechnol.* **35**, 757–764 (2017). doi:10.1038/nbt.3892 Medline

99. U. Schnell, F. Dijk, K. A. Sjollema, B. N. G. Giepmans, Immunolabeling artifacts and the need for live-cell imaging. *Nat. Methods* **9**, 152–158 (2012). doi:10.1038/nmeth.1855 Medline

100. D. R. Whelan, T. D. M. Bell, Image artifacts in single molecule localization microscopy: Why optimization of sample preparation protocols matters. *Sci. Rep.* **5**, 7924 (2015). doi:10.1038/srep07924 Medline

101. D. Li, L. Shao, B.-C. Chen, X. Zhang, M. Zhang, B. Moses, D. E. Milkie, J. R. Beach, J. A. Hammer 3rd, M. Pasham, T. Kirchhausen, M. A. Baird, M. W. Davidson, P. Xu, E. Betzig, ADVANCED IMAGING. Extended-resolution structured illumination imaging

of endocytic and cytoskeletal dynamics. *Science* **349**, aab3500 (2015). doi:10.1126/science.aab3500 Medline

102. W. R. Legant, L. Shao, J. B. Grimm, T. A. Brown, D. E. Milkie, B. B. Avants, L. D. Lavis, E. Betzig, High-density three-dimensional localization microscopy across large volumes. *Nat. Methods* **13**, 359–365 (2016). doi:10.1038/nmeth.3797 Medline

103. K. J. Hayworth, C. S. Xu, Z. Lu, G. W. Knott, R. D. Fetter, J. C. Tapia, J. W. Lichtman, H. F. Hess, Ultrastructurally smooth thick partitioning and volume stitching for large-scale connectomics. *Nat. Methods* **12**, 319–322 (2015). doi:10.1038/nmeth.3292 Medline

104. Y.-G. Yoon, P. Dai, J. Wohlwend, J.-B. Chang, A. H. Marblestone, E. S. Boyden, Feasibility of 3D reconstruction of neural morphology using expansion microscopy and barcode-guided agglomeration. *Front. Comput. Neurosci.* **11**, 97 (2017). doi:10.3389/fncom.2017.00097 Medline

105. S. M. Asano, R. Gao, A. T. Wassie, P. W. Tillberg, F. Chen, E. S. Boyden, Expansion microscopy: Protocols for imaging proteins and RNA in cells and tissues. *Curr. Protoc. Cell Biol.* **80**, e56 (2018). doi:10.1002/cpcb.56 Medline

106. T. L. Liu, S. Upadhyayula, D. E. Milkie, V. Singh, K. Wang, I. A. Swinburne, K. R. Mosaliganti, Z. M. Collins, T. W. Hiscock, J. Shea, A. Q. Kohrman, T. N. Medwig, D. Dambournet, R. Forster, B. Cunniff, Y. Ruan, H. Yashiro, S. Scholpp, E. M. Meyerowitz, D. Hockemeyer, D. G. Drubin, B. L. Martin, D. Q. Matus, M. Koyama, S. G. Megason, T. Kirchhausen, E. Betzig, Observing the cell in its native state: Imaging subcellular dynamics in multicellular organisms. *Science* **360**, eaaq1392 (2018). doi:10.1126/science.aaq1392 Medline

107. K. Smith, Y. Li, F. Piccinini, G. Csucs, C. Balazs, A. Bevilacqua, P. Horvath, CIDRE: An illumination-correction method for optical microscopy. *Nat. Methods* **12**, 404–406 (2015). doi:10.1038/nmeth.3323 Medline

108. S. Preibisch, S. Saalfeld, P. Tomancak, Globally optimal stitching of tiled 3D microscopic image acquisitions. *Bioinformatics* **25**, 1463–1465 (2009). doi:10.1093/bioinformatics/btp184 Medline

109. D. Hörl *et al*., BigStitcher: Reconstructing high-resolution image datasets of cleared and expanded samples. *bioRxiv* (2018). 10.1101/343954

110. M. Emmenlauer, O. Ronneberger, A. Ponti, P. Schwarb, A. Griffa, A. Filippi, R. Nitschke, W. Driever, H. Burkhardt, XuvTools: Free, fast and reliable stitching of large 3D datasets. *J. Microsc.* **233**, 42–60 (2009). doi:10.1111/j.1365-2818.2008.03094.x Medline

111. A. Bria, G. Iannello, TeraStitcher—A tool for fast automatic 3D-stitching of teravoxel-sized microscopy images. *BMC Bioinformatics* **13**, 316 (2012). doi:10.1186/1471-2105-13-316 Medline

112. T. Pietzsch, S. Preibisch, P. Tomancák, S. Saalfeld, ImgLib2—Generic image processing in Java. *Bioinformatics* **28**, 3009–3011 (2012). doi:10.1093/bioinformatics/bts543 Medline

113. J. Schindelin, I. Arganda-Carreras, E. Frise, V. Kaynig, M. Longair, T. Pietzsch, S. Preibisch, C. Rueden, S. Saalfeld, B. Schmid, J.-Y. Tinevez, D. J. White, V. Hartenstein,

K. Eliceiri, P. Tomancak, A. Cardona, Fiji: An open-source platform for biological-image analysis. *Nat. Methods* **9**, 676–682 (2012). doi:10.1038/nmeth.2019 Medline

114. T. Pietzsch, S. Saalfeld, S. Preibisch, P. Tomancak, BigDataViewer: Visualization and processing for large image data sets. *Nat. Methods* **12**, 481–483 (2015). doi:10.1038/nmeth.3392 Medline

115. I. R. Wickersham, D. C. Lyon, R. J. O. Barnard, T. Mori, S. Finke, K.-K. Conzelmann, J. A. T. Young, E. M. Callaway, Monosynaptic restriction of transsynaptic tracing from single, genetically targeted neurons. *Neuron* **53**, 639–647 (2007). doi:10.1016/j.neuron.2007.01.033 Medline

116. H. Dionne, K. L. Hibbard, A. Cavallaro, J. C. Kao, G. M. Rubin, Genetic reagents for making split-GAL4 lines in *Drosophila*. *Genetics* **209**, 31–35 (2018). doi:10.1534/genetics.118.300682 Medline

117. L. Tirian, B. Dickson, The VT GAL4, LexA, and split-GAL4 driver line collections for targeted expression in the *Drosophila* nervous system. *bioRxiv* (2017). 10.1101/198648

118. S. Truckenbrodt, M. Maidorn, D. Crzan, H. Wildhagen, S. Kabatas, S. O. Rizzoli, X10 expansion microscopy enables 25-nm resolution on conventional microscopes. *EMBO Rep.* **19**, e45836 (2018). doi:10.15252/embr.201845836 Medline

119. J. A. Bogovic, S. Saalfeld, BigWarp, (available at https://github.com/saalfeldlab/bigwarp).

120. J. A. Bogovic, P. Hanslovsky, A. Wong, S. Saalfeld, in Proceedings—International Symposium on Biomedical Imaging (2016), pp. 1123–1126.

121. F. Aguet, S. Upadhyayula, R. Gaudin, Y. Y. Chou, E. Cocucci, K. He, B.-C. Chen, K. Mosaliganti, M. Pasham, W. Skillern, W. R. Legant, T.-L. Liu, G. Findlay, E. Marino, G. Danuser, S. Megason, E. Betzig, T. Kirchhausen, Membrane dynamics of dividing cells imaged by lattice light-sheet microscopy. *Mol. Biol. Cell* **27**, 3418–3435 (2016). doi:10.1091/mbc.e16-03-0164 Medline

122. N. Otsu, A threshold selection method from gray-level histograms. *IEEE Trans. Syst. Man Cybern.* **9**, 62–66 (1979). doi:10.1109/TSMC.1979.4310076

123. P. A. Yushkevich, J. Piven, H. C. Hazlett, R. G. Smith, S. Ho, J. C. Gee, G. Gerig, User-guided 3D active contour segmentation of anatomical structures: Significantly improved efficiency and reliability. *Neuroimage* **31**, 1116–1128 (2006). doi:10.1016/j.neuroimage.2006.01.015 Medline

124. A. Rodriguez, D. B. Ehlenberger, P. R. Hof, S. L. Wearne, Rayburst sampling, an algorithm for automated three-dimensional shape analysis from laser scanning microscopy images. *Nat. Protoc.* **1**, 2152–2161 (2006). doi:10.1038/nprot.2006.313 Medline

125. A. Rodriguez, D. B. Ehlenberger, D. L. Dickstein, P. R. Hof, S. L. Wearne, Automated three-dimensional detection and shape classification of dendritic spines from fluorescence microscopy images. *PLOS ONE* **3**, e1997 (2008). doi:10.1371/journal.pone.0001997 Medline

126. S. B. Berman, Y. B. Chen, B. Qi, J. M. McCaffery, E. B. Rucker 3rd, S. Goebbels, K.-A. Nave, B. A. Arnold, E. A. Jonas, F. J. Pineda, J. M. Hardwick, Bcl-x L increases

mitochondrial fission, fusion, and biomass in neurons. *J. Cell Biol.* **184**, 707–719 (2009). doi:10.1083/jcb.200809060 Medline

127. M. Kislin, J. Sword, I. V. Fomitcheva, D. Croom, E. Pryazhnikov, E. Lihavainen, D. Toptunov, H. Rauvala, A. S. Ribeiro, L. Khiroug, S. A. Kirov, Reversible disruption of neuronal mitochondria by ischemic and traumatic injury revealed by quantitative two-photon imaging in the neocortex of anesthetized mice. *J. Neurosci.* **37**, 333–348 (2017). doi:10.1523/JNEUROSCI.1510-16.2016 Medline

128. M. Arakawa, A scanning electron microscope study of the human glomerulus. *Am. J. Pathol.* **64**, 457–466 (1971). Medline

129. Q. Liu, S. Liu, L. Kodama, M. R. Driscoll, M. N. Wu, Two dopaminergic neurons signal to the dorsal fan-shaped body to promote wakefulness in *Drosophila*. *Curr. Biol.* **22**, 2114–2123 (2012). doi:10.1016/j.cub.2012.09.008 Medline

130. K. Cichewicz, E. J. Garren, C. Adiele, Y. Aso, Z. Wang, M. Wu, S. Birman, G. M. Rubin, J. Hirsh, A new brain dopamine-deficient *Drosophila* and its pharmacological and genetic rescue. *Genes Brain Behav.* **16**, 394–403 (2017). doi:10.1111/gbb.12353 Medline

131. K. Xu, G. Zhong, X. Zhuang, Actin, spectrin, and associated proteins form a periodic cytoskeletal structure in axons. *Science* **339**, 452–456 (2013). doi:10.1126/science.1232251 Medline

132. A. Curd, A. Cleasby, K. Makowska, A. York, H. Shroff, M. Peckham, Construction of an instant structured illumination microscope. *Methods* **88**, 37–47 (2015). doi:10.1016/j.ymeth.2015.07.012 Medline

133. T. Azuma, T. Kei, Super-resolution spinning-disk confocal microscopy using optical photon reassignment. *Opt. Express* **23**, 15003–15011 (2015). doi:10.1364/OE.23.015003 Medline